DISSERTATION

Experimental and TCAD Analysis of Behaviour of Multifinger Devices with Substrate Coupling and of Filamentary States in SCRs for ESD Protection

ausgeführt zum Zwecke der Erlangung des akademischen Grades eines
Doktors der technischen Wissenschaften

unter der Leitung von

Ao.Univ.Prof. Dipl.-Ing. Dr. Dionyz Pogany
Institut für Festkörperelektronik

eingereicht an der

Technischen Universität Wien
Fakultät für Elektrotechnik und Informationstechnik

von

Dipl.-Ing. Hasan Karaca

Mat.Nr. 11743102

Wien, Juli 2021

Dissertation Betreuer und Prüfer: Ao.Univ.Prof. Dipl.-Ing. Dr. Dionyz Pogany
Begutachter und Prüfer: Prof. Dr. Gaudenzio Meneghesso
Begutachter und Prüfer: Prof. Dr. Nicolas Nolhier

Tag der mündlichen Prüfung: DD MM YY, HH Uhr

“Tesla’s cat [Nikola Tesla’s favorite childhood companion] was the family’s black cat, Macak. Macak followed young Nikola everywhere, and they spent many happy hours rolling on the grass.

It was Macak the cat who introduced Tesla to electricity on a dry winter evening. “As I stroked Macak’s back,” he recalled, “I saw a miracle that made me speechless with amazement. Macak’s back was a sheet of light and my hand produced a shower of sparks loud enough to be heard all over the house.” Curious, he asked his father what caused the sparks. Puzzled at first, [his father] finally answered, “Well, this is nothing but electricity, the same thing you see through the trees in a storm.” His father’s answer, equating the sparks with lightning, fascinated the young boy. As Tesla continued to stroke Macak, he began to wonder, “Is nature a gigantic cat? If so, who strokes its back? It can only be God,” he concluded.”

— W. Bernard Carlson, Tesla: Inventor of the Electrical Age

Abstract

Silicon Controlled Rectifiers (SCRs) are popular devices for electrostatic discharge (ESD) protection due to their low capacitance and high failure current. For high ESD robustness, in addition, simultaneous or sufficiently fast triggering of device fingers are required and for latch-up safe operation, high holding voltage, V_{HOLD}, and high holding current, I_{HOLD}, are often requested. SCRs we studied are of discrete technology for system level ESD protection.

This thesis consists of two parts. In the first part, the triggering behavior of multi-finger SCRs with substrate coupling were investigated under a HBM-like TLP stress and a Surge-like half sinusoidal pulse by using Transmission Line Pulser (TLP) system, Transient Interferometric Mapping (TIM) technique and simulations from Synopsys Sentaurus TCAD. Under the HBM-like TLP stress, RT dependent simultaneous ($RT = 300$ ps) and sequential ($RT = 10$ ns) finger triggering mechanisms were explained, and the effect of applied current and different layout variations were analyzed. Under the Surge-like half sinusoidal pulse, on the other hand, geometry dependent direction of finger activity spreading was studied and the effect of different layout variations were explained.

In the second part, the current filament (CF) related double-hysteresis IV behavior and I_{HOLD} were analyzed by using emission microscopy (EMMI) and 3D TCAD simulations in SCRs. A 3D TCAD methodology that uses up and down quasi-DC current sweeps was suggested to reveal the double-hysteresis IV behavior in long width devices. In addition to that, the non-trivial dependence of I_{HOLD} on device width was investigated and the numerical aspects to induce inhomogeneity in the current flow along the device width were discussed. The effect of different layout parameters on the value of I_{HOLD} were also studied.

The results acquired in this thesis are important for designing latch-up safe and robust ESD protection devices.

Kurzfassung

Siliziumgesteuerte Gleichrichter (SCRs) sind aufgrund ihrer geringen Kapazität und ihres hohen Ausfallstroms beliebte Bauelemente für den Schutz vor elektrostatischer Entladung (ESD). Für eine hohe ESD-Robustheit sind außerdem eine gleichzeitige oder ausreichend schnelle Auslösung der Bauteil-Finger erforderlich und für einen Latch-up-sicheren Betrieb werden oft eine hohe Haltespannung, V_{HOLD}, und ein hoher Haltestrom, I_{HOLD}, gefordert. Die von uns untersuchten SCRs sind von diskreter Technologie für den ESD-Schutz auf Systemebene.

Diese Arbeit besteht aus zwei Teilen. Im ersten Teil wurde das Auslöseverhalten von Multi-Finger-SCRs mit Substratkopplung unter einem HBM-ähnlichen TLP-Stress und einem Surge-ähnlichen Halbsinuspuls mit Hilfe eines Transmission Line Pulser (TLP)-Systems, Transient Interferometric Mapping (TIM)-Technik und Simulationen in Synopsys Sentaurus TCAD untersucht. Unter der HBM-ähnlichen TLP-Belastung wurden RT-abhängige simultane (RT = 300 ps) und sequentielle (RT = 10 ns) Finger-Trigger-Mechanismen erklärt und die Auswirkung des angelegten Stroms und verschiedener Layout-Variationen analysiert. Unter dem Surge-ähnlichen Halbsinuspuls wurde dagegen die geometrieabhängige Richtung der Ausbreitung der Fingeraktivität untersucht und der Effekt verschiedener Layoutvariationen erklärt.

Im zweiten Teil wurden das mit dem Current Filament (CF) zusammenhängende Doppelhysterese-IV-Verhalten und I_{HOLD} mit Hilfe von Emissionsmikroskopie (EMMI) und 3D TCAD-Simulationen in SCRs analysiert. Eine 3D-TCAD-Methode, die Auf- und Abwärts-Quasi-DC-Stromsweeps verwendet, wurde vorgeschlagen, um das Doppelhysterese-IV-Verhalten in Bauteilen mit großer Breite zu zeigen. Darüber hinaus wurde die nichttriviale Abhängigkeit von I_{HOLD} von der Bauteilbreite untersucht und die numerischen Aspekte zur Induzierung von Inhomogenität im Stromfluss entlang der Bauteilbreite wurden diskutiert. Der Einfluss verschiedener Layout-Parameter auf den Wert von I_{HOLD} wurde ebenfalls untersucht.

Die in dieser Arbeit gewonnenen Ergebnisse sind wichtig für den Entwurf von Latch-up-sicheren und robusten ESD-Schutzgeräten.

Acknowledgement

I would like to express my deepest gratitude to my advisor Ao.Univ.Prof. Dipl.-Ing. Dr. Dionyz Pogany for his contribution and guidance throughout the development of this thesis. His profound knowledge, valuable suggestions and always being available for consultation made this period very fruitful time for me.

I would like to express my sincerest gratitude to Steffen Holland, Hans-Martin Ritter, Vasantha Kumar and Guido Notermans from Nexperia Hamburg for sharing their deep understanding and knowledge. The biweekly meetings that we made together helped the development of this thesis a lot. In addition, I would like to thank Steffen Holland for giving me a training about Synopsys Sentaurus TCAD.

I am grateful to Dr. Clément Fleury for giving me training about laboratory equipment and sharing his experience.

A special thank to Dr. Michael Heer and Dr. Matteo Rigato with whom I had fruitful cooperation.

My appreciation to Christine Brendt and Alexandra Linster for their administrative support and Erich Riegler, Johannes Prinzinger, Peter Kröll and Jürgen Smoliner for their technical support related to the institute. They made our lives easier in both the institute and the university.

I deeply thank Nexperia Hamburg and Institute of Solid State Electronics at Vienna University of Technology for providing me to work on this highly sophisticated research topic.

Finally, I would like to thank my mother Durdu, my father Bilal, my sister Elif and my brother Yusuf Emir for their love, patience and endless support.

I dedicate this thesis to the world peace and to animals under threat of extinction.

Contents

List of Figures

List of Tables

Abbreviations

Symbol	Meaning
AOM	**A**cousto-**O**ptic **M**odulator
BOX	**B**urried **Ox**ide
CDM	**C**harged **D**evice **M**odel
DC	**D**irect **C**urrent
DC-IV	**D**irect **C**urrent **I**ntensity **V**oltage characteristics
DUT	**D**evice **U**nder **T**est
EMMI	**Em**ission **Mi**croscopy
ESD	**E**lectro**s**tatic **D**ischarge
ESDA	**ESD** **A**ssociation
FPA	**F**ocal **P**lane **A**rray
HBM	**H**uman **B**ody **M**odel
HMM	**H**uman **M**etal **M**odel
IEC	**I**nternational **E**lectrotechnical **C**ommission
IR	**I**nfra**r**ed
ob-SCR	**o**pen-**b**ase **S**ilicon **C**ontrolled **R**ectifier
MM	**M**achine **M**odel
OSS	**O**N-**S**tate **S**preading
PW	**P**ulse **W**idth
RT	**R**ise **T**ime
SCR	**S**ilicon **C**ontrolled **R**ectifier
SFT	**S**equential **F**inger **T**riggering
Si	**Si**licon
SMU	**S**ource **M**easurement **U**nit
SOI	**S**ilicon-**o**n-**I**nsulator
TIM	**T**ransient **I**nterferometry **M**apping
TL	**T**ransmission **L**ine
TLP	**T**ransmission **L**ine **P**ulser
USB	**U**niversal **S**erial **B**us

Chapter 1

Introduction

1.1 Motivation

Since the invention of MOSFET by Mohamed M. Atalla and Dawon Kahng at Bell Labs in 1959 [1], scaling down and miniaturization became the driving force for the rapid growth of electronic semiconductor technology. The motivation behind this desire was both reducing fabrication costs, power consumption and increasing switching frequencies, device performance and market growth. This trend was even observed by Gordon Moore and formulated as Moore's Law in 1965 stating that the number of devices on a chip doubles every couple of years [2]. Miniaturization, on the other hand, owes its progress to the development in lithographic processes. Improvements in lithography provided mass production and smaller feature sizes.

Down-scaling of device dimensions, however, brought reliability issues into the field. As device sizes get smaller, power density in the active regions was increasing and this was resulting in various gradual device degradation such as electromigration in metal lines, time dependent dielectric breakdown, hot carrier degradation and abrupt failures like melting o metal lines, latch-up and thermal runaway. Further researches revealed that these failures and degradation are mostly due to electrostatic discharge (ESD) and electrical overstress (EOS) [3]. Hence, it turned out that special ESD protection elements which can prevent microelectronics from such damages during discharging events by clamping the transient voltages to safe levels are required.

The miniaturization process and faced challenges in microelectronics also lead to new developments in the ESD protection structures and so they showed a huge improvement since the first thyristor shown by Ebers in 1952 [4, 5]. Development of ESD protection units, however, are not based on fixed design rules. Therefore, they are needed to be adapted for each new device technology. For instance, high speed data interfaces like USB3 and Thunderbolt with data rates of 10 Gbps and 40 Gbps, respectively require ESD protection solutions with parasitic capacitance lower than 0.25pF [6, 7] so that the data signals can be transferred. Also, since integrated circuits (ICs) in such applications are very sensitive to the transient over-voltage, ESD protection solutions are wanted to have clamping voltages lower than 2.5 V [7, 8]. Furthermore, for system level protection, USB systems are often required to achieve robustness of the order of 15kV (IEC 61000-4-2 [9, 10]). On-chip protection solutions in that case become cost inefficient because of the large area consumption of the protection device itself to handle high current flow. Low capacitance demand, on the other hand, requires extremely low doped substrate [7, 8]. Discrete component technology based off-chip ESD protection structures in that case looks like a proper solution [6]. In this respect, in addition to fulfilling above mentioned requirements [11, 12], due to their low on-resistance (0.3 Ω) [7] and high failure current I_{t2} [6, 11, 13–15] properties, Silicon Controlled Rectifiers (SCR) becomes an effective remedy [11, 16–18].

While designing multi-finger SCR structures to reach robustness of the order of 30kV [14, 15], achieving simultaneous finger triggering became a long-standing goal of ESD engineers [19–23]. Generally, as it is observed in Human Body Model (HBM) pulses [24], in the case of long pulse rise times (RT>10ns), however, only a few fingers trigger at the beginning and when the voltage on the device reaches the trigger voltage V_{TR} again, next fingers trigger by resulting in an IV curve in zigzag shape [21]. Simultaneous finger triggering, on the other hand, is achieved in the case of short rise times due to e.g. dV/dt effect [19]. In this respect, it is worth to investigate and understand the mechanism of sequential finger triggering (SFT) under long pulse rise times so as to trigger fingers simultaneously or at least sufficiently fast [25] to meet high robustness requirements. Some other alternative methods like substrate or gate coupling were also proposed to trigger fingers simultaneously or subsequently [21–23].

Another important phenomenon that we may observe while designing SCR structures is the current filamentation [26] under quasi-static conditions. Depending on the device width, current may flow inhomogeneously [26] through the device width due to negative differential resistance (NDR)–induced instability [27–30] and so a current filament (CF) may emerge [26, 28–37]. The existence of CF, on the other hand, affects the determination of holding current (I_{HOLD}) value, which is the smallest current in the SCR on-state [26, 38]. Since for latch-up safe operations, high holding voltage (V_{HOLD}) and high holding current are often requested [39, 40], understanding the parameters that determines the CF formation and I_{HOLD} becomes a significant research topic. Due to its dependence on device width, CF is a 3D phenomenon and since 2D TCAD simulation always considers a homogeneous current flow along the device width, its observation cannot be done with 2D or relatively short width 3D TCAD simulation structures. 3D TCAD simulation of structures with relatively long widths, on the other hand, is a very delicate, time and resource consuming task. To our knowledge, in addition, 3D TCAD has not been applied to I_{HOLD} analysis yet.

1.2 Scope and Outline

In the first chapter, a brief introduction to electrostatic discharge (ESD) (section 1.3), some important ESD qualification standards (section 1.4), state-of-the-art ESD investigation methods (section 1.5) as well as silicon controlled rectifier (SCR) (section 1.6) is given.

In the second chapter, triggering behavior of multi-finger SCRs with substrate coupling are investigated under a HBM-like TLP stress (section 2.1) and a Surge-like half sinusoidal pulse (section 2.2) both experimentally and by TCAD simulations. In section 2.1, the rise time dependent simultaneous and sequential finger triggering mechanisms are explained and in section 2.2, the reason behind the preferred direction for sequential finger triggering is revealed. Besides that, in both studies, effect of different pulse variations and layout changes are studied to deepen the understanding.

In the third chapter, filamentary states in SCRs observed under quasi-static conditions are investigated both experimentally (section 3.1, 3.2 and 3.3) and by TCAD simulations (section 3.4 and 3.5). The 3D TCAD simulation methodology to create double hysteresis filamentary IV behaviour observed in experiments is explained (section 3.4) and applied to determination of I_{HOLD} (section 3.5.1). The effect of different layout parameters on the value of I_{HOLD} is also studied (section 3.5.2) and the differences between the 2D and 3D TCAD results are emphasized.

Finally in the conclusion and prospects part, the main findings of this PhD thesis are summarized.

1.3 ESD

When two objects at different potentials get very close to or touch each other, the one which has higher potential, discharges into the other one due to dielectric breakdown or electrical short, respectively by causing a flow of electrons for a short time. This sudden current flow event is called as electrostatic discharge (ESD). The buildup of charges on the objects can be due to electrostatic induction or triboelectricity. Although the energy of discharging is low and it happens in a very short duration (in the range of ns), since microelectronic circuits are small, fatal device degradation and failures in the ICs can still occur due to high enough dissipated power density. Different parameters such as the relative humidity of the surrounding atmosphere, capacitance between the objects and resistivity of the objects affects duration and density of the electron flow.

ESD can be observed in our daily lives from large scales like lightening in air, to small scales such as electric sparks while touching a contact pin after walking along carpets or while taking out a woollen sweater. In spite of the advancement in packaging technology and developments in the integrated circuit production techniques, around 30% and 40%

of total microelectronic circuit failures still stems from ESD events [41, 42].

Figure 1.1 shows an example of device failure due to ESD on a multi-finger SCR structure. At a very high ESD current pulse, metal wires overheats and so evaporates leading an open connection. Figure 1.1 (a) is the infrared image from backside of the device whereas Figure 1.1 (b) is the top image under visible light. Both pictures belongs to the same device; however, in Figure 1.1 (b) since the left part of the device stays under the contact pad, all fingers are not visible.

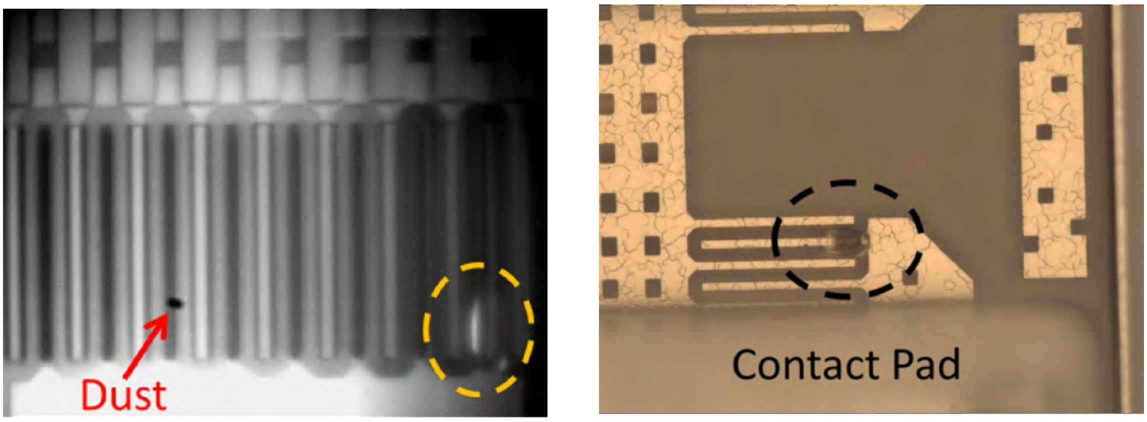

(a) **(b)**

Figure 1.1: (a) Backside infrared and (b) top side visible light image of a device failure

1.4 ESD Models

Since ESD protection components should handle various type of electrostatic discharging events that microelectronics circuits can encounter during their production and usage, ESD Association (ESDA), and industry agreed to define standardized models that can reproduce similar ESD stress conditions on the device under test (DUT) by a lumped equivalent circuit. Three common standard ESD models are Human Body Model (HBM) [43, 44], Charged Device Model (CDM) [45] and Machine Model (MM) [46]. These three standards will be investigated in the next sections but since we have also investigated sequential finger triggering (SFT) under a half-sinusoidal current waveform which mimics a surge, IEC 61000-4-5 standard [47] defined by International Electrotechnical Commission (IEC) will also be analyzed.

1.4.1 Human Body Model (HBM)

1.4.1.1 Component Level HBM

The Human Body Model (HBM) is implemented to mimic the discharge of a standing electrostatically charged human being into a grounded integrated circuit compound through his/her pointing finger tip. This model is beneficial in terms of providing a rating about failures which can be encountered in manufacturing environment during component assembly, packaging, and shipping.

Figure 1.2 (a) shows the equivalent lumped circuit model of HBM [43, 44, 48–50]. With the touch of a human being, 100 pF capacitor which is approximately the capacitance of the human body, first charged up by the high voltage supply. Then, it discharges to device under test (DUT) through 1.5 kΩ resistor which is modeling the resistance of the finger.

The discharge process is approximated by the circuit design shown on Figure 1.2 (c). The circuit is designed with LTspice [51]. In order to simulate the transient current on a 50 Ω load (Rdut) under 2kV high voltage source, the charged up capacitor is emulated by defining a 2kV initial condition voltage on the 100pF capacitor. The resulting transient current is presented in Figure 1.2 (b). The simulation gives a normal pulse duration from 150ns to 160ns and a typical risetime of 10ns. Ihus, HBM shows a slow transient response compared other common standard ESD models. In addition to all of these, currently 1-2 kV HBM requirements are expected to meet.

1.4.1.2 IEC 61000-4-2 based Human Metal Model (HMM)

As component handling started to be performed under controlled ESD environment by using ESD protective gears, ESD stress on the components decreased drastically. Therefore, component level HBM turned out to be a soft test. In this respect, so as to get failure ratings under uncontrolled environments where ESD levels can go up to 40 kV, a new model named Human Metal Model (HMM) was needed to be established [9]. HMM imitates the discharging of a charged person through a metal object, like a screw driver, to a grounded system. A human being can be charged up to 40 kV while plugging and unplugging cables.

IEC 61000-4-2 based HMM is a system level method and hence instead of a single component, a combination of pins are stressed. HMM, from this point of view, defines ESD standards much stronger than the component level HBM and CDM. Figure 1.3 (a), (b) and (c) show the equivalent lumped circuit model, the transient current from the LTspice model and LTspice schematic, respectively. The inductor L1 with 2.4 µH value in Figure 1.3 (c) represents the compulsory ground strap with 2 m length. The first peak in Figure 1.3 (b), on the other hand, originates from parasitic or lumped parasitic elements [52].

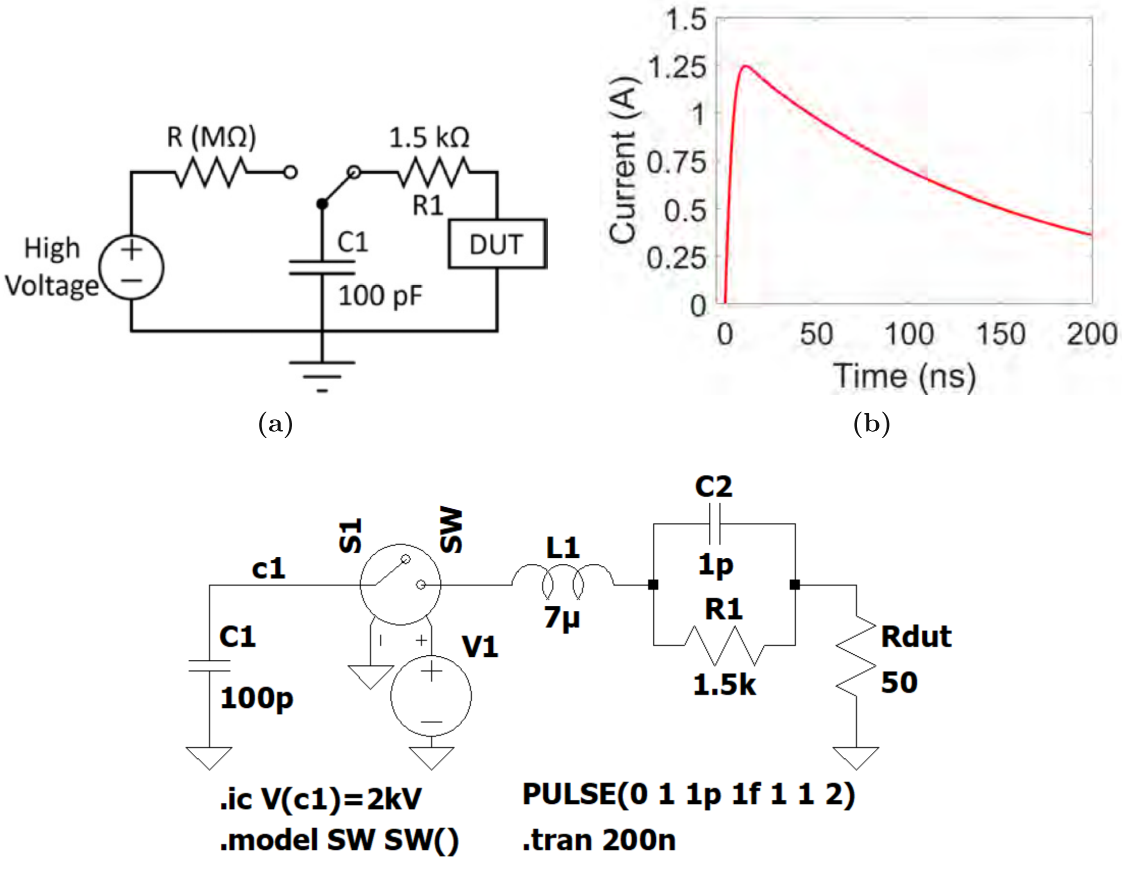

(a) (b)

(c)

Figure 1.2: (a) HBM equivalent lumped circuit model (b) HBM transient current for 2kV high voltage source (c) LTspice simulation schematic for HBM [43, 44, 48–50]

Apart from ESD generator models (compare Figures 1.2 (a) and 1.3 (a)), the main distinctions between HBM and HMM are the pulse rise times, amount of peak currents and the number of ESD strikes. Rise time in HBM is around 10 ns whereas in IEC 61000-4-2 based HMM, it is less than 1 ns. Thus, a device passed from HBM test may fail in HMM test. Similarly, due to different peak currents, a test device survive under 4 kV HBM may be degraded with 2 kV IEC-ESD. Lastly, as for the number of ESD strikes, in HBM one positive and one negative stresses are needed to apply; however, in HMM a minimum of 10 positive and 10 negative strikes are required. So again, it is a high probability that a device may survive in HBM test but fail in HMM during one of the subsequent stresses.

Since HBM and HMM has non-flat waveform characteristic, in this work, we used Transmission Line Pulse (TLP) instead of HBM and HMM. However, since with all methods equivalent energies can be provided on DUT [53, 54], their results are related.

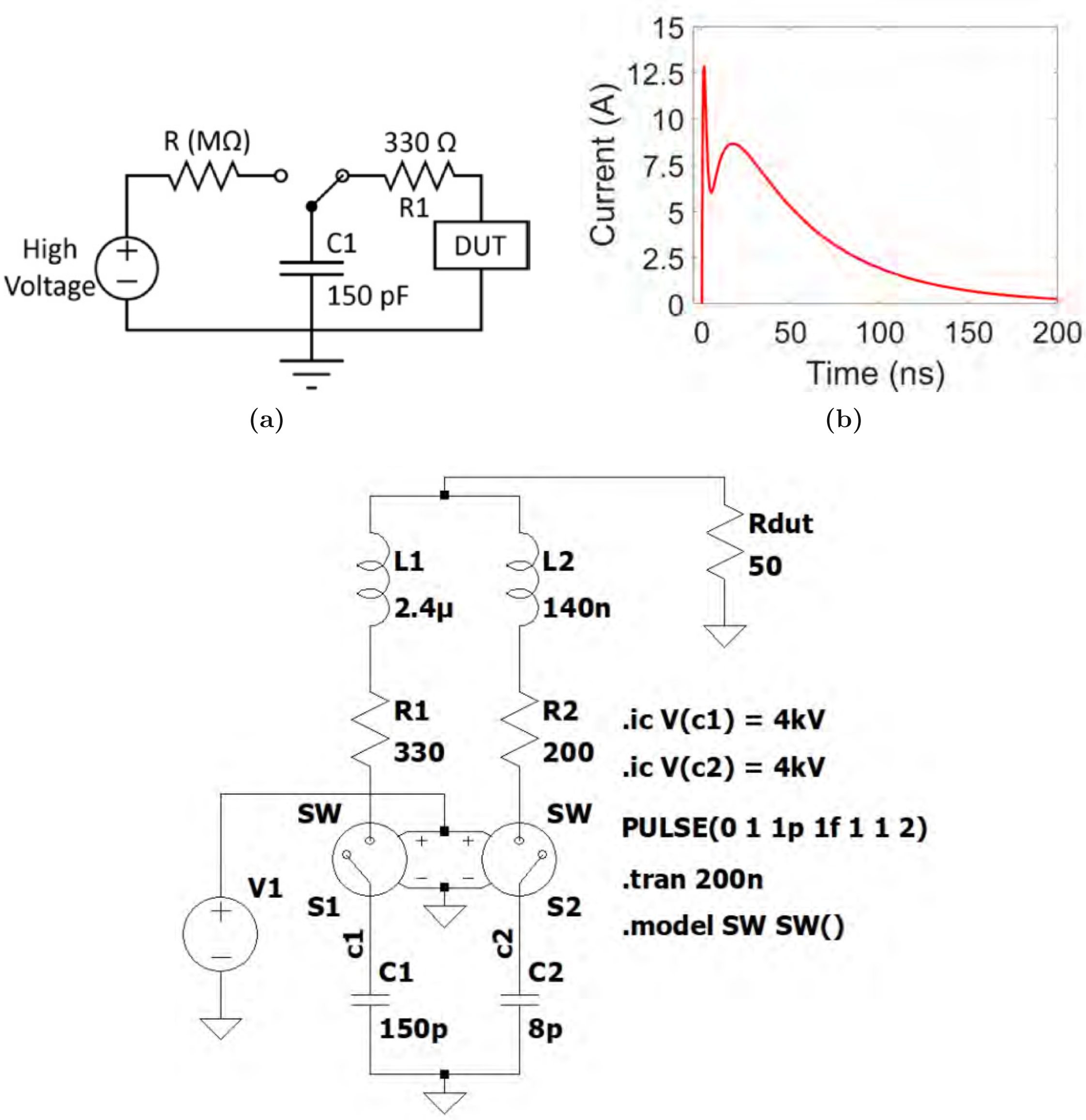

(a) (b)

(c)

Figure 1.3: (a) HMM equivalent lumped circuit model (b) HMM transient current for 4kV high voltage source (c) LTspice simulation schematic for HMM [9, 50, 52]

1.4.2 Charged Device Model (CDM)

During manufacturing, while integrated circuits are sliding over insulators in automated assemblers they may charge up. Then, when these charged devices contact with a conductive surface with a lower potential, they rapidly discharge to ground through this conductive object. This discharging event is called as Charged Device Model (CDM). Current waveforms of CDM show a very fast rise time due to very low inductance values (L1≤100 nH and R1≤25 Ω, see Figure 1.4 (a)) and so they can cause a gate oxide failure.

Figure 1.4 (a), (b) and (c) show the equivalent lumped circuit model, the transient current from the LTspice model and LTspice schematic, respectively. In Figure 1,4 (c) a 5pF C1 capacitance discharges into ground through L1 (10 nH inductor), R1 (10 Ω resistor) and C2 (5 pF stray capacitance).

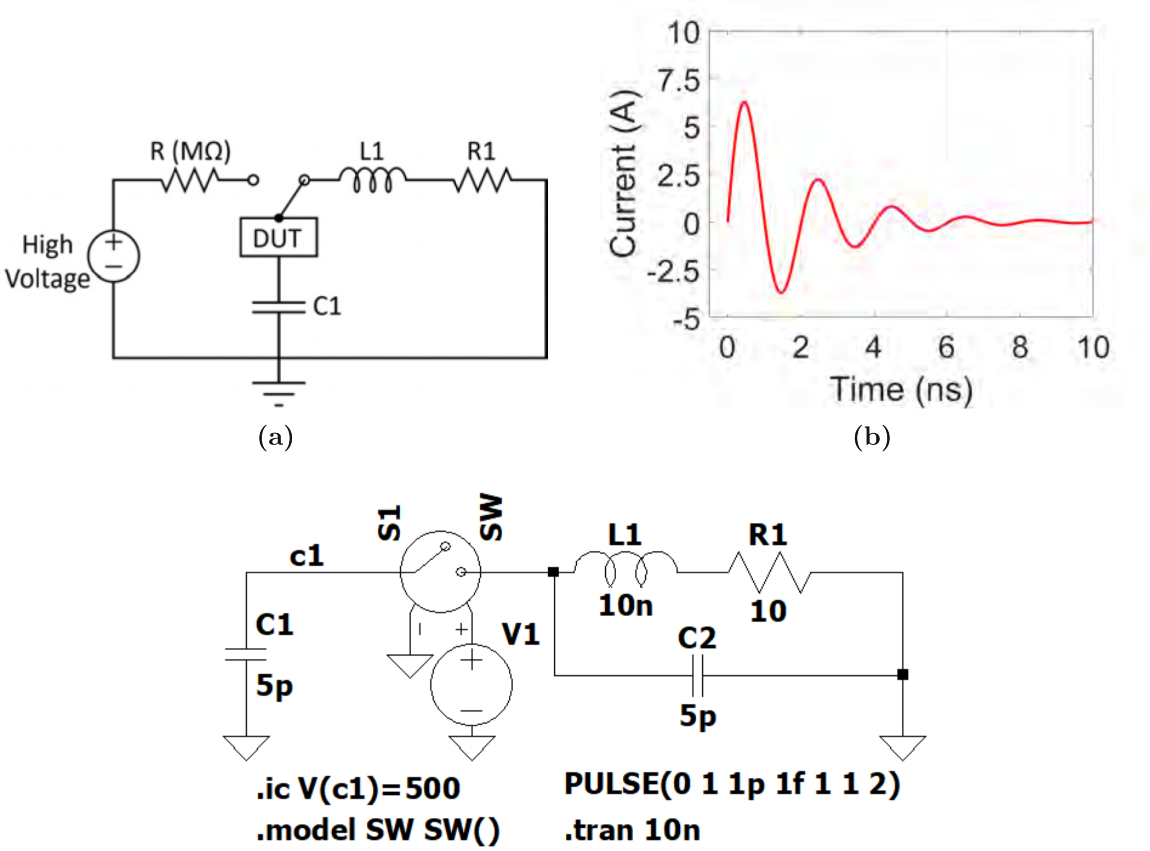

(a) (b)

(c)

Figure 1.4: (a) CDM equivalent lumped circuit model (b) CDM transient current for 500V high voltage source (c) LTspice simulation schematic for CDM [48, 49]

1.4.3 Machine Model (MM)

During the production of ICs, some equipment like metallic handling tools, charged cables and metal contacts on a charged board may discharge into ground through ICs. This event is described by Machine Model (MM). The equivalent lumped circuit model of MM, as shown in Figure 1.5 (a), is very similar to that of HBM but since MM does not include a resistor between the discharging 200pF capacitor (C1) and DUT, it is also called as the 0 Ω model [55]. Due to this zero resistance, however, the energy is dissipated mainly on the IC.

MM was discovered while trying to find the worst case HBM event [56]. Failure types in MM testing; therefore, are similar to ones observed in HBM testing. However, in general the applied stress levels in HBM is 10 times higher than that of MM. For example, the typical protection voltage level for HBM is around 2 kV whereas for MM it is around 200V. Thus, it can be stated that MM ESD robustness can be guaranteed by the HBM ESD test. Because of these facts actually, MM ESD has begun to be used less frequently compared to HBM ESD test. Even recently, some ESD people have started to complain about the redundancy of MM to HBM [57].

In Figure 1.5 (c) we observe the LTspice schematic for MM and Figure 1.5 (b) shows the transient voltage waveform on DUT (50Ω resistance) from LTspice simulation.

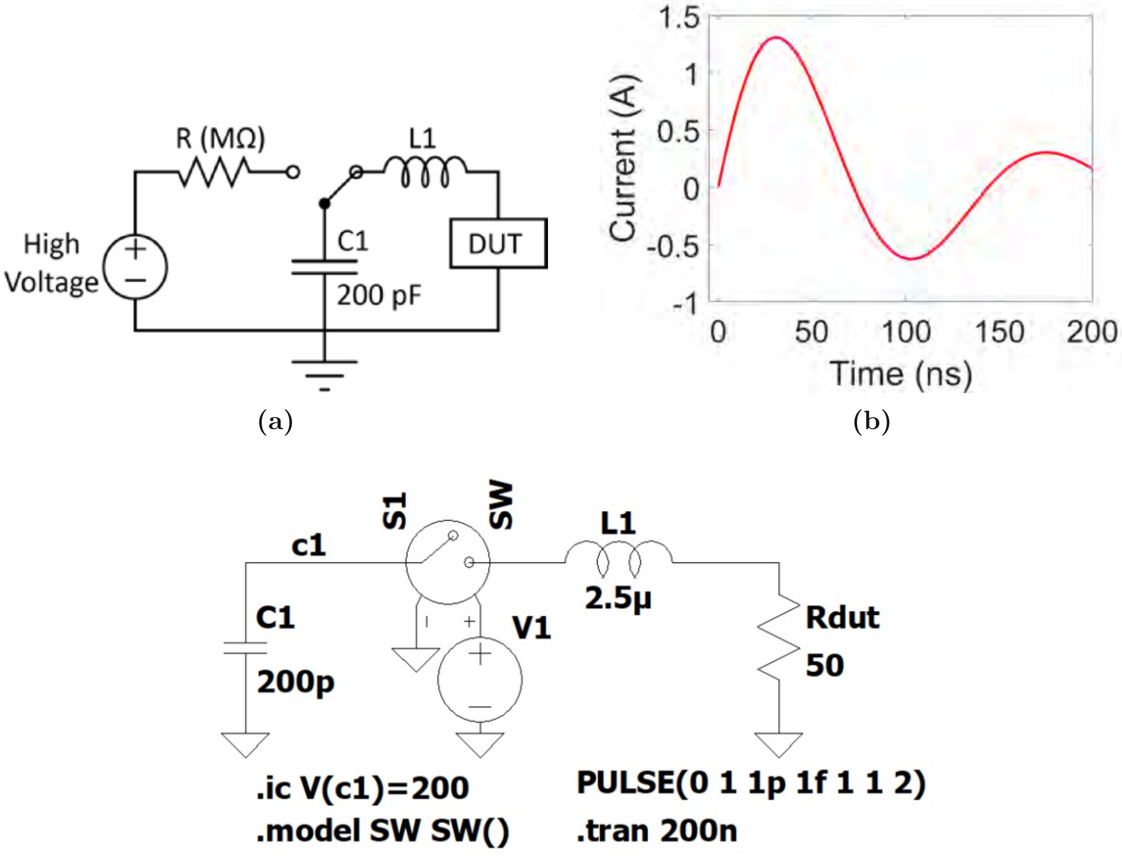

(a) (b)

(c)

Figure 1.5: (a) MM equivalent lumped circuit model (b) MM transient current for 200V high voltage source (c) LTspice simulation schematic for MM [48, 49]

1.4.4 Surge Model

Surge immunity standard also known as IEC 61000-4-5 is a system level ESD protection and it addresses the immunity requirements of unidirectional surges generated by overvoltages from switching and lightning strikes. Switching transients can be caused by power system switching, resonating circuits related to switching devices, load changes in power distribution systems and short circuit faults. Lightning transients, on the other hand, may stem from a direct strike or induced currents and voltages after an indirect strike [47].

Two surge waveforms are specified with IEC 61000-4-5: the 1.2 x 50 µs voltage waveform for an open-circuit DUT and the 8 x 20 µs current waveform for a short-circuit DUT. There, 1.2 µs and 8 µs indicates the front times whereas 50 µs and 20 µs specifies time to half values [47].

Since SCR devices we are using in this work have around 1 Ω resistance, we used the 8 x 20 µs short-circuit current waveform model. Figure 1.6 (a), (b) and (c) show the equivalent lumped circuit model for Surge model, the transient current on the 1Ω resistance (Rdut) from the LTspice simulation for a 2kV high voltage source and LTspice schematic [58], respectively.

In Figure 1.6 (a) R1, L1, R2 and C1 are named as impedance matching resistor, rise time shaping inductor, charging resistor and energy storage capacitor, respectively. R3 and R4, on the other hand, are called as pulse duration shaping resistors.

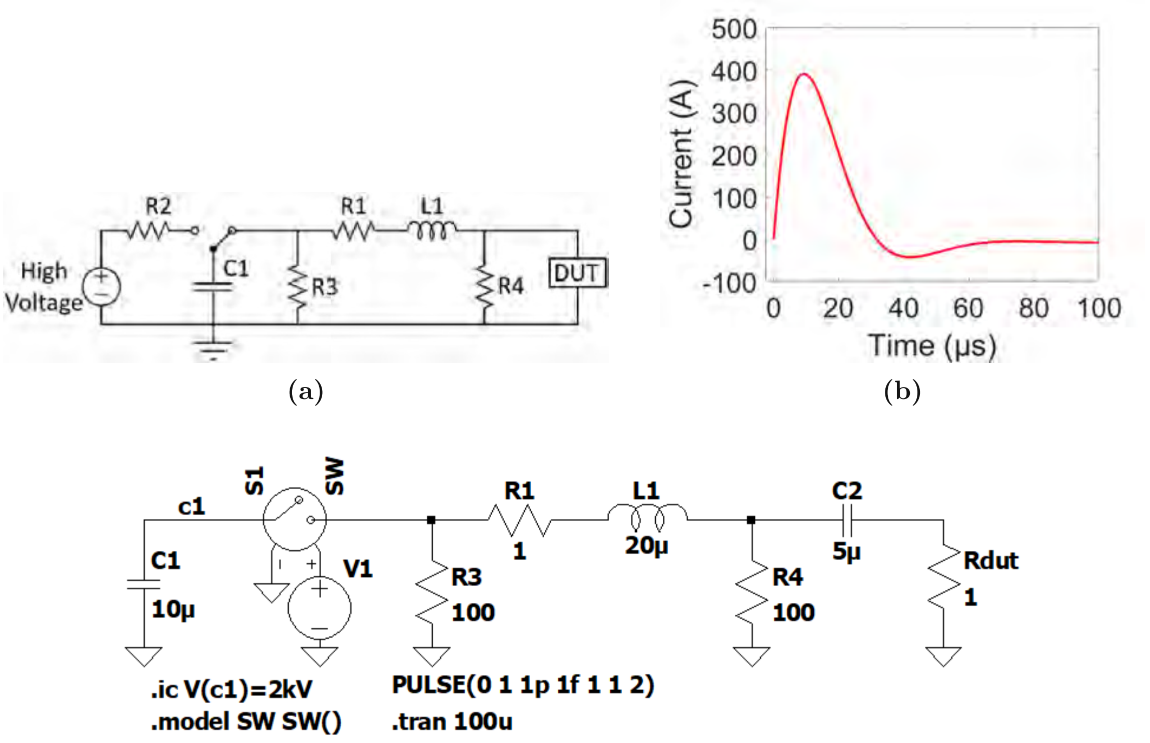

(a)

(b)

(c)

Figure 1.6: (a) Surge model equivalent lumped circuit model (b) Surge model transient current for 2kV high voltage source (c) LTspice simulation schematic for Surge model [47, 58]

1.5 Investigation Methods

In the following there subsections I will introduce the investigation methods we carried out in this work. Within these methods, Transmission Line Pulser (TLP) is an electrical method whereas Transient Interferometric Mapping (TIM) and Emission Microscopy (EMMI) are optical techniques.

1.5.1 Transmission Line Pulser (TLP) System

The motivation behind for the development of TLP is to give a useful approximation for HBM ESD pulse. TLP allows us to have current and voltage waveforms in HBM time domain. Since TLP pulse is in the rectangular and HBM is in a non-flat shape, This approximation is valid in terms of the applied energies on DUT, not current and voltage transients [53, 54]. The best approximation for HBM in TLP setup is obtained with 100 ns Pulse Width (PW) and 10 ns Rise-Time (RT) configuration [27].

TLP system allows us to vary the load line, rise-time and pulse width values. That is why, since its invention by Maloney and Khurana in 1985, it gained a huge popularity [59] and widespread usage. However, its biggest disadvantage is pulse width (duration) inflexibility. Separate transmission lines (TL) are necessary for each pulse width.

In this work, we employed a 4-point-probe TLP system from HPPI [60] as shown schematically in Figure 1.7. A 2-point-probe TLP setup is also possible. The biggest distinction between these two configurations is the contact resistance. In 4-point-probe TLP configuration, contact resistance is cancelled whereas in 2-point-probe TLP system it is not and so voltage is needed to be corrected according to the contact resistance.

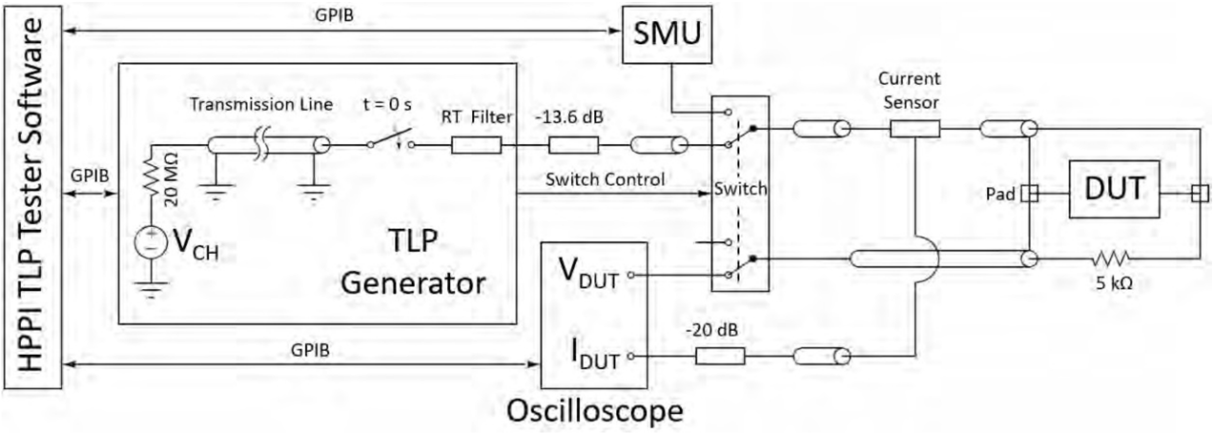

Figure 1.7: Schematic of a 4-point-probe TLP setup

In Figure 1.7, the transmission line (coaxial cable) with 50 Ω characteristic impedance and length l is charged up through the 20 MΩ resistor by the high voltage source V_{CH}. The length of transmission line is determined according to desired pulse duration (PW).

Since the rectangular pulse waveform travels the transmission line twice [60], the desired length becomes

$$l = \frac{v \cdot \mathrm{PW}}{2} \tag{1.1}$$

where v is the propagation speed of the pulse in TL and its value is 20 cm/ns (generally polytetrafluoroethylene (PTFE or Teflon) is employed as the inner insulator of TL [60]). The high voltage source can provide voltages between -1.5 kV and +1.5 kV. However, in order to protect the TLP generator from the effect of reflected waves, we put a 13.6 dB attenuator in front of its output. Therefore, the maximum voltage we can have on DUT is ±300 V (= ±6 A in the case of 50 Ω TL impedance). Rise time (RT) filters apply a low-pass filter on the generated pulse and smooths its edges. The available rise time values in our TLP setup is 300 ps, 1 ns, 10 ns and 50 ns.

As a current sensor we have two options: Tektronix CS-CT1-3003A and CS-CT2-3003A. Due to their different frequency responses, we used CT1 for pulses shorter than 200 ns and CT2 for the rest. In addition, CT1 and CT2 provide 5 V/A and 1 V/A sensitivity, values respectively. We also employ a 20 dB attenuator in front of the I_{DUT} channel of the oscilloscope to protect it from high voltages. Therefore, in the case of CT1 and CT2 we set the current scaling factor as 2 and 10 in the HPPI TLP Tester software, respectively. Similarly, since we probe the voltage on the device with 5 kΩ probe needle and since the channel resistances in the oscilloscope is 50 Ω, we set the voltage scaling factor in the HPPI TLP Tester software as 100. As probe tips we use GGB Picoprobe Model 10 needles.

TLP measurement is conducted by applying step by step increasing TLP voltage pulses on DUT to acquire TLP-IV curve with current and voltage waveforms, and measuring DC leakage current at a certain DC voltage after each step. Switching between these two cases is controlled by the *Switch* shown in Figure 1.7. Typical current and voltage waveforms on a SCR device under the conditions of RT = 10 ns and PW = 100 ns are shown in Figure 1.8 (a) and (b), respectively. For every applied TLP pulse, measured TLP voltage and TLP current waveforms on DUT are averaged over a selected time window, which is in practice between 70% and 90% of PW, to reduce the impact of current and voltage undulations within a single stress. Then, with all these averaged values, quasi-static TLP-IV characteristic is acquired as shown in Figure 1.8 (c).

In order to carry out DC leakage current measurement after each TLP voltage pulse, we employed Keithley 2410 as our a Source Measurement Unit (SMU). A typical leakage current plot can be observed in Figure 1.8 (d). Lastly, the digital oscilloscope we used is LeCroy WaveRunner 104MXi.

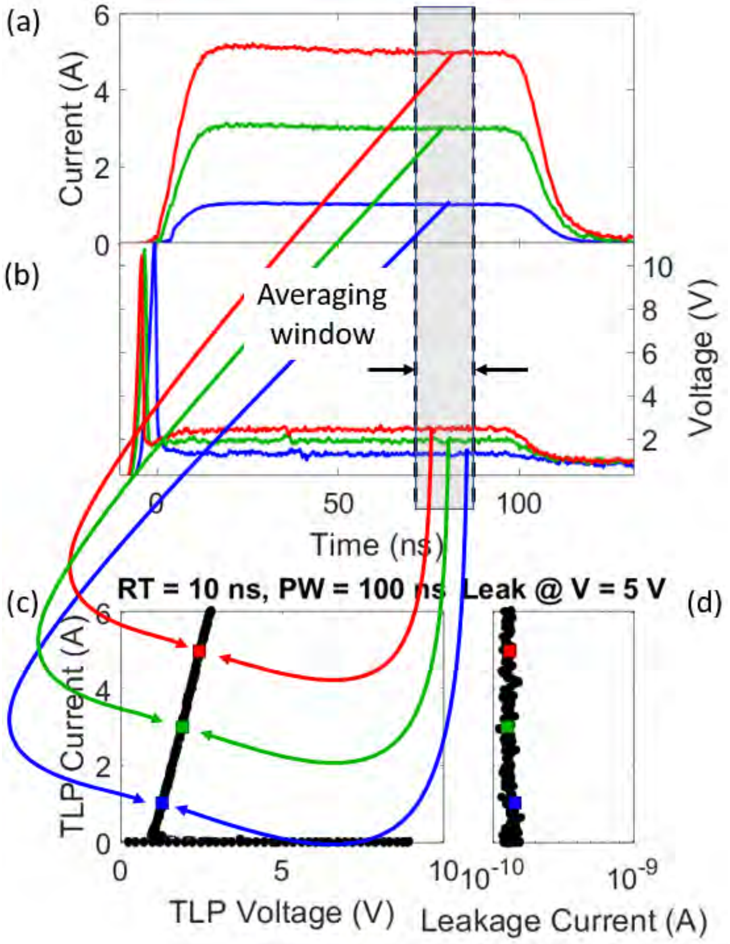

Figure 1.8: An example of (a) transient current and (b) transient voltage on a SCR device measured by a TLP setup for RT = 10ns and PW = 100 ns. (c) TLP-IV curve obtained by averaging related current and voltage waveforms over the selected averaging time window. (d) An example of leakage current plot

1.5.2 Transient Interferometric Mapping (TIM) Technique

Transient Interferometric Mapping (TIM) technique is a non-destructive method and it is based on the measurements of the local transient variations in the semiconductor refractive index Δn due to free carrier concentration (plasma-optical [61] effect) and temperature (thermo-optical [62] effect) changes under the TLP stress [63–67]. The principle of method can be observed in Figure 1.9 (a). In this technique, first of all, a certain TLP stress and scanning path are defined. An example of the scanning path across the fingers of a multifinger device is shown in Figure 1.9 (b). Then, while the laser probe beam is scanning every scanning path position of DUT from its polished backside, the TLP pulse is applied to DUT repetitively in two-point configuration with a repetition rate of about 1 Hz. It is important to have a polished backside so as to reduce scatterings due to surface roughness. Moreover, the low repetition rate allows the device to cool down between subsequent pulses. The number of TLP pulses at each position, on the other hand, determines the signal-to-noise ratio of the extracted phase shift from the heterodyne signal. Since DUT may show pulse-to-pulse instabilities, in order to improve signal-to-noise ratio, the average of several extracted phase shift is taken.

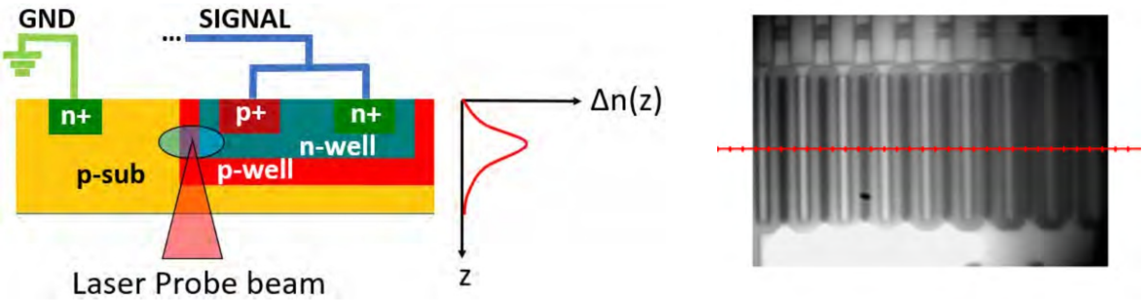

(a) (b)

Figure 1.9: (a) The principle of TIM technique (b) An example of the scanning path across the fingers of a multifinger device

TIM technique we use has 3ns time and 1.5um space resolution [68]. The schematic of the setup can be observed in Figure 1.10. The wavelength of the used laser beam is 1.3 µm; therefore, semiconductors with bandgap energies greater than 0.95 eV (including low doped silicon) becomes transparent. The word heterodyne indicates a mixing to an intermediate frequency. Mixing is achieved by the Acousto-Optic Modulator (AOM) with a 80 MHz frequency signal and so the frequency of the laser probe beam is shifted by 160 MHz compared to the reference beam. This frequency range is suitable for short pulses in the order of 100 ns. Both shifted frequency and reference beam signals interfere at the detector by creating a 160 MHz beating signal with a phase equal to the phase of the probe beam. The resulting current and voltage waveforms in addition to heterodyne signal from detector is collected with a digital oscilloscope. In the case of long pulses like surge pulse, sampling the 160 MHz heterodyne signal in oscillator may take up a lot of space in the computer memory. In this case 160 MHz heterodyne signal can be modulated with a 159 MHz external signal and the output of this modulation can be filtered by a low-pass filter with cutoff frequency of 5 MHz. Then, the resulting 1 MHz signal can be feed up to digital oscilloscope for sampling. By doing like that we will gain memory space in the expense of loosing time resolution.

In order to position the device on the setup, a stage with 100 nm minimum step size is used. For this purpose, a broadband light enlightens DUT from its backside and the real-time infrared view captured by InGaAs Focal Plane Array (FPA) Infrared camera is shown on a monitor. By playing with the stage and looking at the monitor, device is positioned. This stage is also controlled automatically by a computer program during measurements and so the device is brought to each new scanning probe position automatically after

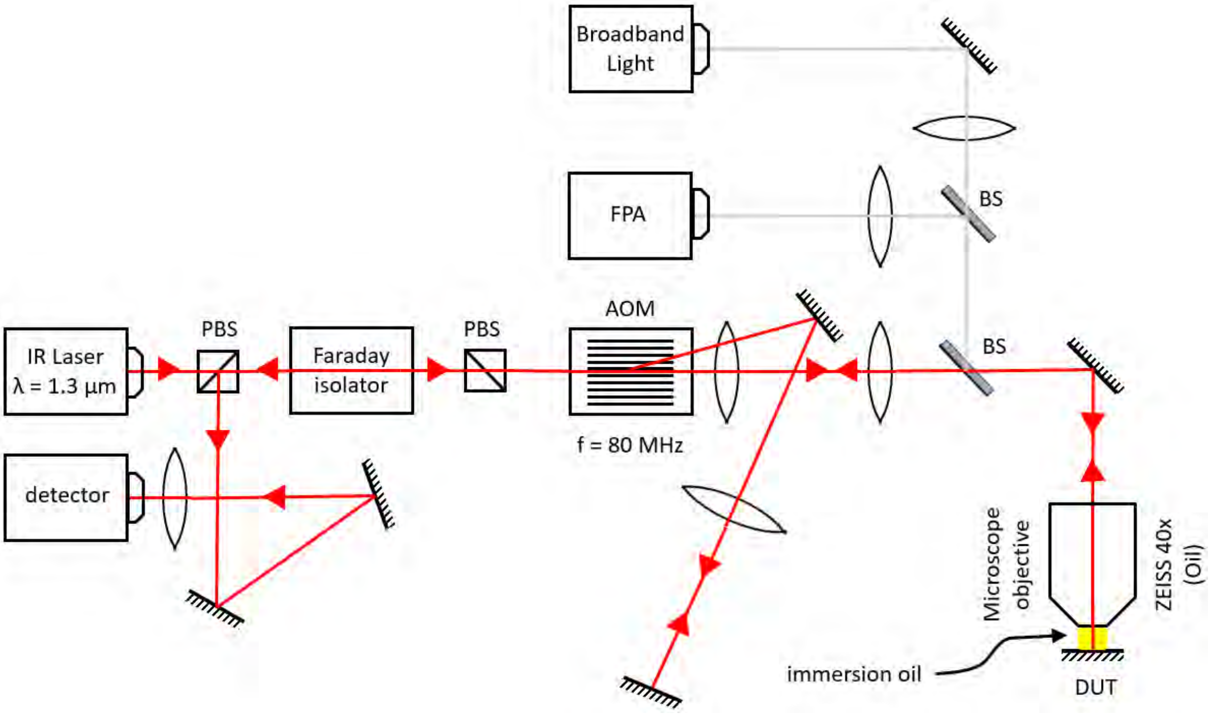

Figure 1.10: The schematic of TIM setup

the measurements on the previous position is done. Broadband light and FPA infraraed camera, on the other hand, are turned off during measurement. To check whether DUT suffers from a cumulative damage or not, a DC-IV measurement with Keithley 2410 is performed after completing the scan at each scanning position. For this purpose a switch as shown in TLP setup is used to provide the connection between the device and SMU.

As for detection of the local transient variations in the semiconductor refractive index Δn, phase shift variation $\Delta\phi$ in heterodyne signal is used. By including contributions from both plasma-optical and thermo-optical effects, the refractive index change in a medium can be written as

$$\Delta n(x,y,z,t) = \Delta n_{th}(x,y,z,t) + \Delta n_e(x,y,z,t) + \Delta n_h(x,y,z,t) \tag{1.2}$$

where Δn_{th} is the component due to temperature change (ΔT); and Δn_e and Δn_h are parameters due to electron and hole concentration variations, respectively. Then, since wave number is

$$k = 2\pi/\lambda \tag{1.3}$$

refractive index change results in a phase shift in the probing laser beam, stated as

$$\Delta\phi(x,y,t) = 2\cdot k \int_{z=bottom}^{z=top} \Delta n(x,y,z,t)\, dz = 2\cdot \frac{2\pi}{\lambda} \int_{z=bottom}^{z=top} \Delta n(x,y,z,t)\, dz \tag{1.4}$$

there the factor 2 is due to two times (forward and backward) traveling of the laser beam. So the total measured phase shift is proportional to integral of change in the refractive index along the beam path.

The resulting optical phase shift is a superposition of temperature and free carrier induced contributions. Temperature increase causes a positive phase shift whereas free carrier concentration results in a negative phase shift. Since the negative phase shift due to the carrier injection is dominant in our investigated SCR devices at short times, it is used to probe the onset of the SCR activity in fingers. In a long pulse duration, however, termally induced phase shift term Δn_{th} dominates and so the phase shift equation above reduces to

$$\begin{aligned}\Delta\phi(x,y,t) &= 2\cdot\frac{2\pi}{\lambda}\int_{z=bottom}^{z=top}\Delta n_{th}(x,y,z,t)\,dz\\ &= 2\cdot\frac{2\pi}{\lambda}\int_{z=bottom}^{z=top}\frac{dn}{dT}\Delta T(x,y,z,t)\,dz\end{aligned} \tag{1.5}$$

At our laser beam wavelength (λ=1.3 µm), it was found that the thermo-optical coeffecient $\frac{dn}{dT}$ of silicon around 320 K is approximately $1.9\cdot10^{-4}$ K^{-1} [62].

Figure 1.11 shows an example of phase shift (in rad.) for an SCR under I=3A TLP pulse with the condition of 100 ns pulse width (PW) and 300 ps rise time (RT). The TLP pulse starts at t=0 and and ends at t=100 ns. As it can be seen, a negative phase shift occurs at the beginning of the pulse due to free carrier injection. However, later due to heating of the device, temperature increases and phase shift moves towards positive values. When the applied stress ends, the device starts to cool down and so the phase shift value decreases.

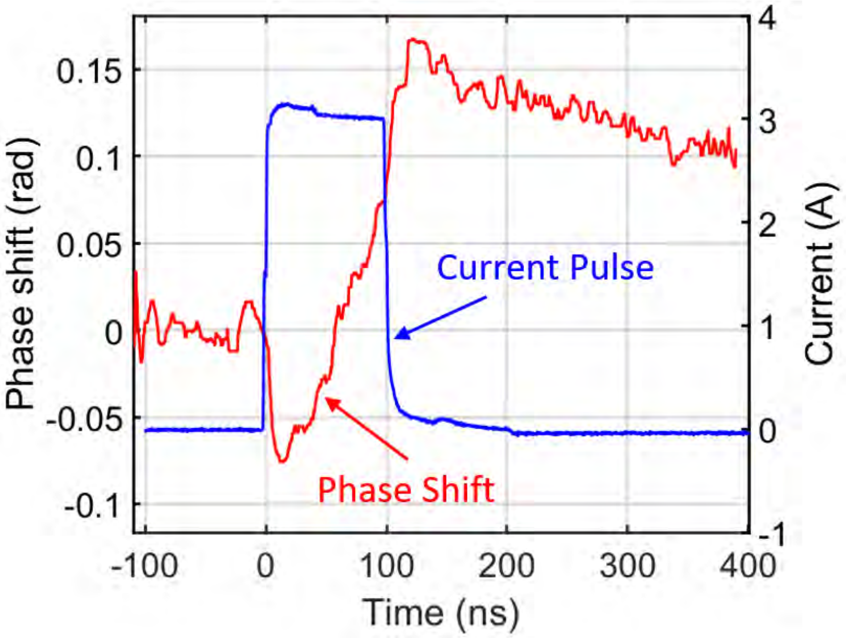

Figure 1.11: Phase shift for an SCR under I=3A TLP pulse with the condition of PW = 100 and RT = 300 ps

The biggest drawback of TIM technique arises when dealing with devices which have multiple layers. In that case, phase shift calculation becomes quite complicated due to constructive and destructive interference.

1.5.3 Emission Microscopy (EMMI)

Silicon under DC stress emits light in infrared spectrum [69, 70]. Therefore, Emission Microscopy (EMMI) depends on the idea of capturing infrared images of a silicon based device while it is conducting current. Figure 1.12 shows the schematic of EMMI setup. The camera we use is InGaAs Focal Plane Array (FPA) infrared camera. EMMI setup is a modified version of TIM setup and the device is again imaged from its backside. As the stress source, however, DC (either Keithley 2410 Source Measurement Unit or HP4155A Semiconductor Parameter Analyzer) and repetitive pulses (HP8114A Pulse Generator) are used.

The property that makes EMMI a very effective and beneficial tool is its facility for real-time observation. In EMMI setup, the infrared pictures are shown on a monitor while measurement is going on. Therefore, one can quickly understand device behavior and observe possible failure locations and homogeneous/inhomogeneous current flow.

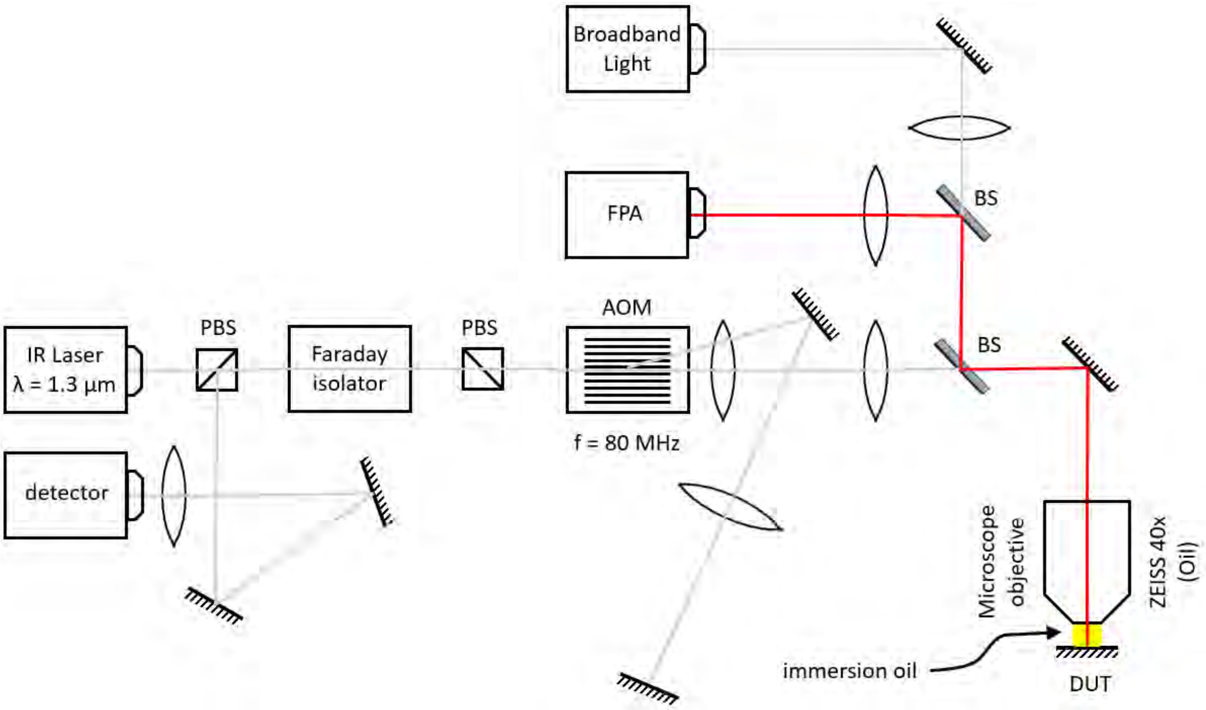

Figure 1.12: The schematic of EMMI setup

1.6 Silicon Controlled Rectifier (SCR)

An SCR basically consists of a pnp transistor, an npn transistor and their corresponding base resistances. The collectors of pnp and npn transistors also serve as the base of npn and pnp transitors, respectively. Therefore, all together forms a pnpn structure. Figure 1.13 (a), (b) and (c) show the 2D cross-section view, equivalent circuit and IV curve of an SCR, respectively.

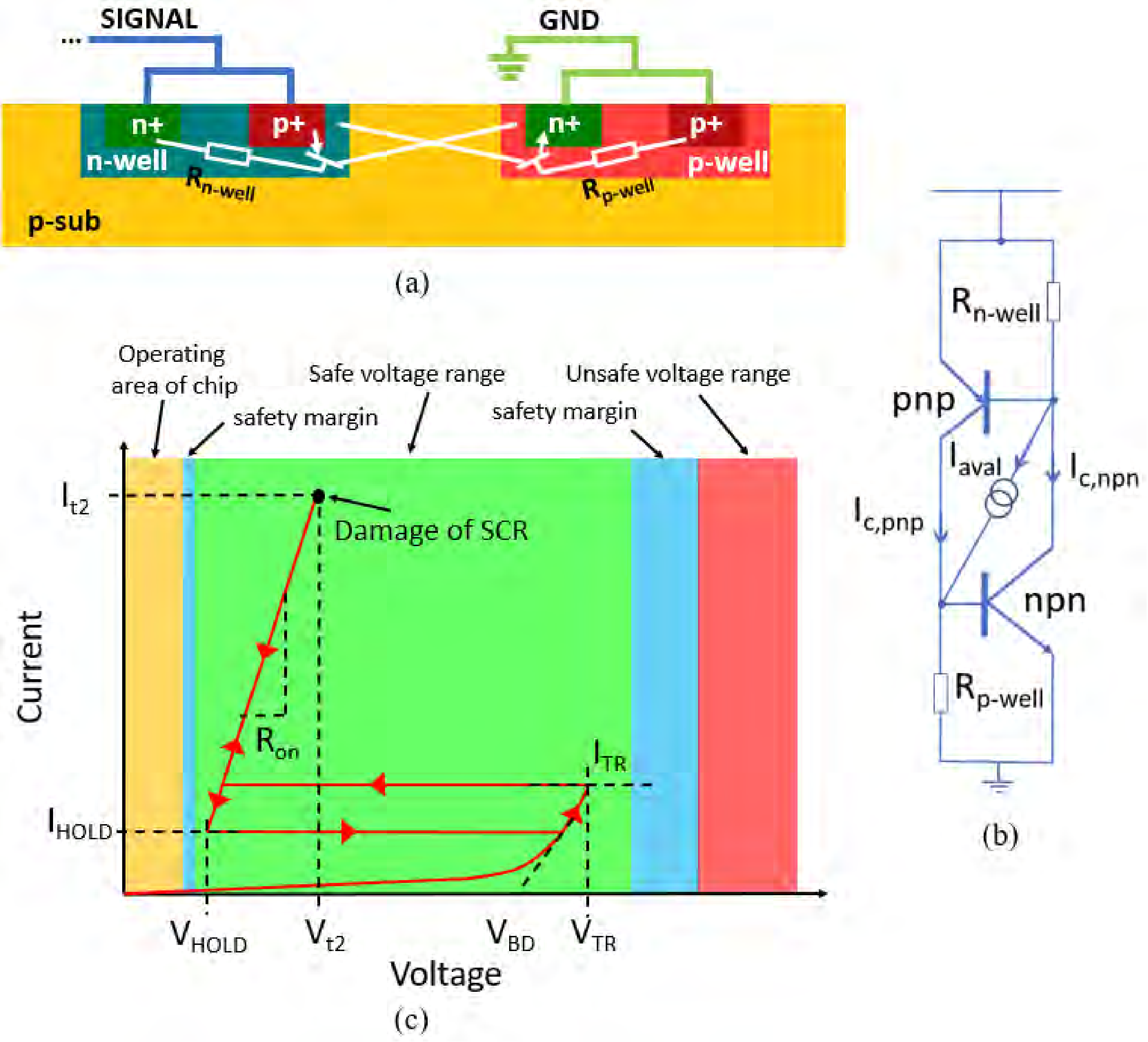

Figure 1.13: (a) 2D cross-section view (b) equivalent circuit and (c) IV characteristic of an SCR

An SCR is connected in parallel to a circuit that is desired to be protected so that they share the same voltage. Ideally an SCR stays in the idle state as an open circuit while the protected circuit is working within its operating voltage range. In a real SCR, of course, there exist some leakage current. Then, if an ESD stress emerges on the protected device, the voltage on both SCR and the protected circuit start to rise. So that means npn and pnp transistor currents $\mathrm{I_{c,npn}}$ and $\mathrm{I_{c,ppn}}$ start to increase. At this stage p+/n-well and p-well/n+ junctions stay in forward bias whereas n-well/p-sub(p-well) junction stays in reverse bias. Then, if the voltage on the SCR and the protected circuit increases more and becomes higher than breakdown voltage $\mathrm{V_{BD}}$, an avalanche process (impact ionization) starts at the reverse biased n-well/p-sub(p-well) junction. The resulted avalanche current ($\mathrm{I_{aval}}$) simply is

$$\mathrm{I_{aval}} = (\mathrm{M} - 1) \cdot (\mathrm{I_{c,npn}} + \mathrm{I_{c,pnp}}) \tag{1.6}$$

where M is the multiplication factor:

$$\mathrm{M} = \frac{1}{1 - (\frac{\mathrm{V_{BC}}}{\mathrm{V_{BD}}})^{\mathrm{n}}} \tag{1.7}$$

where n is the fitting factor (between 3 to 6 for silicon [71]). Actual calculation of avalanche curent and multiplication factor for an SCR are quite complex [71], however, these above formulas give the simplified picture. At this stage, generally one of the transistors becomes dominant and determines the multiplication factor and so avalanche current depending on its current gain β and well resistance $\mathrm{R_{n\text{-}well}}$ or $\mathrm{R_{p\text{-}well}}$. In addition, an increase in one of the transistor current causes an enhancement at other transistor current with a self-feeding system. Therefore, at one stage we reach a voltage condition on $\mathrm{R_{n\text{-}well}}$ or $\mathrm{R_{p\text{-}well}}$ which is enough to bias base/emitter junction of pnp or npn, respectively. Then, once one of the transistors trigger, its collector current increases even more and we reach the enough voltage condition for triggering on the base/emitter junction of the other transistor rapidly and so this transistor also triggers. This is the point that we reach triggering voltage $\mathrm{V_{TR}}$ and triggering current $\mathrm{I_{TR}}$ on the SCR. At this stage both npn and pnp transistors trigger and previously reverse biased n-well/p-sub(p-well) junction breaks down and becomes forward biased. Therefore, the voltage on SCR catastrophically drops to a smaller value. This sudden decrease on the voltage is also called as *snap-back*. Silicon Controlled Rectifier (SCR); therefore, is used as an ESD protection element due to its this s-shaped characteristic. It drops the voltage on the protected device before reaching some unsafe voltage range by providing a discharge path.

After snap-back, since the voltage on the protected device is needed to be in the safe voltage range independently of the current value on the SCR, the slope of the IV curve has to be as vertical as possible. In other words, on-resistance value of SCR, $\mathrm{R_{on}}$, should be as small as possible. A large value of $\mathrm{R_{on}}$ causes also power dissipation and so heating which can be the reason of the failure of SCR itself at high currents such as thermal runaway. In a case like that the current and voltage levels that SCR is destroyed are called as $\mathrm{I_{t2}}$ and $\mathrm{V_{t2}}$, respectively. In this respect, in order to decrease on-resistance and to spread current to a larger width, multi-finger SCR structures where several SCRs are connected in parallel are designed.

Once the ESD stress on the protected circuit is over, SCR is expected to turn back to its idle state. However, as mentioned above, with the start of avalanche process, transistors go into a self-feeding (self-sustaining) system i.e. npn keeps pnp active and pnp keeps npn active. This self-sustaining current flow continues even after the avalanche process and the activating event are stopped. Thus, this results in reaching a holding current value I_{HOLD} smaller than I_{TR} during turn off. In other words, total current gain of transistors ($\beta_{npn} \cdot \beta_{pnp}$) stays still larger than one until reaching I_{HOLD} during turn off. Holding current I_{HOLD} and its corresponding voltage value V_{HOLD} is the last active point that we have SCR action. During design of an SCR, holding voltage V_{HOLD} should be designed to be higher than the supply voltage [25, 72–77]. Otherwise, supply pins become short circuited due to low on-resistance of SCR and so an excessive amount of current flows through SCR even after ESD stress on the protected circuit is over. Eventually this leads to the burning of SCR and failure of the protected circuit.

During the design of an SCR according to needs of the protected circuit, several approaches are realized in the expense of some trade-offs in order to achieve the desired parameters for V_{TR}, I_{HOLD}, R_{on}, capacitance and leakage current. For instance, to decrease triggering voltage V_{TR} an external triggering circuit such as diode [18, 78] and grounded-gate NMOS (ggNMOS) [79, 80] is connected to p-substrate (p-sub) region. Therefore, current from this external triggering circuit initiates triggering instead of avalanche current I_{aval}. However, this external triggering circuit enhances the overall capacitance. Another method to reduce V_{TR} is adding trigger taps (TT) between p-well and n-well regions [7, 25]. A trigger tap is a narrow region of p-implant that expedites current injection. Adding trigger tap at several places also eliminates on-state spreading and helps SCR to trigger at several places simultaneously. However, adding TT contributes to the leakage current and overall capacitance. Hence, their numbers are needed to be minimized. Another alternative method to decrease V_{TR} can be a floating-base SCR structure [14, 15] like in Figure 1.9 (a). With this approach p-well is left floating due to removal of p+ doping at the ground side. $R_{\text{p-well}}$ is set as an open-circuit and so npn directly triggers at very low currents. For the triggering of SCR; therefore, we just need to wait for triggering of pnp. To lower capacitance and leakage current on the other hand, p-sub region can be less doped. Low doped p-sub spreads the depletion width. On-resistance R_{on}; however, increases in that case. Another method for decreasing capacitance can be SOI technology where SCR stays on a buried oxide (BOX) [25, 81–84].

Chapter 2

Multi-finger SCRs with Substrate Coupling

Simultaneous finger triggering has always become a long-standing goal of ESD engineers [19–23] while designing multi-finger SCR structures especially to reach robustness of the order of 30 kV [14, 15]. However, during measurements, it has been observed that the number of triggered fingers were changing depending on the applied current [25], rise time (RT) [25] and width (PW) [25] of the pulse while the position of first triggered finger and the preferred direction for sequential triggering were dependent on the structural parameters of the device [14, 15]. In this respect, we decided to understand and explain the mechanisms behind of these triggering observed in multi-finger SCR structures used for ESD protection. For this purpose, we implemented different the pulse and device parameters, and checked their effect on the triggering behavior. By understanding the triggering mechanisms, one can achieve simultaneous or sufficiently fast finger triggering in order to meet requirements for high robustness.

For our investigation, two different multi-finger SCR test structures with substrate coupling provided by Nexperia Hamburg are studied under a HBM-like TLP stress and a Surge-like half sinusoidal pulse both experimentally and by TCAD simulation. Experimental investigations are achieved with TLP and TIM techniques. TCAD simulations, on the other hand, are conducted with Sentaurus from Synopsys. The work in section 2.1 is a continuation of studies of Clément Fleury [25]. For instance, some TIM results in section 2.1 can be also found in [25].

2.1 Analysis with TLP stress

2.1.1 Device under study

In this section, we investigate the triggering behavior of a 16-finger floating-base SCR of discrete technology [6] by applying a transmission line pulse (TLP) stress. Figure

2.1 (a) and (b) show the studied SCR structure and its enlarged image for four fingers, respectively. All fingers stay on a lightly p-doped silicon-on-insulator (SOI) substrate [13] and there is no shallow trench isolation (STI) in between them; therefore, they all are coupled through the same p-substrate.

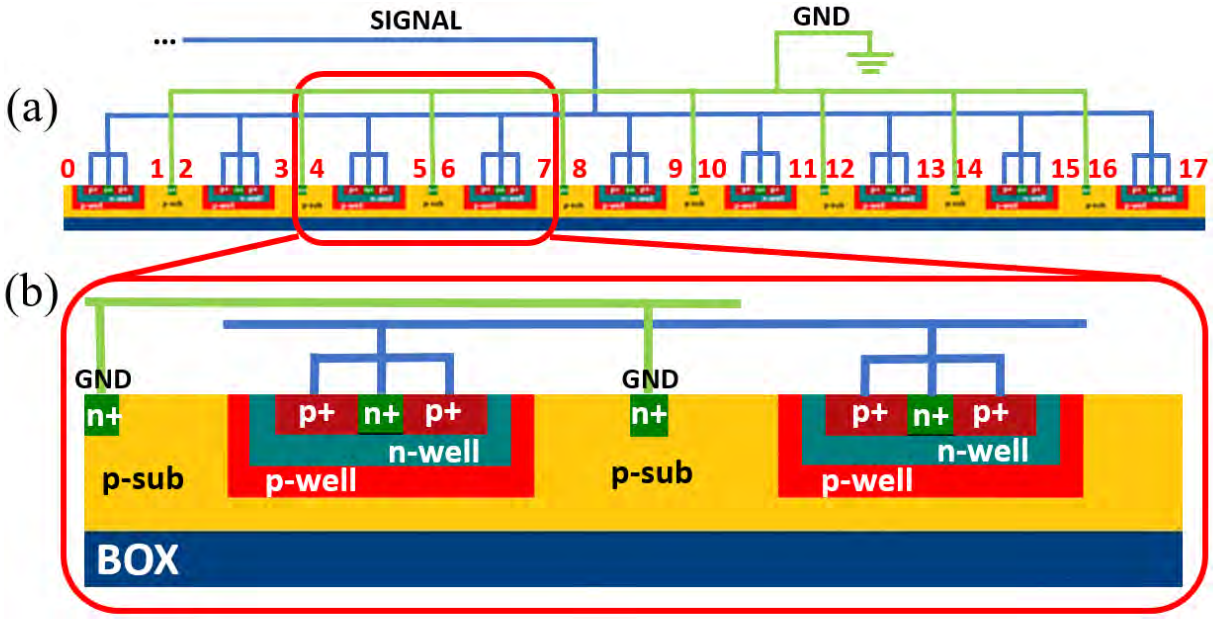

Figure 2.1: (a) Studied 16-finger floating-base SCR structure. (b) Zoomed image for four fingers.

The p+-emitter and n-well regions share the same contact metallization and the positive TLP stress is applied on them. The n+-emitter (GND) contacts of the npn transistors, on the other hand, are connected to ground. The n-well serves both as a base and a base resistor of the pnp transistor while the deep p-well serves both as a base of npn and a collector of pnp. The deep p-well and p-substrate are also left floating.

SCRs are labeled from ‘1’ to ‘16’, in other words from SCR1 to SCR16. The outer fingers on the left and right sides, which are denoted as ‘0’ and ‘17’, respectively, are inactive in the on-state. However, they determine the initial triggering position to be at fingers 1 and 16 at long RT values [14] as will be described later.

2.1.2 Experimental results

We start our analysis by investigating the triggering behavior under short (RT = 300 ps) and long (RT = 10 ns) rise-time values.

2.1.2.1 Simultaneous finger trigering for rise time of 300 ps

Figure 2.2 (a) represents the typical TLP IV curve for RT = 300 ps and PW = 100 ns. As it can be observed, for current values $I < 0.5$ A, a jump is observed in the IV curve.

That means there exists a higher differential resistance for I < 0.5 A. For currents I > 0.5 A, however, there is no jump. In other words, it exhibits a single differential resistance for currents I > 0.5 A. So if we look at the voltage waveform for a current value I > 0.5 A such as 1.75 A, we observe a flat waveform as shown in Figure 2.3 (a). The small ripple at t = 30 ns is a setup artefact due to reflections. At that point, based on these two analysis, it can be concluded that:

a) whether all fingers trigger for I > 0.5 A at the beginning of the pulse and so no non-triggered finger left. The resulted differential resistance, therefore, is the parallel resistance of all triggered 16-fingers or

b) some fingers are triggered at very pulse beginning but somehow no new fingers trigger during the 100ns pulse duration. The resulted differential resistance, thus, is the parallel resistance of the just triggered fingers.

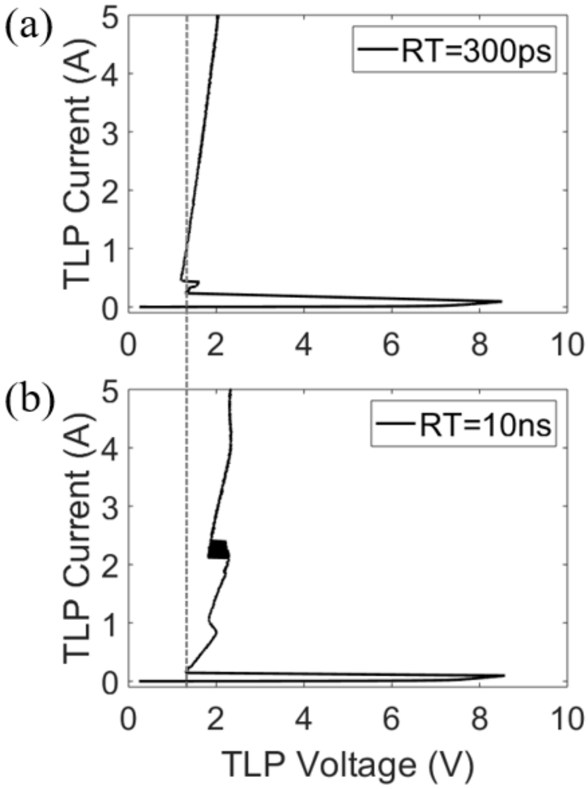

Figure 2.2: 100ns TLP IV curve for (a) RT=300ps and (b) RT=10ns. The averaging window is 75-90ns.

In order to understand what is really going on there in terms of finger triggering, a TIM analysis is needed. Figure 2.4 shows the TIM scan for I = 1.5 A at the pulse beginning. From the scan it is observed that there is a negative phase shift in the p-sub below the n+-GND contacts of each finger. Since the negative phase shift is caused by free carrier injection, this indicates the simultaneous triggering at least for I > 0.5 A.

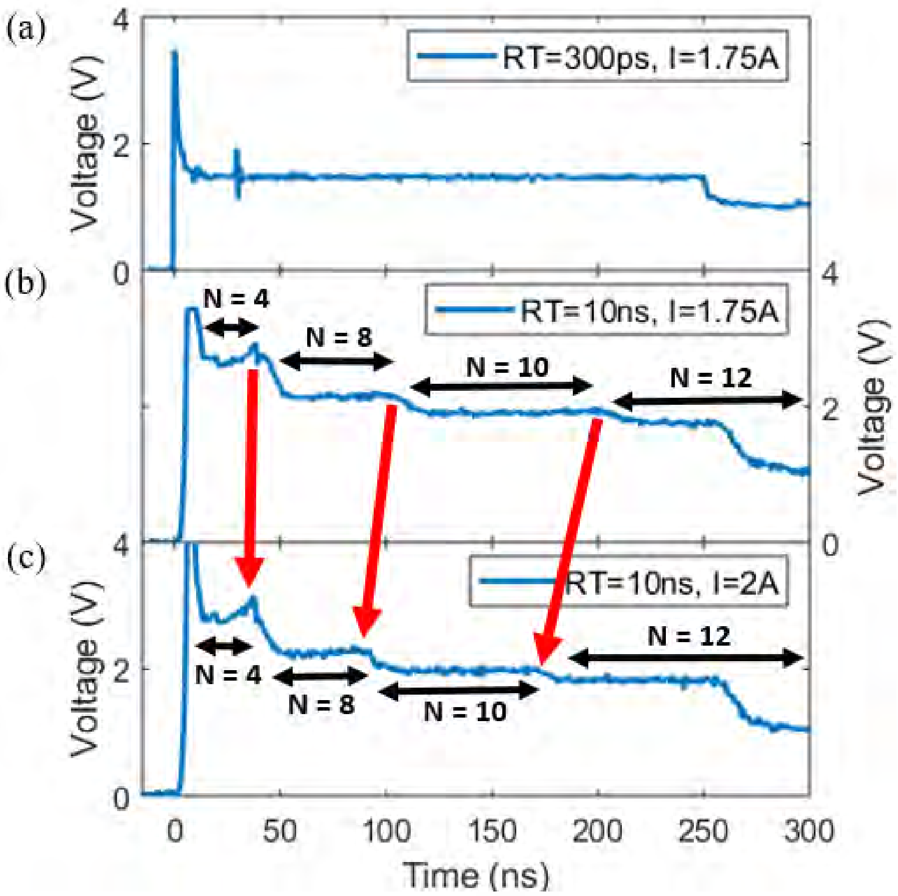

Figure 2.3: Typical voltage waveforms for: (a) RT = 300 ps and I = 1.75 A, (b) RT = 10 ns and I = 1.75 A and (c) RT = 10 ns and I = 2 A. The number of triggered fingers N, extracted from TIM measurements, is indicated. The small ripple at t = 30 ns in (a) is a setup artefact due to reflections.

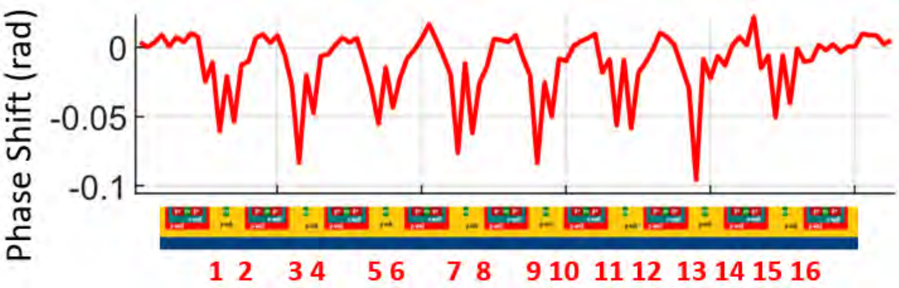

Figure 2.4: TIM scan for RT = 300 ps and I = 1.5 A. The time instant is 20 ns [25].

2.1.2.2 Sequential finger trigering (SFT) for rise time of 10 ns

Figure 2.2 (b) shows the TLP IV curve for RT = 10 ns and PW = 100 ns. As it can be observed, it has several regions with different differential resistances. Also, if we compare Figure 2.2 (a) and (b), it is seen that for I > 0.5 A, the holding voltage for the IV with

RT = 10 ns is higher than that for the IV with RT = 300 ps. Then, if compare the voltage waveforms for RT = 300 ps (Figure 2.3 (a)) and RT = 10 ns (Figure 2.3 (b)) at the same current level (I = 1.75 A), we again see this holding voltage increase. For RT = 10 ns, after triggering at V_{TR} = 8.4 V (see Table 2.1), voltage on the SCR exhibits downward steps instead of a flat waveform like in the case of RT = 300 ps. Based on these results it can be concluded that for RT = 10 ns, fingers trigger subsequently, not together. Therefore, in order to understand the triggering behavior, a TIM scan is needed.

In addition to that Figure 2.3 (c) shows the voltage waveform for current I = 2 A under the condition of RT = 10 ns. As indicated by the red arrows, the time instants of the voltage drops in Figure 2.3 (b) shift to shorter time values. Hence, based on this analysis it can be stated that finger triggering is accelerated by increasing the applied current. However, still a TIM scan is needed to check whether triggering sequence changes or stays the same after applying a higher current.

	V_{TR} (V)	**J_{TR} (mA/µm)**
Exp.	8.4	0.25
Simul.	12.3	0.068

Table 2.1: V_{TR} and J_{TR} values in experiment and simulation

Figure 2.5 (a) and (b) show the TIM scans across the fingers at some selected time instants (indicated on right sides of the figures) under the condition of RT = 10 ns for currents 2 A and 4 A, respectively . As it can be observed, in both scans fingers trigger successively. Thus, this reveal that the voltage drops observed for RT = 10ns are related to sequential triggering of next fingers. If we investigate the triggering sequence for both applied currents, we observe that the outer fingers 1 and 16 triggers first and it is almost instantaneously followed by the triggering of neighboring (inner) fingers 2 and 15 (see panels at t = 11 ns in Figure 2.5 (a) and at t = 15 ns in Figure 2.5 (b)). Since these four fingers trigger during the rising edge of the pulse, there is a very small time difference between their triggering. Then, the inner fingers 3 and 14 trigger subsequently (see panels at t = 57 ns in Figure 2.5 (a) and at t = 35 ns in Figure 2.5 (b)), followed by fingers 4, 13 and so on. As it is indicated at panel t = 213 ns of Figure 2.5 (a), only 12 fingers trigger out of 16 fingers for I = 2 A during the applied pulse of PW = 250 ns. Triggering sequence ends at fingers 6 and 11. If we look at Figure 2.5 (b), on the other hand, we observe that all of the 16 fingers trigger already at t = 151 ns, which is quite earlier than the end of the pulse. In addition, with the increase of current to I = 4 A, fingers 3, 5 and 14, 12 trigger earlier compared to the case for I = 2 A. This is also consisted with the time-shift of the voltage jumps observed in voltage waveforms in Figure 2.3 (b) and (c).

At that point,to make the triggering mechanism easier to understand and find some relation between finger triggering, we made some definitions and defined a so-called trigger delay $\tau_{i,i+1}$ between the triggering of i-th and (i+1)th fingers where i = 1 - 8. This trigger

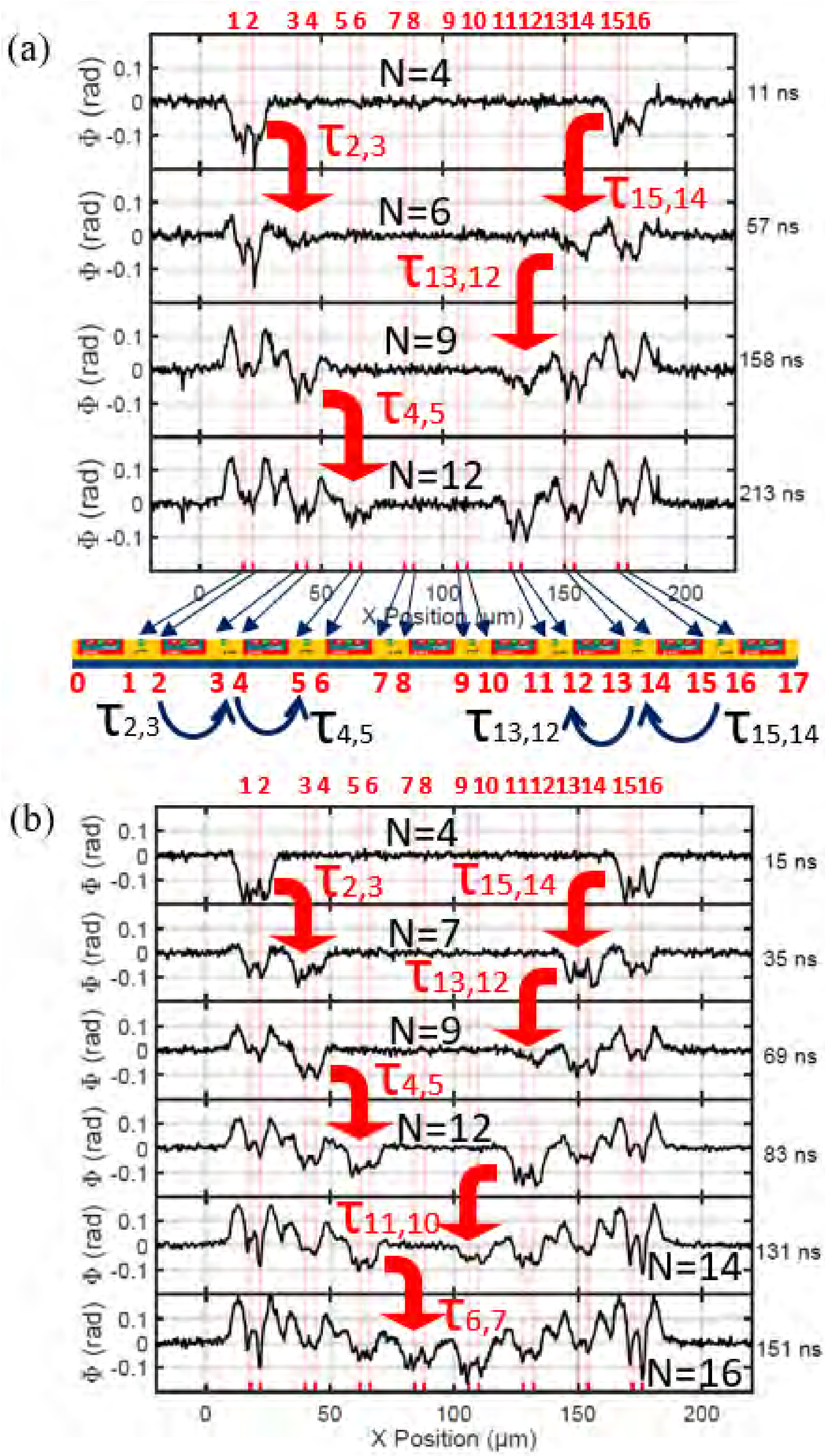

Figure 2.5: TIM scan for RT=10ns and (a) I=2A and (b) I=4A for selected time instants during a 250ns long TLP pulse. The positive value of phase shift at longer times is due to temperature increase caused by the self-heating effect [25].

delays; therefore, are for the propagation of triggering activity from the left to right. For the propagation of the triggering activity from the right to left, on the other hand, we defined an analogous notation $\tau_{\mathrm{j+1,j}}$ where j = 16 - 9. Based on these notation, we made some observations:

1) There exists a short trigger delay τ_{short} in the 3-5 ns range between the fingers sharing the same GND contact, so $\tau_{\mathrm{short}} = \tau_{\mathrm{i,i+1}}$ for i = 1, 3, 5, 7 and $\tau_{\mathrm{short}} = \tau_{\mathrm{j+1,j}}$ for j = 15, 13, 11, 9.

2) There exists a long trigger delay $\tau_{\mathrm{long}} > 15$ ns between the triggering of fingers sharing the same n-well contact, i.e. $\tau_{\mathrm{long}} = \tau_{\mathrm{i,i+1}}$ for i = 2, 4, 6 and $\tau_{\mathrm{long}} = \tau_{\mathrm{j+1,j}}$ for j = 14, 12, 10. In figure 2.5 (a) and (b) some of these time delays are schematically indicated in between the time panels or on the device schematics.

3) The total number of triggered fingers N increases during the applied pulse. This number is indicated in black in Figure 2.5 (a) and (b) for each time panel. For both currents of I = 2 A and I = 4 A in Figure 2.5, the smallest N is 4 because it was not possible to differentiate the trigger delay between the fingers 1 and 2, and 16 and 15 at the pulse beginning. These four fingers trigger during 10 ns pulse rising edge.

4) Triggering of each new finger pair which shares the same GND contact corresponds a drop in voltage waveform V(t). Since the TIM experiment in Figure 2.5 (a) and the voltage waveform in Figure 2.3 (c) are for the same current of I = 2 A, the number of triggered fingers N for each voltage plateau between the steps can be established as shown in Figure 2.3 (b) and (c). The reason of voltage drops on V(t) is the finite differential resistance of the SCR in the on-state. With the triggering of more fingers, the less amount of current flows through each single finger. Hence, voltage drop on the device gets smaller.

Based on these above notation, the extracted values of τ_{long} and τ_{short} from TIM measurements for I = 2 A and I = 4 A are plotted in Figure 2.6 (a) and (d). The horizontal axis represents the average one-dimensional current density, J, before the finger triggering and it is defined as

$$\mathrm{J} = \frac{\mathrm{I}}{\mathrm{N} \cdot \mathrm{W}} \tag{2.1}$$

where N is the number of triggered fingers and W is the device width. If we look at Figure 2.6 (a), it is observed that instead of showing a symmetric behavior, some values of current densities are slightly shifted from certain defined positions on the bottom axis. This is because the trigger delays for the triggering from left to the middle and from right to the middle may slightly differ. In other words, triggering from left to middle and right to middle may not happen symmetrically. For instance, in between the triggering of two neighboring fingers $\mathrm{SCR_i}$ and $\mathrm{SCR_{i+1}}$, another finger at the right part of the device may also trigger. In this case, the current density gets two separate values during one triggering: a higher value $\mathrm{J_H}$ and a lower value $\mathrm{J_L}$. Therefore, in a case like that J is defined as

$$J = \frac{J_H \cdot \Delta t_H + J_L \cdot \Delta t_L}{\Delta t_H + \Delta t_L} \tag{2.2}$$

where Δt_H and Δt_L are time intervals spent during high and low current densities, respectively.

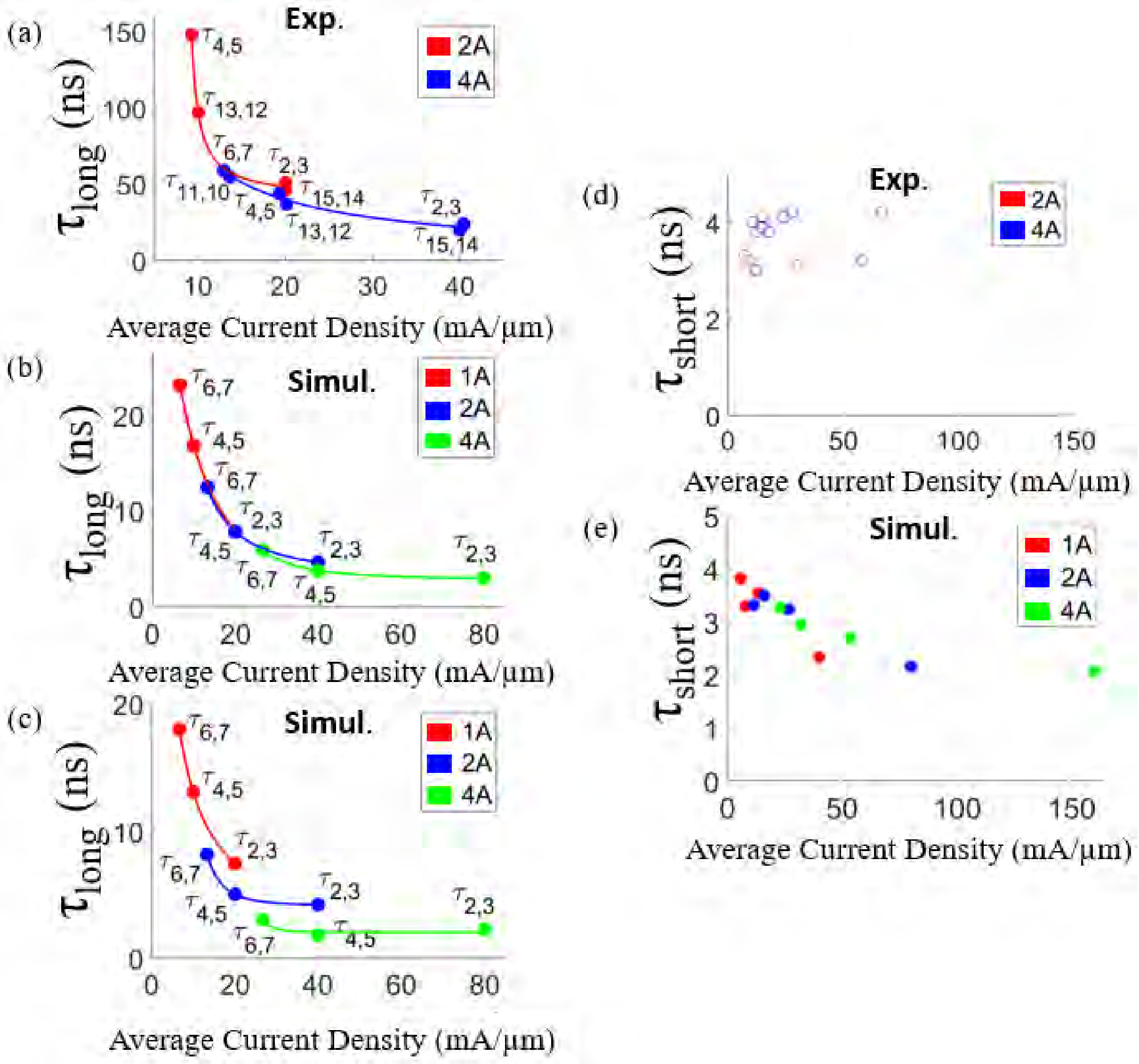

Figure 2.6: Experimental (a,d) and simulated (b,c,e) long (a-c) and short (d,e) time delays between the triggering of fingers as a function of average current density J. R is 0 Ω in (b) and (e) and R = 1 Ω in (c). $\tau_{i,i+1}$ labels in (d) and (e) are omitted due to interwoven values.

As it can be seen in Figure 2.6 (a), data for I = 2 A and I = 4 A overlap and τ_{long} values decreases with average current density J. Thus, it can be concluded that τ_{long} is mainly determined by average current density J. On the other hand, if we look at Figure 2.6 (d), a trend like that is not seen for τ_{short} values and this may be due to influence of noise. Extracted τ_{short} values are at the 3 ns limit of experimental accuracy (see TIM technique section in chapter 1).

Since we understood how fingers trigger sequentially under different applied currents by using TIM and since we know how these triggering are related to successive voltage drops on voltage waveform V(t), we can extract the voltage values for different number of triggered fingers, N, as a function of current and create IV plots. With this plotting IV branch for particular N can be created. Figure 2.7 (a) shows this IV curve for experimental data. For each IV data point, the voltage values represents the average voltage value of each flat region in between the steps of voltage transient which can be observed in Figure 2.3 (b) and (c). As it can be seen, the duration of these flat regions are different. Hence, each IV point is obtained for a different averaging time window. In this respect, to be able to follow these averaging time windows, the average extraction time of each averaging time window is color-coded and inserted in the figure.

The IV branches in Figure 2.7 (a) starts from N=4 as explained above and ends at N=16. Figure 2.7 (c) shows the device model used for obtaining dashed line fittings for IV branches in Figure 2.7 (a). At high currents, some of SFT occurs during the pulse rising edge ($0 < t < 10$ ns). Therefore, the voltage extraction within this part does not show the precise average voltage value after triggering. For this reason, the voltage data for this part was disregarded in Figure 2.7 (a). Only data for $t > 10$ ns was given. That is why, there are reduced number of IV points at high currents for branches with low N. Besides that, as we know, for lower currents evaluation time is longer for a fixed N. So in Figure 2.7 (a) in each IV branch, the average extraction time shifts to longer time values as current decreases. Also, as the time progresses, due to the sequential triggering of more fingers the voltage jumps from the IV branches with lower N to higher N for a nearly fixed current. The round arrows at $I = 1$ A in Figure 2.7 (a) indicate example of such jumps. Compared to standard TLP IV curve like in Figure 2.2 (b), IV curve like in Figure 2.7 (a) provides far more detailed data for SFT phenomenon. This is because in standard TLP IV due to averaging over the same time window, the time-dependent data structure is lost.

2.1.3 TCAD simulation approach

For simulation purposes, an 8-finger 2D device structure was created by using Synopsys Sentaurus TCAD as shown in Figure 2.8. The half of the experimental structure is taken because, as discussed in Figure 2.5 (a) and (b), in the measurements fingers trigger from left and right sides towards the middle. Therefore, simulating half of the structure is enough to represent the device behaviour by reducing the simulation time without loosing the accuracy. At that point it is better to remark that due to this size difference between measured and simulated device structures, the experimental and simulation results are needed to be compared at the same current density J and not at the same total current I.

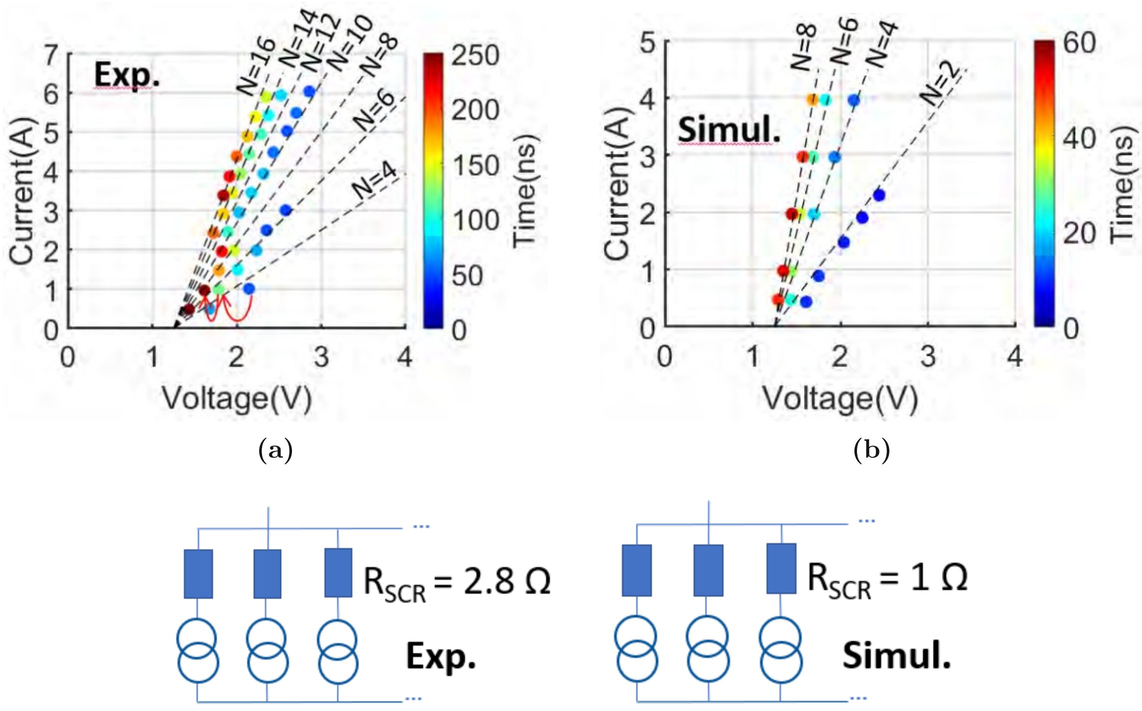

(a) (b)

(c) (d)

Figure 2.7: IV data representation for current/voltage values extracted from each flat part of the voltage transient in between the triggering of finger pairs with common GND, where RT = 10 ns: (a) experiments, (b) simulation. (c) and (d) shows the used device model for obtaining dashed line fitings for IV branches in (a) and (b), respectively. The times of extraction is color-coded and the number of triggered fingers N are indicated. The voltage jumps for I = 1 A are indicated by round arrows.

Since the simualted structure is half of the experimental structure, for the same applied current I and the same number of triggered fingers N, the current density in the simulation is two times higher than that in experiments.

The typical half-pitch distance between the fingers is 5.5 µm. Therefore, according to the thermal diffusion length, defined as [85]

$$\mathrm{L_{th}} = 3\mu\mathrm{m} \cdot \sqrt{\frac{\mathrm{t}}{100\mathrm{ns}}} \tag{2.3}$$

where t is the time difference between the triggering of fingers, we suppose that the self-heating effect has negligible impact on τ_{long}, at least for $\tau_{\mathrm{long}} < 300$ ns as in our case. In other words, the lateral distance between the neighboring fingers is larger than the thermal diffusion length determined by the trigger delay. In this respect, we conduct an isothermal drift-diffusion simulation model instead of a thermodynamic model and get rid of time consumption due to solving of complex thermal equations. Besides that at the edges of simulation region Neumann boundary conditions are applied.

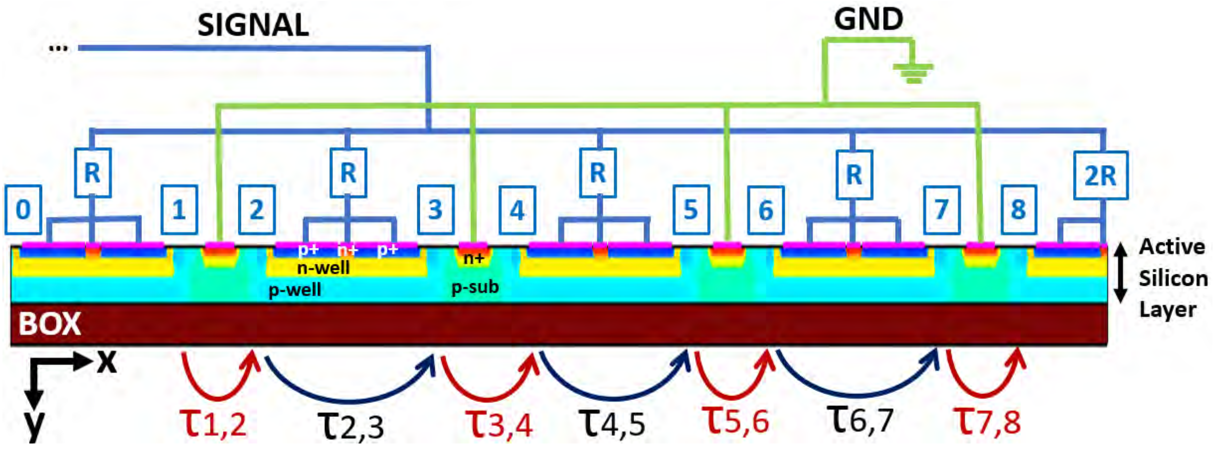

Figure 2.8: Simulation setup with separate contacts for each SCR current component. Time delays are indicated.

In order to make individual analysis of current components on each SCR finger, on top of p+-emitters, n+ region of n-wells and n+-GND regions separate contacts are implemented. The currents through these contacts are called p-emitter, n-well and GND currents. Moreover, to see the effect of contact resistances, simulations are conducted with and without a contact resistance of R = 1 Ω connected to each finger. We did not calibrate the simulation in detail in terms of doping concentration and this lead to differences in experimental and simulated V_{TR} and J_{TR} values (see Table 2.1). However, it allowed us to draw qualitative conclusions.

2.1.4 Simulation results

Before explaining the triggering mechanism under different rise time conditions, it is better here to explain the general condition for triggering in order to help the reader to understand the further subjects easier. In general, an impact ionization occurs at the reverse biased n-well/deep p-well junctions of all fingers prior to triggering of the SCR (what we mean by SCR is the all SCR fingers in the case of simultaneous finger triggering and first triggered SCR finger in the case of sequential finger triggering). Then, with the increase of device voltage, the p-sub to n+-GND junction becomes forward biased and leads to the open base breakdown [86] of the npn transistor. Since now npn becomes active, The collector current, $I_{c,npn}$, of the npn flows through the n-well with a resistance of $R_{n\text{-well}}$. The situation can depicted in a lumped element representation of SCR as shown inside of the dashed box in Figure 2.9. When the potential drop on $R_{n\text{-well}}$ becomes sufficiently high to bias the emitter/base junction of pnp (p+/n-well junction of SCR finger), the p-emitter current of the pnp starts to inject and so the device is driven into self-sustaining SCR action. This indicates the moment of triggering of the SCR [87].

Now, we will investigate the effect of short (RT = 300 ps) and long (RT = 10 ns) rise

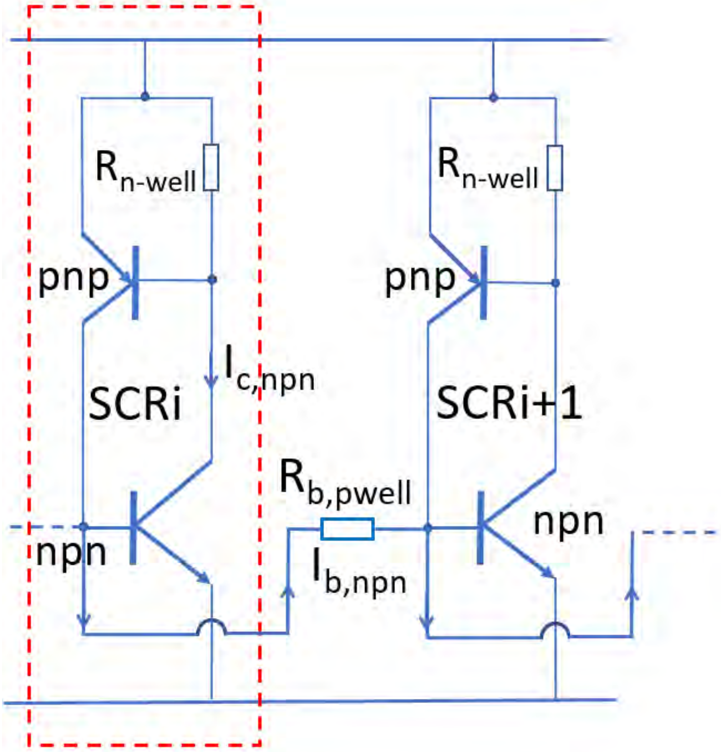

Figure 2.9: Lumped element representation of two SCRs with common n-well contact. The hole base current $I_{b,npn}$ from SCRi to SCRi+1 is indicated (i=2,4,6).

time values on triggering behaviour of simulation structure.

2.1.4.1 Simultaneous finger triggering for rise time of 300 ps

2.1.4.1.1 I(t) and V(t) waveforms The simulated device voltage, p-emitter and n-well currents of each finger during the first nanosecond of a TLP pulse with I = 1 A and RT = 300 ps is shown in Figure 2.10 (a). In terms of current density it represents 2 times higher current density compared to the measured 16-finger device under the same current condition. As it can be observed, n-well currents are negligible and the p-emitter currents are the dominant components of the total current. In addition, the p-emitter currents start to rise at a voltage near V_{TR}, well before the time where the voltage overshoot peak V_{peak} = 16 V happens. Since the rise of p-emitter current represents the moment of finger triggering, it can be stated that all of the 8-fingers trigger before V_{peak} occurs. Figure 2.10 (b), on the other hand, shows the very beginning of the pulse where p-emitter currents rise almost simultaneously at about t = 100 ps.

Besides that under RT = 300 ps condition, if we make simulations above 0.5 A, all fingers trigger simultaneously whereas below 0.5 A, only a few fingers. Therefore, although there is a factor of 2 difference in terms of current densities for the onset of homogeneous triggering between simulations [0.5A/(8W)] and experiments [0.5A/(16W)],

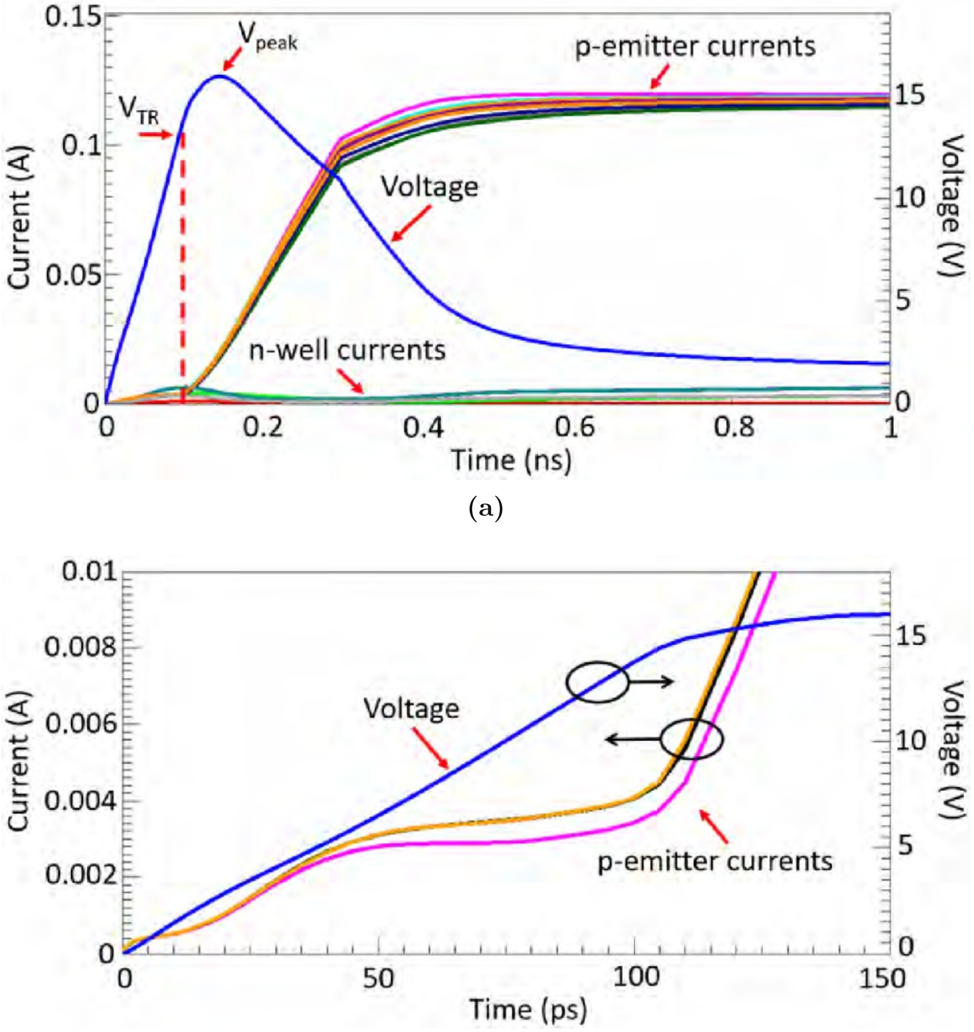

(a)

(b)

Figure 2.10: (a) The simulated voltage, p-emitter and n-well current waveforms for I = 1 A, RT = 300 ps and R = 0 Ω. (b) The zoomed region during the pulse rising edge to show the very beginning of the pulse.

this is consistent with the experiments (see Figure 2.2 (a)) and it can attributed to differences in triggering parameters (see Table 2.1).

2.1.4.1.2 Simultaneous finger triggering mechanism Since the voltage overshoot V_{peak} = 16 V is well above the V_{TR}, we think that the reason of simultaneous finger triggering in the multi-finger device for RT = 300 ps is the voltage overshoot. After the activation of p-emitter currents at a voltage near V_{TR}, holes from p-emitters injects into the p-sub and the conductivity in p-sub starts to rise. However, during the short rise time (RT = 300 ps), the conductivity of p-sub does not become enough to cause triggering and so a voltage drop and the voltage on the device; therefore, still rises to accommodate the imposed current. The voltage overshoot beyond V_{TR} during a short pulse rising edge is known to be due to the delayed conductivity modulation of the low-doped p-sub [13, 88]. With the increase of the voltage, impact ionization happening in the n-well/deep p-well junctions of each finger also increases and provides more base currents for the npn and pnp transistors. Finally, at some voltage value (V_{peak}), the conductivity in p-sub becomes enough for triggering and so the voltage on the device starts to drop. In other words, due to delayed conductivity, voltage on the all fingers increases. Hence, this amplifies the impact ionization at all fingers and so all fingers trigger together at nearly the same moment.

Figure 2.11 (a) shows the Conduction Band Energy (eV) value around finger 2 through A-A' line at $V = V_{TR}$ and $V = V_{peak}$ moments of Figure 2.11. As it can be observed, starting from the moment of rise of p-emitter current, the potential drop related to the voltage overshoot over V_{TR} (i.e. V_{peak}-V_{TR}) appears in the p-sub along the n+-GND to deep p-well direction. This is also consistent with the analytical modeling of the pin diodes [8, 89].

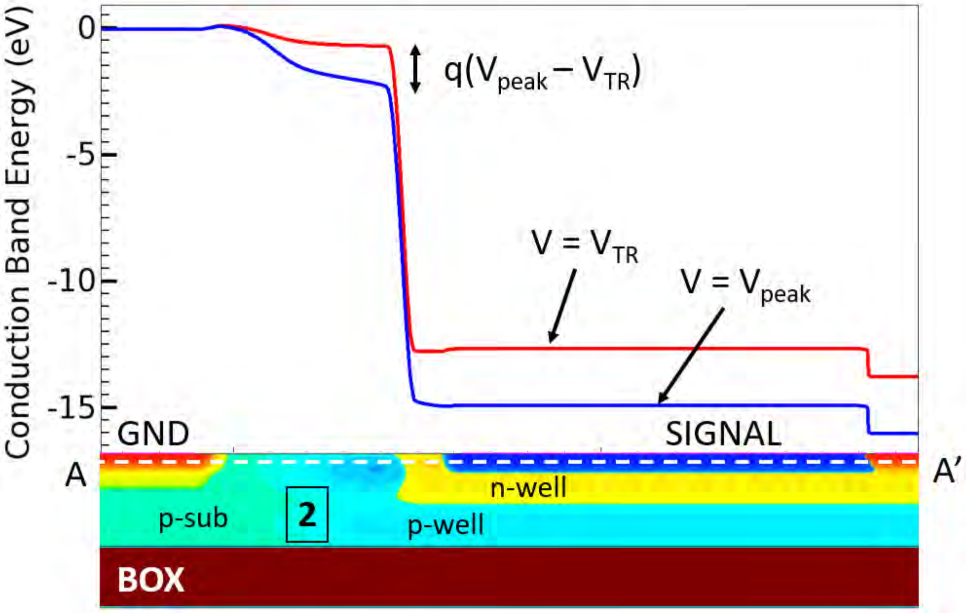

Figure 2.11: Conduction Band Energy (eV) value around finger 2 through A-A' line at $V = V_{TR}$ and $V = V_{peak}$ moments of Figure 2.10 (a)

With this result it can be said that in our case the reason of simultaneous finger triggering is not the usually-considered displacement current $C \cdot \frac{dV}{dt}$ (C being the base collector capacitance) [19] but the voltage overshoot. The $C \cdot \frac{dV}{dt}$ effect reduces the trigger voltage. However, in our case the trigger voltage increases due to delayed conductivity modulation.

2.1.4.2 Sequential finger trigering for rise time of 10 ns

2.1.4.2.1 I(t) and V(t) waveforms and trigger delay extraction The simulated voltage and current components of each SCR for I = 1 A and RT = 10 ns is shown in Figure 2.12 (a) and (b), respectively. R (see Figure 2.8) is set to zero in order to eliminate the influence of an extra voltage drop on it and so to see the net effect of the SCR behavior on the triggering. Figure 2.12 (a) contains the full and the enlarged scale data of voltage waveform V(t). The enlarged voltage data is obtained by zooming inside of the dashed rectangle in Figure 2.12 (a). Figure 2.12 (c), on the other hand, shows the enlarged current waveforms from Figure 2.12 (b) by zooming inside of the dashed rectangle. The dotted lines in Figure 2.12 (b) and (c) show which particular current component corresponds to which contact.

As discussed previously, the rapid rise of the p-emitter currents, which dominate the n-well currents in the on-state, in Figure 2.12 (b) and (c) indicates the onset of SCR action. In this respect, it can be observed that SCR1 triggers first at $V_{TR} \sim 12.3$ V and then the inner fingers trigger consecutively. The reason for SCR1 to trigger first is the assistance of impact ionization happening in the neighbor SCR0 in the trigger process but it will be discussed in detail later in the sequential finger triggering mechanism part. Compared to the case of RT = 300 ps, the inner fingers are activated near the holding voltage, as observed also in measurements with RT = 10 ns (see Figure 2.3 (b) and (c)), without impact ionization. By following the triggering of SCR1, SCR2 triggers after a short trigger delay $\tau_{\text{short}} = \tau_{1,2}$ and then SCR3 after a long trigger delay $\tau_{\text{long}} = \tau_{2,3}$. Likewise, all fingers trigger alternately until SCR8 triggers. Time delay between the triggering of fingers are indicated in Figure 2.12 (c) (see also Figure 2.8). Each time when a new finger triggers, the following happens:

1) The current density in the triggered fingers tends to be equalized. In addition, it decreases in already triggered fingers and increases in the newly triggered finger (see Figure 2.12 (b)).

2) A voltage drop is observed in the voltage waveform V(t) as can be seen in the enlarged waveform in Figure 2.12 (a). This voltage drop occurs small and high depending on whether there is a short (τ_{short}) and long (τ_{long}) delay period, respectively. In experiments (see Figure 2.3 (b) and (c)), due to resolution of TIM setup the small voltage drop related to triggering of a finger pair with common GND cannot be distinguished; however, the high voltage drop related to triggering of a finger pair which shares the same n-well contact can be resolved.

Like we did in the analysis of experimental data, τ_{long} and τ_{short} values from simulations are extracted for R = 0 Ω (see Figure 2.8) and plotted as a function of current density J at three different currents in Figure 2.6 (b) and (e), respectively. As it can be observed in Figure 2.6 (b), τ_{long} decreases strongly with increasing J and τ_{long} data for the three different currents overlap perfectly. This shows us that our simulation results are

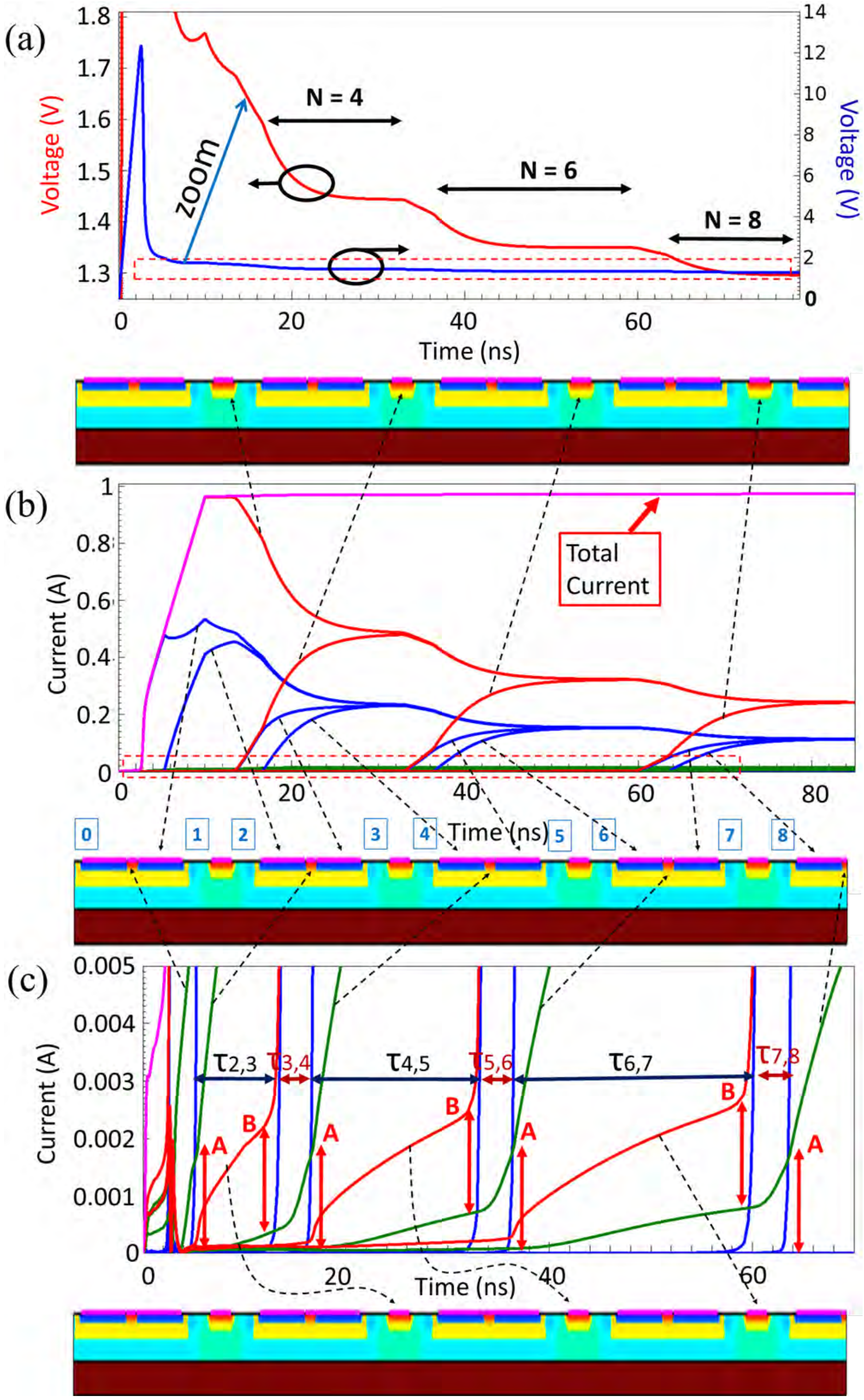

Figure 2.12: Simulated voltage (a) and current (b) components under the conditions of I = 1 A, RT = 10 ns and R = 0 Ω. (c) Zoomed current waveforms. Blue, green and red lines indicate the p-emitter, n-well and GND currents, respectively. The dotted arrows relate these currents to corresponding contacts. The red curve in (a) is the zoom of the dashed rectangle. Figure (c) is the zoom of the dashed rectangle in (b).

in a qualitative agreement with the measurements in Figure 2.6 (a). This is also the confirmation for our argument that τ_{long} is mostly determined by the average current density J. At that point it is also worth to point out that one can observe higher values of τ_{long} in the measurements compared to simulations at the same J by comparing Figure 2.6 (a) and (b). This discrepancy can be attributed to the higher triggering current density in experiments compared to simulations (see Table 2.1). To reach a higher current density on the next triggering finger, a longer time is needed to wait in experiments. We also want to remark that there is a slight decrease in τ_{short} values with J in simulations (see Figure 2.6 (e)). This was not distinguished in the experiments (Figure 2.6 (d)) due to resolution of the TIM setup.

Using the same procedure in measurements that we used to create Figure 2.7 (a), IV data is extracted for currents from 0.5 A to 4 A and plotted as in Figure 2.7 (b). As it can be seen, there exists a similar pattern to measurements when we consider the evaluation of finger pairs with common GND together. A significant difference between Figure 2.7 (a) and (b) is that the smallest N in simulations is 2 because the half of the structure is simulated. The on-resistance values of SCRs in experiments and simulations are also different as shown in Figure 2.7 (c) and (d).

2.1.4.2.2 Sequential finger triggering mechanism We will start our discussion with the investigation of why SCR1 triggers first. In the simulations it is observed that the impact ionization occurs also in the inactive finger SCR0 at $V = V_{\text{TR}}$ along its high-doped deep p-well/n-well junction. Figure 2.13 (a) and (b) shows the hole current density just before (t = 2 ns) and at the triggering of SCR1 (t = 2.34 ns), respectively. As it can be seen, the generated holes due to this impact ionization moves through the deep p-well below SCR0 and SCR1 (see the dashed arrow in Figure 2.13 (a)) towards the active GND contact of SCR1. This hole current; therefore, serves as the base current, $I_{\text{b,npn}}$, for the npn of SCR1 and biases its base emitter junction (see Figure 2.13 (b)). Since this extra hole current from SCR0 helps the triggering of SCR1, SCR1 triggers first. The $I_{\text{b,npn}}$ moving through the deep p-well resistance $R_{\text{b,p-well}}$ can be indicated in a lumped element scheme as in Figure 2.9. According to the lumped element representation in Figure 2.9, the left and right SCRs indicate SCR0 and SCR1, respectively. The resistance $R_{\text{b,p-well}}$, on the other hand, couples these two SCRs.

Since we understood how SCR1 trigger first, we will now investigate how the inner fingers trigger. As we discussed previously, pnp of an SCR is activated once we have enough voltage difference on the $R_{\text{n-well}}$ resistance (see Figure 2.9). In this respect, at the fast rise moment of the p-emitter current, the electron current in the n-well can considered as the representative of the local trigger current for an SCR finger. In our multi-finger simulation structure, since the inner fingers trigger sequentially, the n-well currents at the n-well contacts of the even fingers (i = 2, 4, 6, 8) contain contribution from only that SCR and so it can be directly extracted (see Figure 2.8 and Figure 2.12 (b) and (c)).

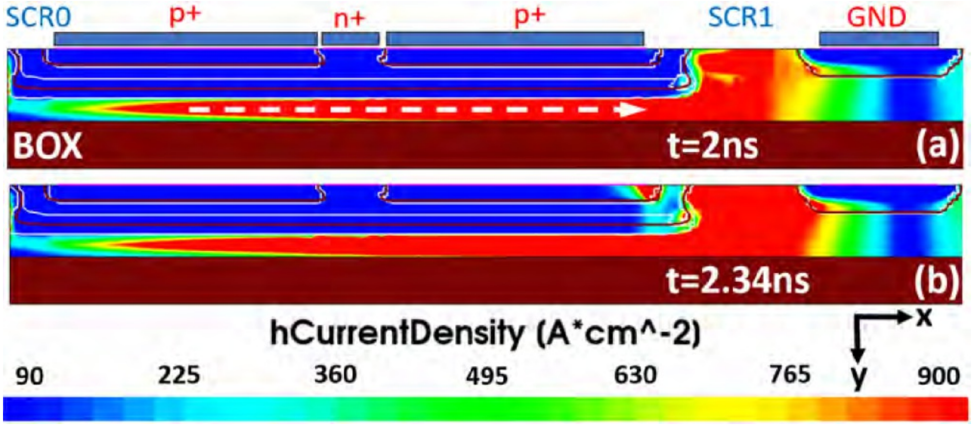

Figure 2.13: Simulated hole current density (a) just before and (b) at the triggering of SCR1. I = 1 A, RT = 10 ns and R = 0 Ω.

These extracted n-well currents at the triggering of even fingers are denoted by arrows A in Figure 2.12 (c). In the case of odd fingers (j = 1, 3, 5, 7); however, we cannot rely on the n-well currents on the n-well contact of these fingers as the local trigger current because the n-well currents of the odd SCRs contain contributions from two SCRs. The previously triggered even finger which shares the same n-well contact with the odd finger also contributes to the current at the n-well contact of the odd SCR. But we know that the n-well currents of odd SCRs goes to their GND contacts and constitutes their GND currents. So we can benefit from these GND currents to find the local triggering n-well currents of the odd fingers. The GND currents contain the n-well current of the j-th SCR (odd finger) in addition to n-well current of non-triggered j+1-th SCR (even finger). Hence, the n-well current of odd fingers can be extracted by subtracting the n-well current of the j+1-th SCR from the GND current of the j-th SCR. These currents are denoted with arrows B in Figure 2.12 (c). It is remarkable that the current differences indicated by arrows A and B are the same. Thus, this indicates that each inner finger triggers at the same local triggering current of about 1.8 mA.

Now we will go into detail and investigate the physical origin of the inter-finger coupling between inner fingers, which appears at voltages well below V_{TR}, where there is no impact ionization. We will also discuss processes which determines the long and short trigger delays. For that purpose, we will consider the triggering of SCR5 and SCR6 after triggering of SCR4 because they are far from the right reflecting boundary in addition to SCR1. Hence, with this selection we eliminate their possible influence. Figure 2.14 shows the simplified schematics for our consideration. With the triggering of SCR4, holes are injected from the p-emitter and forms the dominant lateral SCR path which is shown with the blue arrow Figure 2.14 (a). The supporting flow of electrons via n-well, on the other hand, is indicated with the red arrow. With these electrons, the region below the n-well of SCR4 is filled with an electron-hole plasma as shown with the dashed region

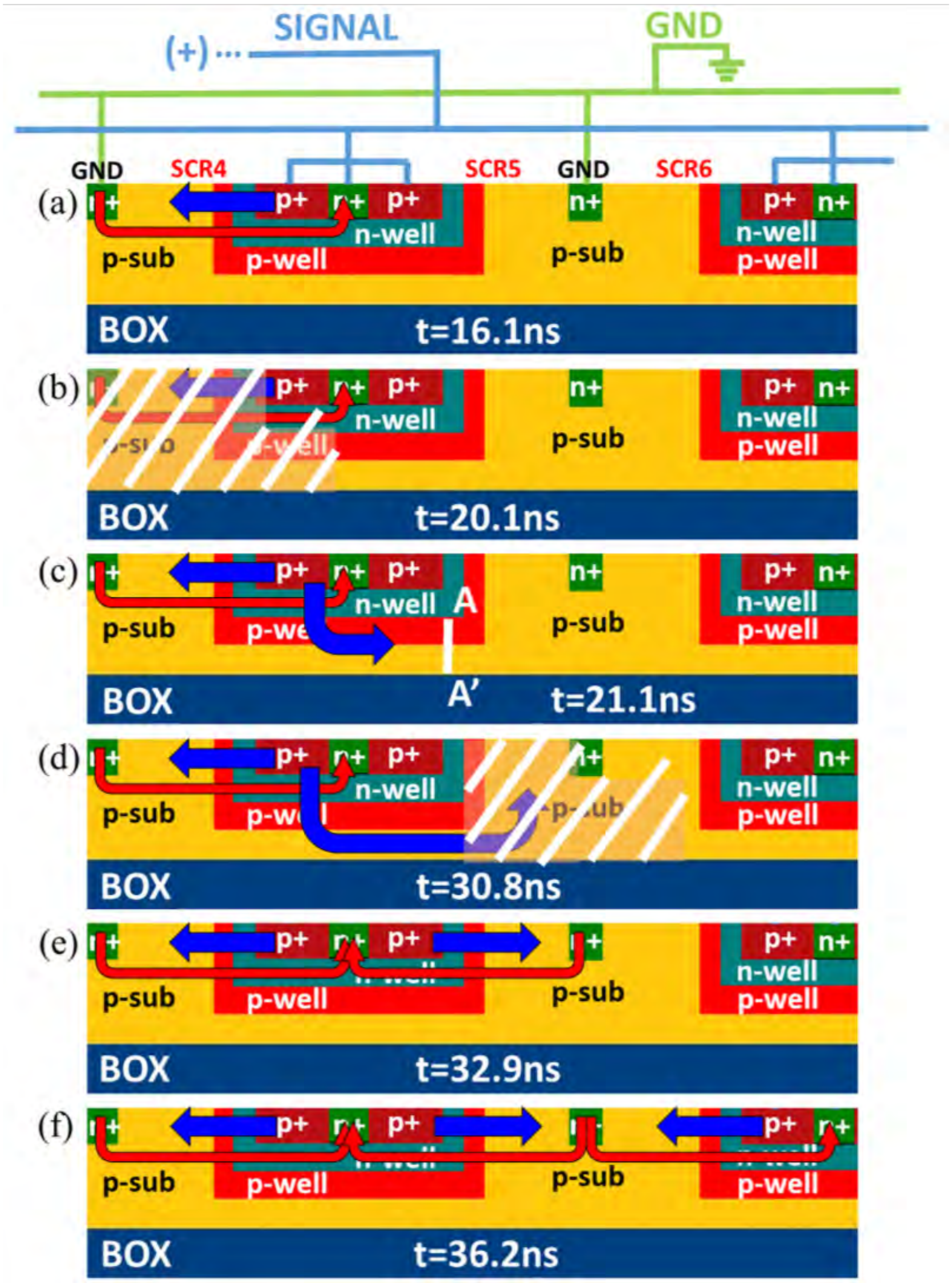

Figure 2.14: Schematics showing the different movement direction of electrons (red) and holes (blue) between the triggering of SCR4 and SCR6: (a) moment of triggering of SCR4, (b-c) are moments before triggering of SCR5, (d) GND region of SCR5 is filled by holes, (e) triggering of SCR5, (f) triggering of SCR6. The indicated time moments are consistent with Figure 2.12 (i.e. I = 1 A, R = 0 Ω). The orientation of the arrows indicate the electron or hole flow vectors, not the corresponding electrical currents.

in Figure 2.14 (b). While this is happening, the vertical pnp, which is shown with the vertical/right blue arrow in Figure 2.14 (c) becomes activate and causes further hole injection and their drift towards the common GND contact of SCR5 and SCR6 along the deep p-well. This hole current then forms the base current, $I_{b,npn}$, for the triggering of the npn transistor of SCR5. The situation can be schematically depicted with Figure 2.9. In that case, $R_{b,pwell}$ denotes the p-well resistance and the left and right SCRs correspond to SCR4 and SCR5, respectively. With the drift of holes, as shown with the dashed region in Figure 2.14 (d), part of the holes fill the region around the GND region of SCR5 and SCR6. Thus, according to the charge-controlled concept of SCR introduced in [90], these holes help to forward bias the p-sub/n+-GND junction (base/emitter junction of the npn of SCR5). The current inside the n-well of SCR5; therefore, increases as shown with the right-side red arrow in Figure 2.14 (e). When the n-well current reaches a critical value, a certain voltage difference on the $R_{n\text{-}well}$ is satisfied as discussed previously, and so the pnp of SCR5 is triggered (see the right-side blue arrow in Figure 2.14 (e)). The processes in both dashed regions are slow, diffusion-limited processes and they control τ_{long}. For a typical distances of 5 - 10 µm, the time for hole diffusion is in the range of 20 - 80 ns. In this respect, our simulated τ_{long} values in Figure 2.6 (b) are proper and also consistent with measured τ_{long} values, shown in Figure 2.6 (a). Finally with the triggering of SCR5, n+-GND contact of it strongly injects electrons and due to short diffusion distance, it takes only a few ns to reach the condition for triggering of SCR6 (see Figure 2.14 (f)). The short diffusion distance brings also a much shorter τ_{short} values compared to τ_{long}.

Our discussions showed us that the hole current $I_{b,npn}$ is an important parameter to explain the SFT mechanism. Therefore, in Figure 2.15 (a) we showed the evolution of $I_{b,npn}$ around the triggering of SCR4 and SCR5 for three different currents. The calculation of $I_{b,npn}$ was achieved by integrating the x-component of the hole current density over the deep p-well and p-sub regions through the line A-A' shown in Figure 2.14 (c). The upward and downward arrows, in Figure 2.15 (a) indicate the triggering instants of SCR4 and SCR5, respectively. As it can also be observed, $I_{b,npn}$ first rises rapidly just after the triggering of SCR4. But then this rise levels off and shows a slower increase. The reason of the fast rising edge is the rising of the SCR4 current. The reason for the rise with slower slope, on the other hand, is the above mentioned slow diffusion processes. SCR5 triggers when $I_{b,npn}$ reaches the critical condition necessary for triggering. So if we look at the magnitude of $I_{b,npn}$ at the moment of triggering of SCR5 (i.e. at the positions of downwards arrows in Figure 2.15 (a)), we observe a rise with I. These $I_{b,npn}$ values are extracted and plotted separately as a function of I in Figure 2.15 (b). Since a higher $I_{b,npn}$ current fulfills the condition for triggering of SCR5 earlier, at higher applied currents I, smaller τ_{long} values are expected. Thus, this explains the measured and simulated $\tau_{long}(J)$ dependence in Figure 2.6 (a) and (b), respectively.

At that point we also want to note that the total current flowing via the SCR is lowered due to the base current $I_{b,npn}$. However, compared to the $I_{b,npn}$ values, the current flowing via the individual SCRs is much higher. In this respect, this "missing" $I_{b,npn}$ current is not harmful for the self-sustaining operation of already triggered SCR fingers. This is because in these devices the sum of common base current gains of the npn, α_{npn}, and of the pnp,

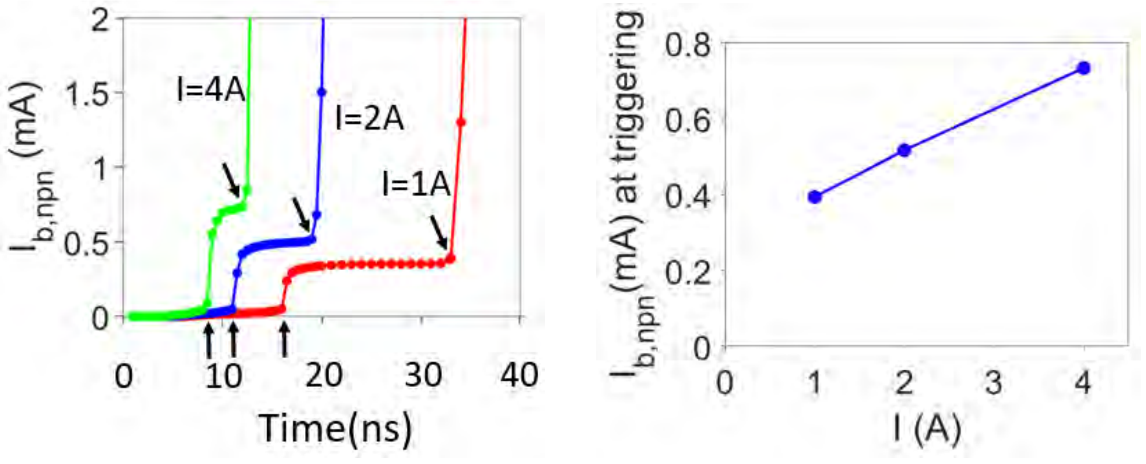

(a) (b)

Figure 2.15: (a) Simulated $I_{b,npn}$ evolution covering the moments of triggering of SCR4 (the upward arrows) and SCR5 (downward arrows) for I = 1 A, 2 A and 4 A. (b) $I_{b,npn}$ at the triggering of SCR5; R = 0 Ω.

α_{pnp}, is much higher than 1, so $\alpha_{npn} + \alpha_{pnp} \gg 1$. On the other hand, the missing holes in the triggered SCR will weaken the reverse hole injection in the inverse pnp transistor [91]. Nevertheless, for very low applied currents, one can expect that the sequential triggering will stop when there is not enough base current $I_{b,npn}$ for the triggering of the neighboring SCR finger.

2.1.4.2.3 Simultaneous triggering at high current for RT = 10 ns During our analysis, we observed that for RT = 10 ns the 8-finger simulation device triggers homogeneously for I ≥ 11 A. Figure 2.16, for instance, shows the simulated device voltage, p-emitter and n-well currents of each finger during the first 2 ns of a TLP pulse with I = 11 A. As it can be observed, the simulation shows a pronounced voltage overshoot around 13.3 V and so it causes the simultaneous triggering of all fingers as in the case of RT = 300 ps.

2.1.4.2.4 Effect of contact resistance on trigger delay In order to investigate the effect of contact resistance on trigger delay, we set R = 1 Ω (see Figure 2.8) and applied the same conditions of I = 1 A and RT = 10 ns as in Figure 2.12. Curve1 in Figure 2.17 (a) shows the resulting voltage waveform V(t). As it can be seen, for R = 1 Ω case, the voltage steps are larger than that in the case of R = 0 Ω (see Figure 2.12 (a)) and so they show a better match to the experimental values. The Curve2 in Figure 2.17 (a) represents the simulated waveform for RT = 300 ps and it is given to show that device voltage reaches the same asymptotic voltage value after the triggering of all fingers (t>50 ns) under diffrent RT conditions.

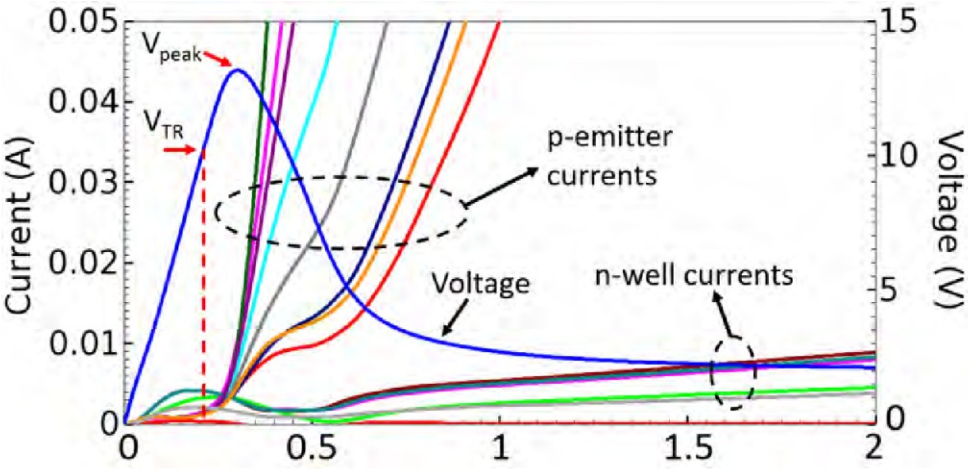

Figure 2.16: The simulated voltage, p-emitter and n-well current waveforms for I = 11 A, RT = 10 ns and R = 0 Ω.

Figure 2.6 (c) shows the effect of finite finger resistance (R = 1 Ω) on long trigger delays τ_{long} for different applied currents I. By comparing Figure 2.6 (b) and (c) one can say that with the rising R value, τ_{long} gets shorter and levels off with J faster. The reason for this behaviour is the increase of the device voltage for R > 0. Higher device voltage helps to meet the triggering condition in the next neighbor fingers faster. In this respect, if the slightly higher series resistance of the protection device would not be of primary concern, increasing R can be a design tool for shortening τ_{long} and thus improving the ESD robustness in HBM time domain.

Figure 2.17 (b) shows the voltage waveform for the condition of I = 2 A, RT = 10ns and R = 1 Ω. Similar to what we observed in measurements (see Figure 2.3 (b) and (c)), the voltage drops shifts to shorter times compared to Curve1 in Figure 2.17 (a). This shift is demonstrated with the arrows.

At that point it may also worth to discuss the the origin of voltage peaks in the simulated voltage waveforms for t < 10 ns observed in Figure 2.12 (a), Curve1 of Figure 2.17 (a) and Figure 2.17 (b). A similar voltage peak also occurs in the experiments (see Figure 2.3 (b) and (c)). Although in the first place one may think that it is because of the self-heating effect, its origin is purely electrical. Our RT value is 10 ns. Hence, since some of the fingers trigger before the end of the rising edge of the pulse, the voltage on the device rises to accommodate the imposed current.

2.1.4.2.5 Effect of ambient temperature on trigger delay Figure 2.18 compares the simulated voltage waveforms V(t) for three ambient temperatures. As it can be observed, τ_{long} shortens with the increasing ambient temperature. The reason for this is the increase in the n-well resistance $R_{\text{n-well}}$ with temperature. As $R_{\text{n-well}}$ increases, a smaller n-well current becomes enough to satisfy the triggering condition of the pnp of an SCR under

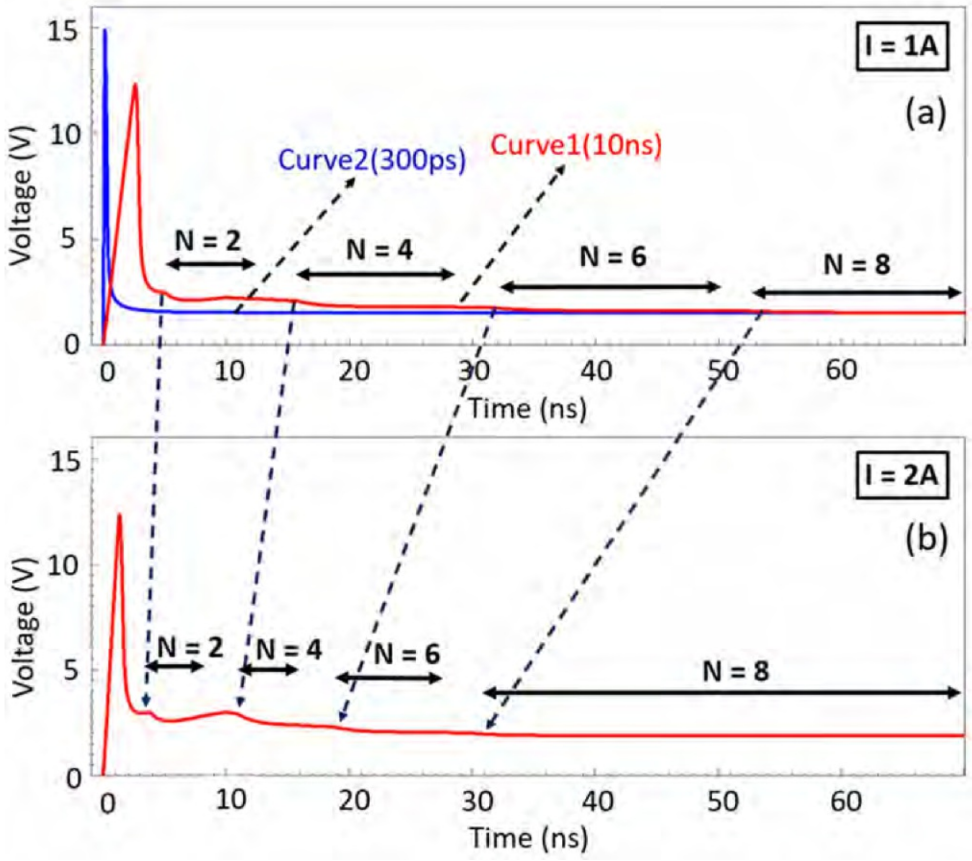

Figure 2.17: Simulated voltage waveforms for (a) RT = 10 ns (Curve1) and RT = 300 ps (Curve2) under I = 1 A (b) RT = 10 ns and I = 2 A. R = 1 Ω. The number of triggered fingers N are indicated.

the same applied current (see Figure 2.9) and so the SCR triggers earlier. Figure 2.19 shows the evolution of n-well current at the triggering of fingers for each temperature case. Rising of temperature by 100°C shortens the longest trigger delay by about 15 ns.

2.1.4.2.6 Effect of active silicon layer thickness on trigger delay When we increase the thickness of active silicon layer in our simulation structure (see Figure 2.8), a similar dependence on the average one-dimensional current density, J, as in Figure 2.6 (b) is observed in long trigger delay τ_{long} values. In all simulations SCR1 triggers first and other inner fingers SCR2, SCR3 and alternately up to SCR8 trigger sequentially. SCR0, on the other hand, stays inactive as discussed before. Therefore, $\tau_{6,7}$ always become the the longest trigger delay. In this respect, in order to understand the effect of active silicon layer thickness on trigger delay, we compare $\tau_{6,7}$ values for different thicknesses in an arbitrary unit. Figure 2.20 shows this comparison.

As we discussed previously, holes from triggered fingers move through the deep p-well/p-sub and bias the npn of the non-triggered neighbor finger which will trigger next.

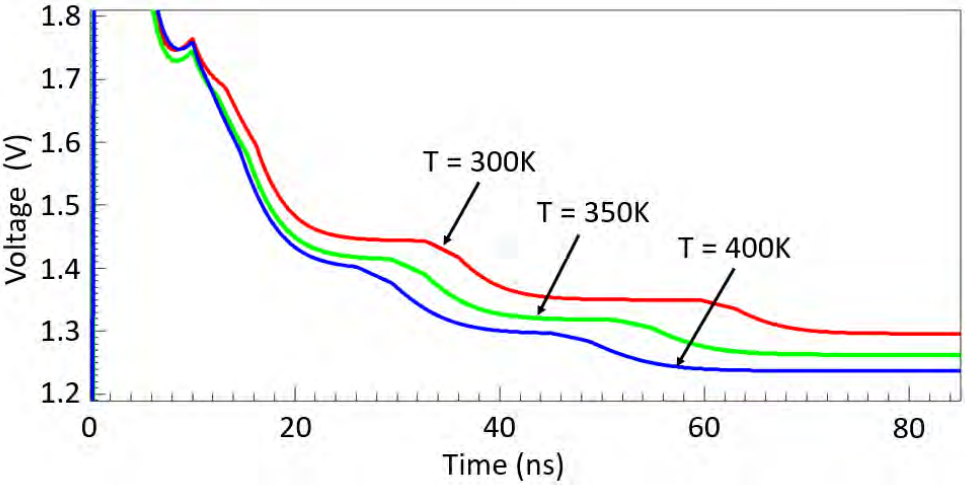

Figure 2.18: Comparison of simulated voltage waveforms for different ambient temperature for I = 1 A, RT = 10 ns and R = 0 Ω.

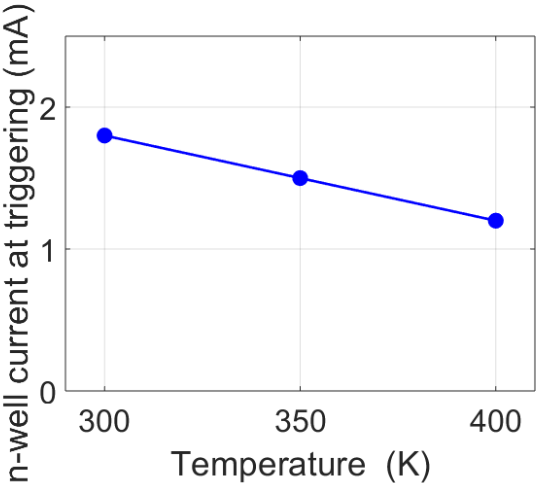

Figure 2.19: n-well currents at the triggering of fingers for different temperatures. I = 1 A, RT = 10 ns and R = 0 Ω.

During this movement, holes face with the resistance of deep p-well/p-sub region. In this respect, with the increase of active silicon layer thickness, the effective value of this resistance decreases and so holes move faster. More charge; therefore, is transported to the region around the GND due to higher $I_{b,npn}$ and so the base/emitter junction of npn is forward biased faster. Faster npn triggering then brings shorter τ_{long} values. In Figure 2.20, we observe this effect clearly until the active silicon layer thickness of 0.6.

Most of the holes which move towards the neighbor finger move within the thickness of 0.6 from the surface of the active silicon layer. The amount of holes from surface into deeper region of active silicon layer decreases exponentially. Therefore, the enhancement of active silicon layer more than 0.6 does not strongly affect the actual resistance of deep p-well region which holes are experiencing. However, some of the holes still moves into

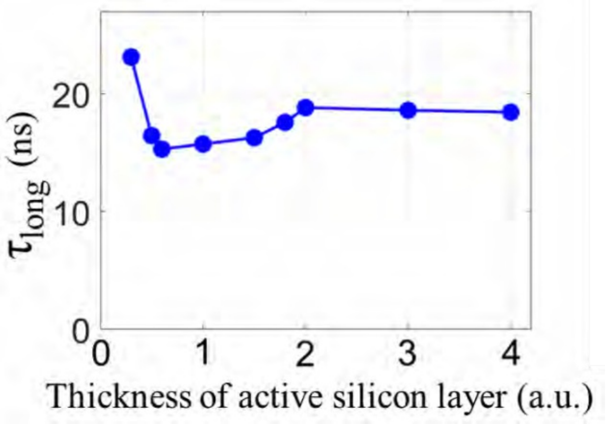

Figure 2.20: Comparison of the longest trigger delay ($\tau_{6,7}$) values for different active silicon layer thicknesses in an arbitrary unit. I = 1 A, RT = 10 ns and R = 0 Ω.

deeper regions of the p-sub and do not contribute to the base current $I_{b,npn}$. In this case, a slight increase in τ_{long} occurs. The rise in τ_{long} values between the active silicon layer thicknesses of 0.6 and 2 in Figure 2.20 can be attributed to this reason. After the active silicon layer thickness of 2; however, the moving holes into deeper region of p-sub do not play a significant role anymore and τ_{long} values nearly do not change.

2.2 Analysis with half sinusoidal pulse

2.2.1 Investigated device structure

In this section we investigate the triggering behavior of a 8-finger SCR by applying a half sinusoidal pulse. Figure 2.21 (a) shows the cross-section view of the studied SCR structure at a region where p-doped trigger taps (TTs) exist. Figure 2.21 (b) and (c), in addition, shows the enlarged image for the regions of a finger where TT does not exist and exist, respectively. Figure 2.21 (d), on the other hand, shows the top view of the layout of a finger. The p-doped TTs help to decrease the trigger voltage V_{TR} and so triggering starts at n-well/TT junctions. All fingers stay on a lightly p-doped bulk silicon substrate and there is no shallow trench isolation (STI) in between them; therefore, they all are coupled through the same p-substrate.

The p+-emitters of pnp transistors and n-well regions share the same contact metallization and the positive half sinusoidal stress is applied on them. The n+-emitter of the npn transistors and p-well regions, on the other hand, share the same contact metallization which is connected to ground. The n-well serves both as a base and a base resistor of the pnp transistor whereas the p-well serves both as a base and a base resistor of the npn transistor. The n-well and p-well regions, moreover, serves as a collector of npn and pnp transistors, respectively.

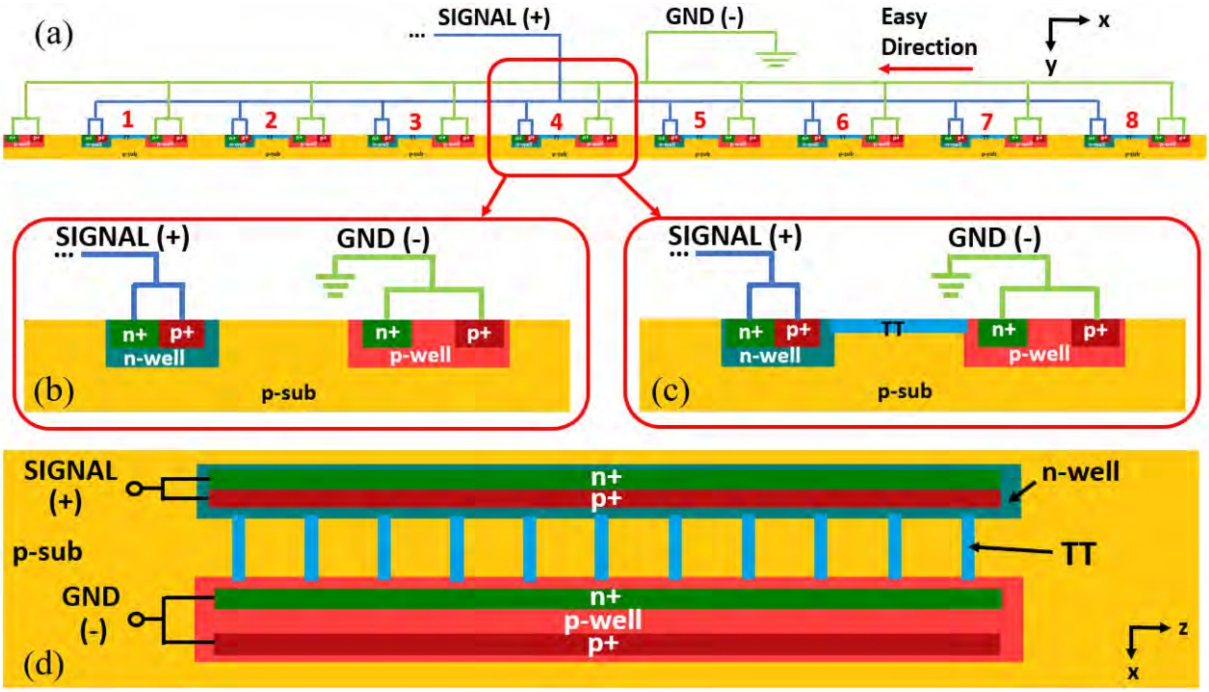

Figure 2.21: (a) Simplified cross section of the studied 8-finger SCR structure on which trigger taps (TTs) are shown. The zoomed image for regions (b) without trigger taps (w/o-TTs) and (c) with trigger taps (w-TTs) (d) Top view of a finger.

SCRs are labeled from ‘1’ to ‘8’, in other words from SCR1 to SCR8. The GND contact at the left side of SCR1 is put in order to have 8 forward biased pn junctions in total in the case of opposite bias. We will not investigate the pn junction behaviour here but the structure is designed so that it becomes SCR or forward biased pn junction in the case of positive or negative stress applied to the Signal contacts, respectively.

2.2.2 Experimental results

2.2.2.1 First investigation with Surge

Our purpose was to investigate the triggering behaviour of our structure under surge (see section 1.4.4). For this purpose, first we created a surge pulse by modifying the square pulse of HP8114A Pulse Generator. We used this pulse generator because it was a device that we know how to create rectangular pulses in the microsecond range in a controlled manner. Figure 2.22 shows the used circuit parameters to get surge from a rectangular pulse [47, 58]. It is plotted by using LTspice. There, the voltage source V1 represents the HP8114A Pulse Generator. A pulse from HP8114A Pulse Generator is sent with a rise time value of RT = 7 ns, which is also equal to its fall time value (FT = 7 ns). That is why, in Figure 2.22, for instance, an 80V pulse with RT = 7 ns and PW = 50 µs is provided to the circuit. R2 resistor represents the internal resistance at the output of the

HP8114A Pulse Generator. C1 capacitor, on the other hand, is used for arranging the falling edge of the surge pulse while L1 is benefited to get a peak around t = 10 µs. R3 represents the SCR structure.

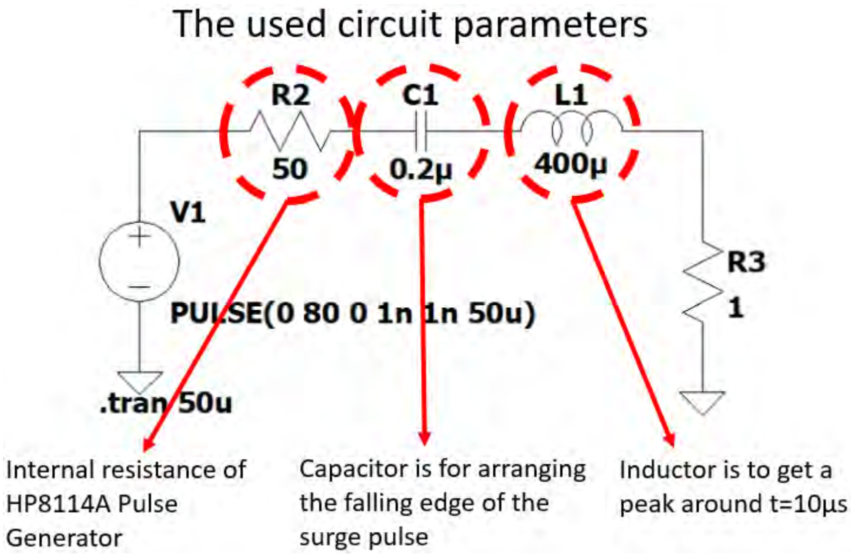

Figure 2.22: The used circuit parameters to get a surge from HP8114A Pulse Generator. The circuit is plotted with LTspice.

With the circuit configuration shown in Figure 2.22, we obtained the current waveform I(t) displayed in Figure 2.23 from HP8114A Pulse Generator. As it can be observed, the shape of the waveform we get is quite close the surge pulse discussed in section 1.4.4. The problem here; however, the maximum voltage that HP8114A Pulse Generator can provide is 100 V. That means that maximum current that we can send to the circuit is around 1.25 A. Under this applied current, unfortunately, we just observe the triggering of one finger instead of a sequential finger triggering. This is because this current is just enough to trigger one finger. With this setup; therefore, we could not investigate the sequential finger triggering observed in this SCR structure under the surge pulse.

To deal with this issue, we decided to change our pulser. Another pulse generator we have that can provide pulses in microsecond range was HP8116A Pulse/Function Generator. With this device we cannot apply surge but a sinusoidal pulse. Since the rising edge of a surge pulse is quite similar to the rising edge of a sinusoidal wave, applying a sinusoidal pulse can provide us the understanding of how sequential finger triggering occurs under the surge. Although the maximum amplitude of the voltage waveform that this pulser can provide is 8 V, with the help of an internally designed amplifier in TU Wien, we were able to amplify the signal by 20 times. The amplifier was directly connected to the output of the HP8116A Pulse/Function Generator and there was a 10 Ω resistor between the output of the amplifier and our SCR device. With this circuit configuration and the pulse generator; therefore, we were able to provide high currents to our SCR up to 16 A and observe sequential finger triggering (SFT). Figure 2.24 shows an example of

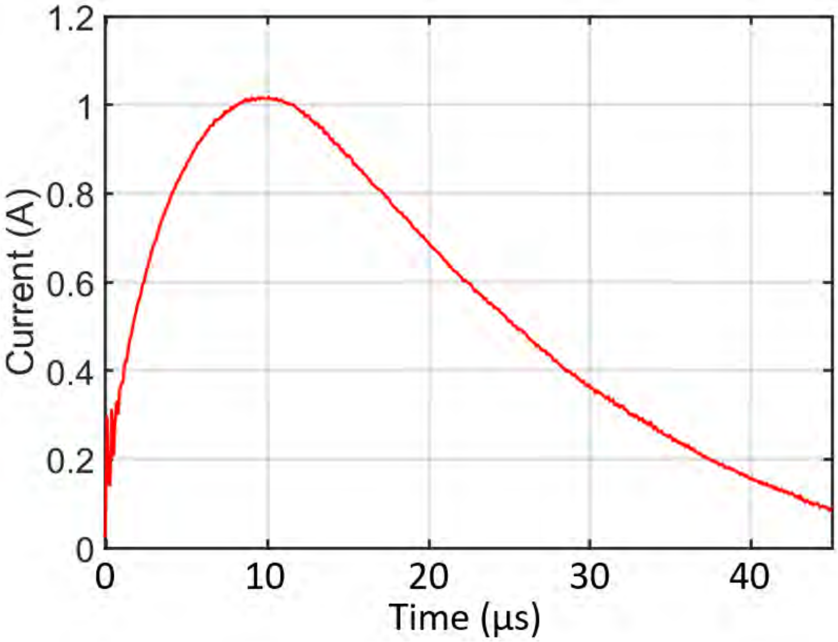

Figure 2.23: The surge pulse obtained from HP8114A Pulse Generator by using the circuit configuration shown in Figure 2.22

the half sinusoidal pulse that we applied to our SCR devices. The pulse in Figure 2.24 is simulated but the ones applied to the experimental devices were also the same.

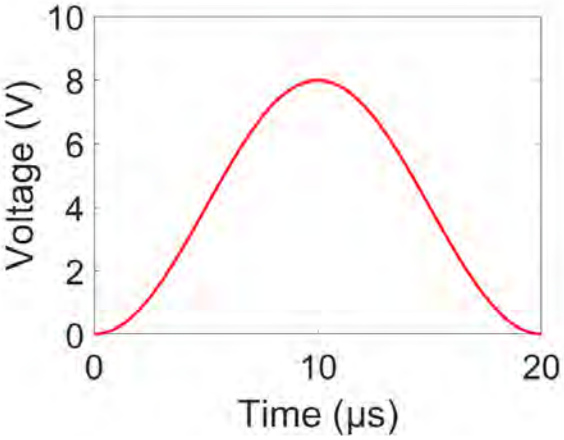

Figure 2.24: An example of the half sinusoidal pulse that we applied to our SCR devices

2.2.2.2 Sequential finger triggering with half sinusoidal pulse

Figure 2.25 represents the typical TLP IV curve for RT = 10 ns and PW = 100 ns. As it can be observed, there is no jump for currents I > 0.25 A. Thus, based on our previous discussion about sequential finger triggering in section 2.1, it can be stated that there is no SFT for currents I > 0.25 A under this specific TLP pulse condition. Although we do not observe a drop on the TLP IV curve due to SFT, it still provides us a knowledge about holding voltage V_{HOLD}. By knowing V_{HOLD} value in our SCR, we can determine whether we have SFT or not in our further analyses once we see successive voltage drop near V_{HOLD}. The V_{HOLD} in our SCR is around 1.6 V.

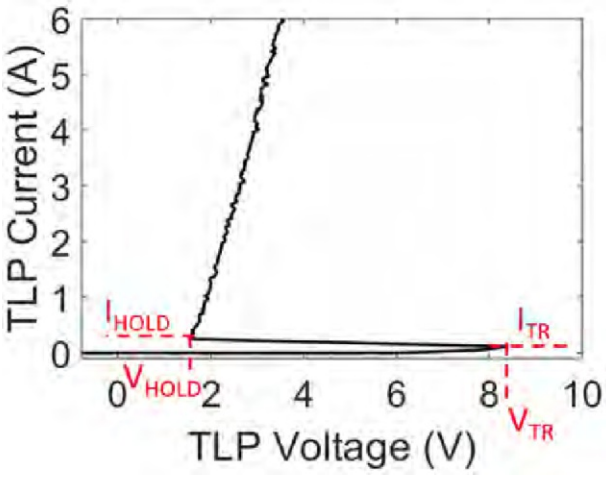

Figure 2.25: TLP IV curve for RT=10ns and PW = 100ns. The averaging window is 75-90ns.

2.2.2.2.1 Current and voltage waveforms Once we applied the half sinusoidal pulse at high currents as shown in Figure 2.24, we observed the sequential finger triggering (SFT) in our SCR device. During these experiments, we also recognized that finger triggering was happening in both directions. The position of the first triggered finger was changing from device to device. However, depending on the position of the first triggered finger, the next fingers were triggering towards both the right and the left sides. In addition, compared to SFT from SCR1 to SCR8 direction, the SFT from SCR8 to SCR1 direction was requiring less amount of applied current for the same amount of finger triggering. In other words, fingers were triggering easier if they trigger towards the left direction (see Figure 2.21 (a)). For convenience, we called this direction as the *easy* direction and the opposite direction; therefore; was called as the *difficult* direction.

Figure 2.26 (a), for instance, shows the TIM scan across the fingers at some selected time instants (indicated on right sides of the figures) for an experiment where fingers trigger in the difficult (towards the right) direction. In this experiment, SCR2 triggers first. Then, since the left direction is the easy direction, SCR1 triggers next. After the triggering of SCR1, since there is no finger left in the easy direction, SCR3, SCR4, SCR5 and SCR6 trigger sequentially in the difficult direction. Figure 2.26 (b), on the other hand, presents the TIM scan for an experiment with the triggering in the easy direction. There, SCR5 triggers first and then the neighbor fingers in the easy direction (towards the left, see Figure 2.21 (a)) trigger sequentially until SCR1. In Figure 2.26 (b) again the TIM scan is conducted across the fingers and the extracted phase shift values at some

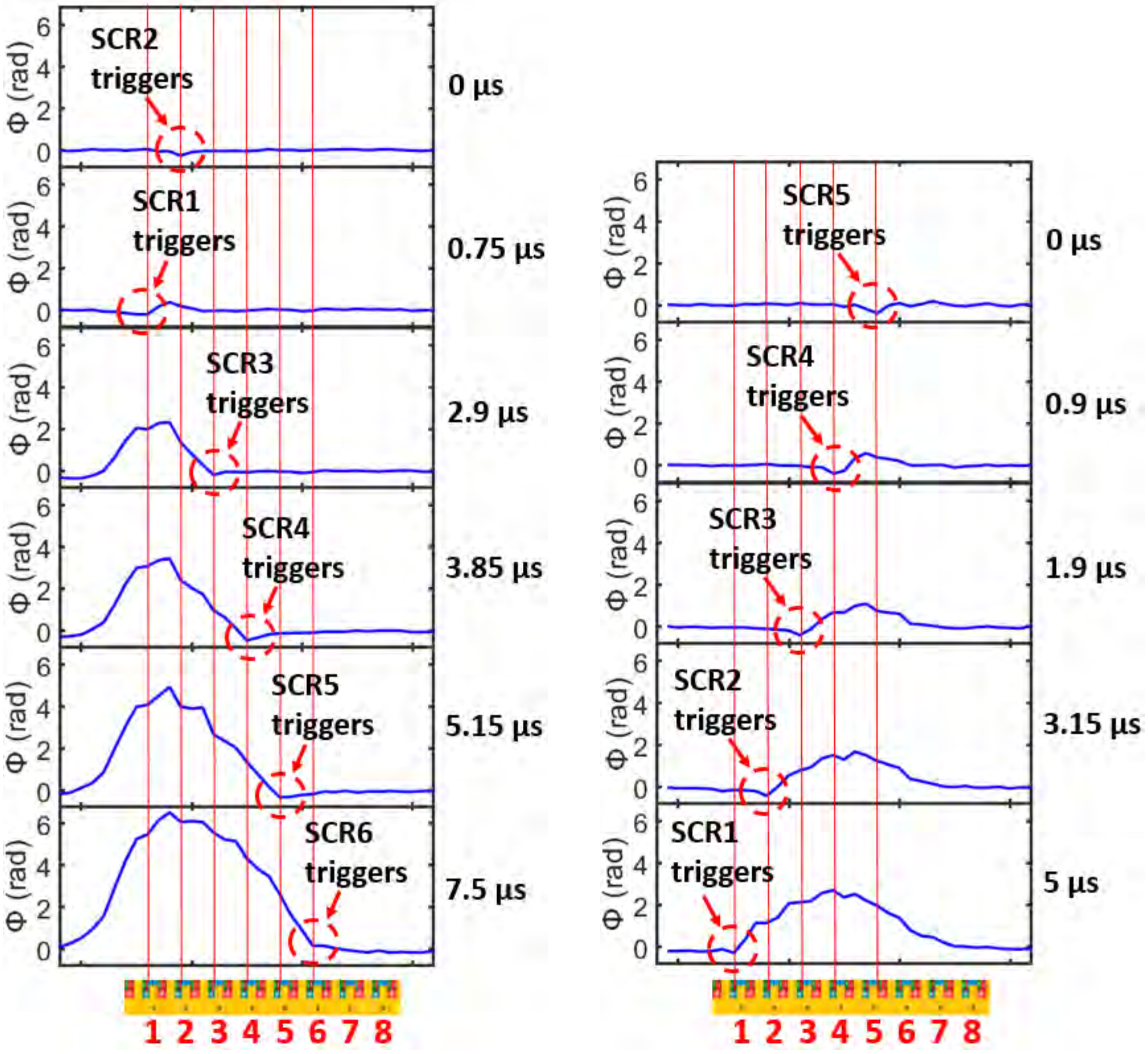

(a) (b)

Figure 2.26: TIM scan across the fingers at some selected time instants under the (a) 42 V and (b) 30 V half sinusoidal pulse to show sequential finger triggering in difficult (towards the right) and easy (towards the left) directions, respectively. The positive value of phase shift at longer times is due to temperature increase caused by the self-heating effect.

selected time instants (indicated on right sides of the figures) are given. At that point, it is worth to remark that in Figure 2.26, the number of total triggered fingers in difficult and easy directions are different and it is 6 and 5, respectively. This can be attributed to that the experiments were conducted with different applied voltages from HP8116A Pulse/Function Generator. For the experiments in difficult and easy directions, 42 V and 30 V half sinusoidal pulses were applied from HP8116A Pulse/Function Generator, respectively. In both TIM scans, the origin of the time instances is not the pulse beginning but the triggering of the first finger. So in the experiment with the triggering in the difficult direction (see Figure 2.26 (a)), for instance, the origin of the time instances is the triggering of SCR2.

In Figure 2.26, it can be observed that the phase shift values increase with time. The reason for this is the self-heating effect. As discussed in section 1.5.2, for a long pulse duration, the thermally induced phase shift term dominates the free carrier induced contributions and so we observe high positive phase shift values. If we focus on the time duration around the triggering of a finger, on the other hand, the negative phase shift due to injection of free carriers can be clearly observed. At time instance t = 0 in Figure 2.27, for instance, the negative phase shift at the triggering of SCR5, which is also presented in Figure 2.26 (b), can be seen.

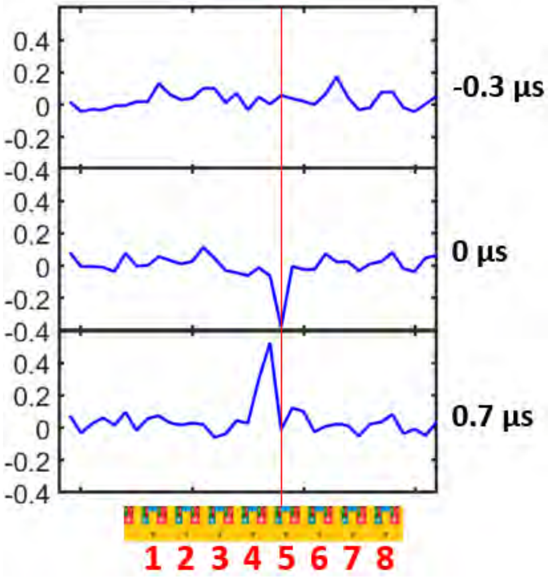

Figure 2.27: Phase shift values around the triggering of SCR5 presented in Figure 2.26 (b)

The red lines in Figure 2.28 (a) and (b) show the experimental current and voltage waveforms for the sequential finger triggering in difficult direction under 42 V half sinusoidal voltage pulse from HP8116A Pulse/Function Generator. Figure 2.28 (c), on the other hand, is the enlarged image of Figure 2.28 (b) to see voltage drops clearly. The peak values of current and voltage waveforms are 3.61 A and 8.36 V, respectively. As indicated by the numbers, there are six successive voltage drops and the last five of them is happening near the holding voltage V_{HOLD} = 1.6 V of the device. Therefore, as we discussed before, it is a strong sign of sequential finger triggering (SFT).

The blue lines in Figure 2.28 (d) and (e), on the other hand, presents the experimental current and voltage waveforms in the easy direction under 30 V half sinusoidal voltage pulse from HP8116A Pulse/Function Generator. Figure 2.28 (f), on the other hand, is the zoomed image of Figure 2.28 (e) to see voltage drops clearly. The peak values of current and voltage waveforms are 2.64 A and 8.39 V, respectively. As indicated by the numbers, there are five successive voltage drops and the last four of them is happening near the holding voltage V_{HOLD} = 1.6 V. It is again a strong sign of SFT.

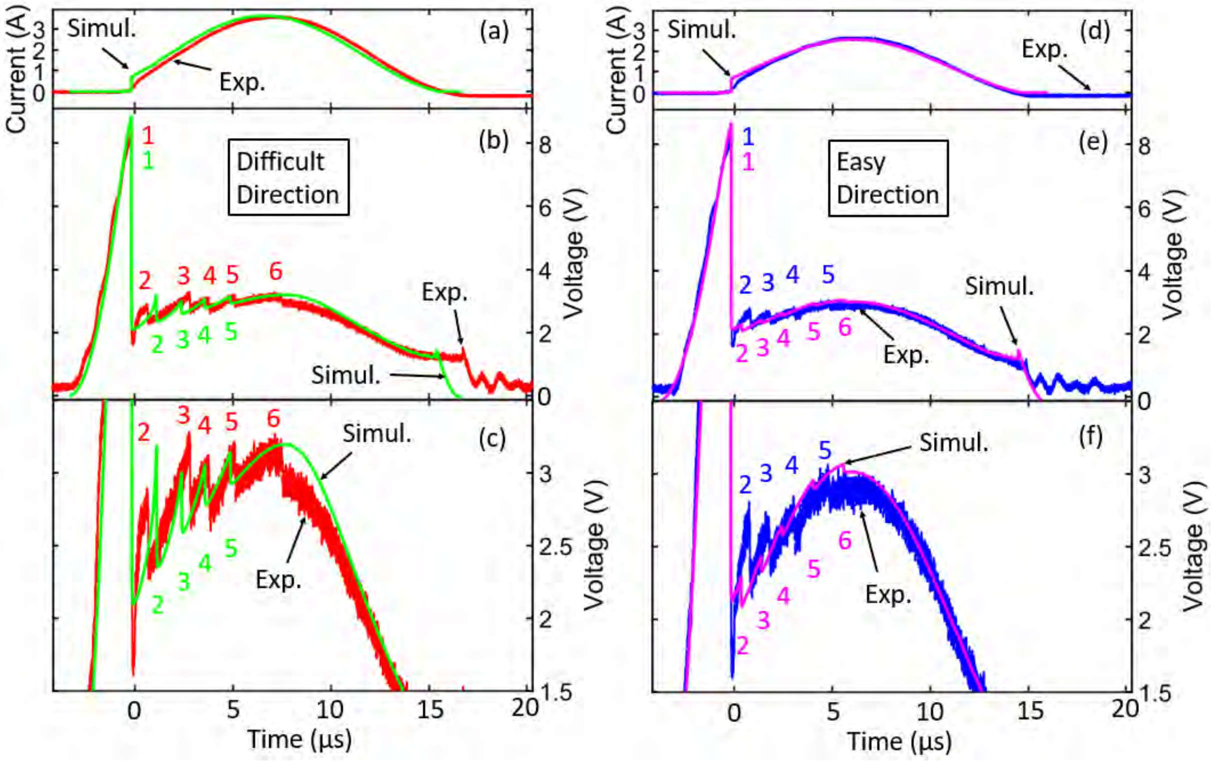

Figure 2.28: Experimental and simulated (a) current and (b) voltage waveforms for the sequential finger triggering in the difficult direction under 42 V half sinusoidal pulse. (c) The enlarged image of (b). Experimental and simulated (d) current and (e) voltage waveforms for the sequential finger triggering in the easy direction under 30 V half sinusoidal pulse. (f) The zoomed image of (e).

As it can be observed in Figure 2.28 (b) and (e), the voltage on the device increases a bit during triggering for both triggering directions. The reason for this is the rise of the current. The voltage on the device is rising in order to accommodate the imposed current.

In order to understand the difference in these two directions in terms of finger triggering and to check whether there is a certain trend for required currents at triggering, we plotted the current per already triggered fingers for the experiments in Figure 2.26 at the moment of the triggering of the next finger. Figure 2.29 shows these plots. The blue and red lines in Figure 2.29; therefore, show the experimental current per triggered finger at the moment of the triggering of a new finger for the easy (towards the left) and difficult (towards the right) directions, respectively. The experimental data for the difficult and easy directions in Figure 2.29 are extracted from Figure 2.28 (a, b) and Figure 2.28 (d, e), respectively.

As it can be observed in Figure 2.29, in both directions (easy and difficult), the amount of current per triggered finger at the moment of the sequential triggering of the neighbor finger is decreasing with the increasing number of triggered fingers. This decrease, in addition, show a tendency to level off at high number of triggered fingers. The amount of required current in the difficult direction; however, is still considerably higher than that in the easy direction. Besides that, it may catch one's eyes that the first value in the difficult direction is in the range of values in the easy (towards the left) direction. This is because in this experiment (see Figure 2.26 (a)) SCR1 triggers in the easy (towards the left) direction after the triggering of SCR2.

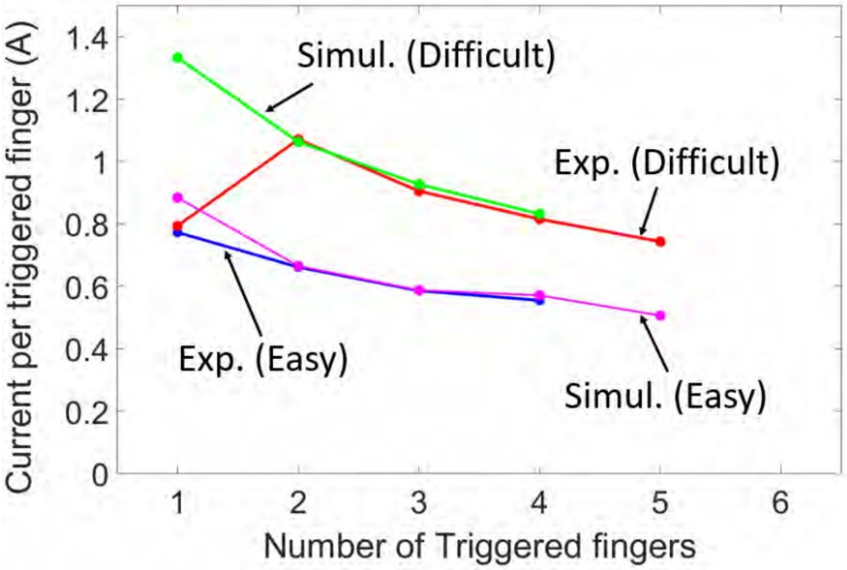

Figure 2.29: Current per triggered finger at the moment of the triggering of a new finger in the easy (towards the left) and difficult (towards the right) directions for experiments and simulations

2.2.3 TCAD simulation approach

For simulation purposes, an 8-finger 2D device structure was created by using Synopsys Sentaurus TCAD as shown in Figure 2.30 (a). Since the experimental device stays on a lightly p-doped bulk silicon, a 200 µm silicon layer is used in the simulation structure. Making the silicon layer thicker than 200 µm was not altering the results. Therefore, in order to decrease the simulation time, we did not make it larger. The surge pulse we are applying is in the microsecond range and so, as discussed in TIM scans previously (see Figure 2.26), we observe self-heating effect. Hence, in order to allow heat diffusion towards the sides of the simulation structure as in the experimental device, it is extended by 100 µm at both sides. Besides that since we have self-heating effect, conducting an isothermal drift-diffusion simulation is not enough to reveal the device behaviour. A thermodynamic simulation is needed. In this respect, in order to apply thermodynamic model, a thermode contact is implemented at the bottom of the structure and its temperature value is set to ambient temperature of 300 K. Due to solving complex thermal equtions, a simulation with thermodynamic model takes more time than a simulation with isothermal drift-diffusion model. However, in order to match simulation and experimental results, this is a trade off to overcome. The vertical lines between the fingers is due to properties of Sentaurus and it does not affect the device behavior. Neumann boundary conditions are applied at the edges of simulation region.

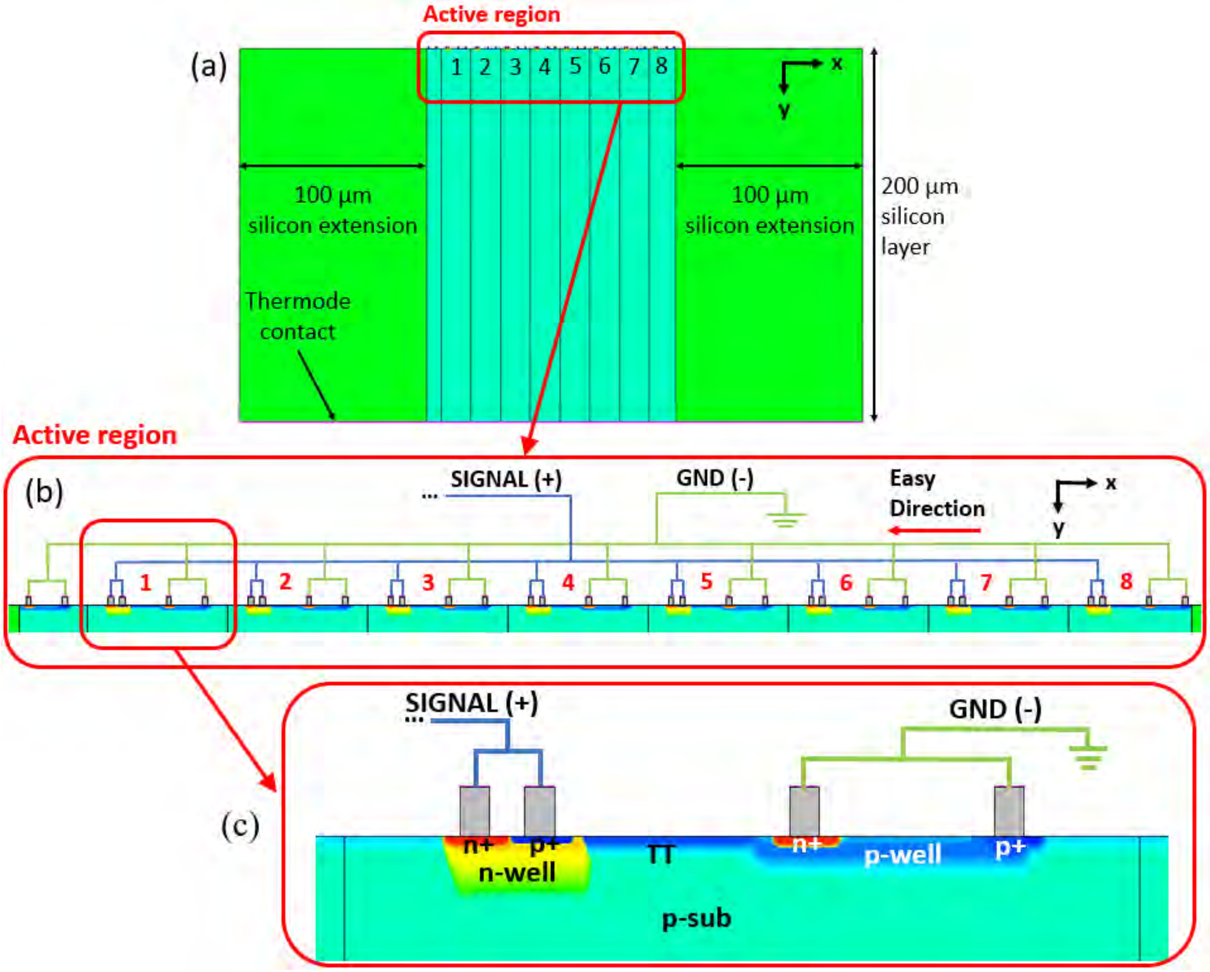

Figure 2.30: (a) Simulation setup with separate contacts for each SCR current component in addition to the bottom thermode contact. (b) Enlarged image of the active region where SCR fingers exist. (c) The zoomed image for a finger.

Figure 2.30 (b) shows inside of the active region where SCR fingers exist and Figure 2.30 (c) presents the enlarged image for a finger. In order to make individual analysis of current components on each SCR finger, separate contacts are implemented on top of p+-SIGNAL, n+ region of n-wells, p+ region of p-wells and n+-GND regions. The currents through these contacts are called p-emitter, n-well, p-well and n-emitter currents. We calibrated the simulation in detail in terms of doping concentration as well as cabling and contact resistances as will be discussed below.

2.2.4 Simulation results

2.2.4.1 Calibration of the simulation setup

Since the TIM setup that we used in the experiments has a 2-point-probe configuration, so as to calibrate the simulations with the experiments in terms of current/voltage waveforms and phase shift values; in addition to doping concentrations, we also needed to consider cabling and contact resistances. Figure 2.31 schematically shows the simulation setup we used.

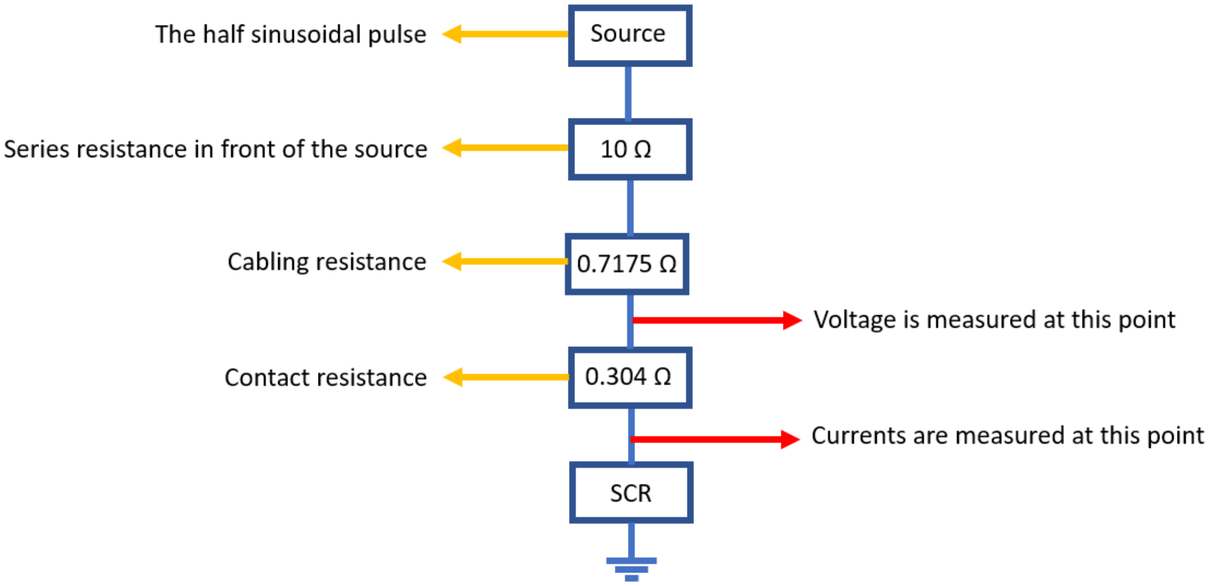

Figure 2.31: Schematic representation of the simulation setup.

Under the 12 V half sinusoidal pulse, only one finger was triggering in the experimental device. Therefore, in order to gain time, we started calibration under the condition of one finger triggering. The idea here was that if we can achieve a successful matching for the triggering of one finger; by using the same simulation setup, we could achieve also the matching for higher number of triggering. Current, voltage, power and energy waveforms in Figure 2.32 (a), (b), (c) and (d), respectively show that we have a very successfully calibrated simulation setup.

In addition to data in Figure 2.32, Figure 2.33 (a)-(d) compares the phase shift values from experiments and simulations at some selected time instants (indicated on right sides of the figures) for the triggering of one finger (SCR4) under the 12 V half sinusoidal pulse. The origin of the time instances again is not the pulse beginning but the triggering of the first finger (SCR4 in this case). Figure 2.33 (e) compares the maximum phase shift values. The simulation data in Figure 2.33 (e) is extracted from Figure 2.33 (a)-(d). The maximum temperatures during the simulation, on the other hand, is shown in Figure 2.33 (f). The maximum temperature values at the selected time instances are also included

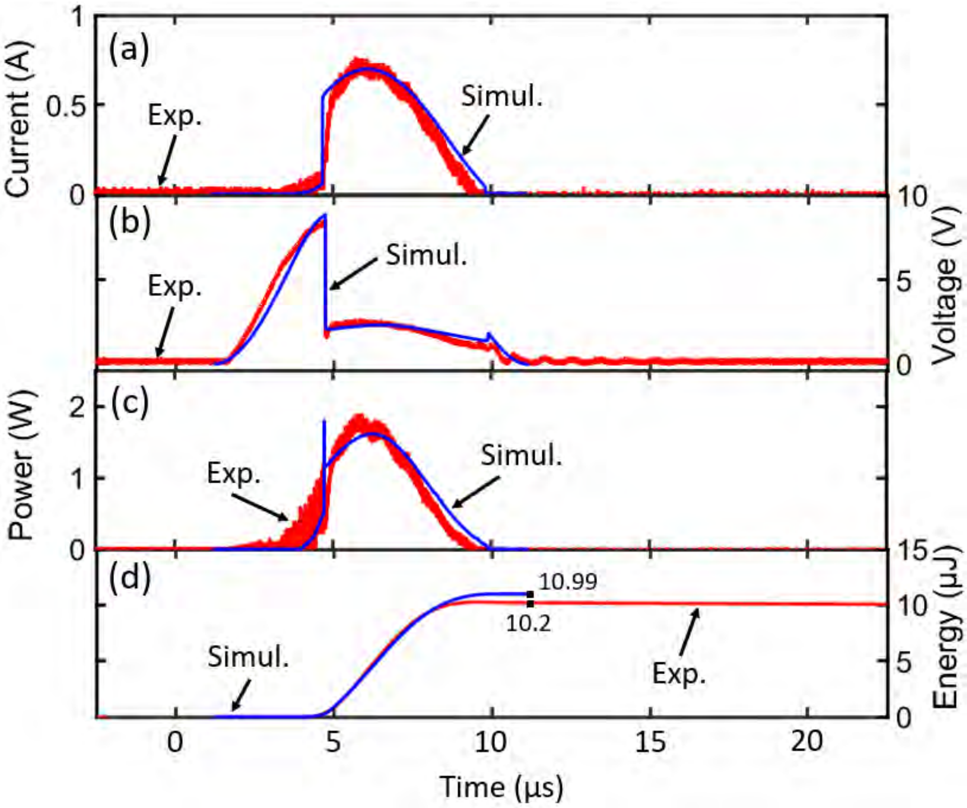

Figure 2.32: Comparison of experimental and simulated (a) current, (b) voltage, (c) power and (d) energy waveforms under the 12 V half sinusoidal pulse.

in Figure 2.33 (e). As it can be observed, the maximum phase shift and the maximum temperature are not happening at the same time. This is due to the property of the phase extraction technique. As it is explained in TIM technique section in chapter1 (section 1.5.2), phase shift is extracted through the the silicon layer in z-direction. Therefore, once the maximum temperature is reached at the top side of the silicon layer, it takes a bit time for heat to diffuse into the silicon layer and so to cause the maximum phase shift. All these results confirm that our simulation setup is very well calibrated with the experiments.

2.2.4.2 Condition for Triggering

Before investigating the current and voltage waveforms for finger triggering in the easy and difficult directions, it is better here to explain the general condition for triggering to make further subjects easier to understand for the reader. In general, an impact ionization occurs at the reverse biased n-well/TT junctions of all fingers prior to triggering of the SCR. Then, with the increase of the device voltage, the p+-SIGNAL to n-well and the p-well to n+-GND junctions become forward biased. A voltage difference; therefore, occurs on the $R_{\text{n-well}}$ and $R_{\text{p-well}}$ resistances, respectively. Since the effective resistance of $R_{\text{p-well}}$

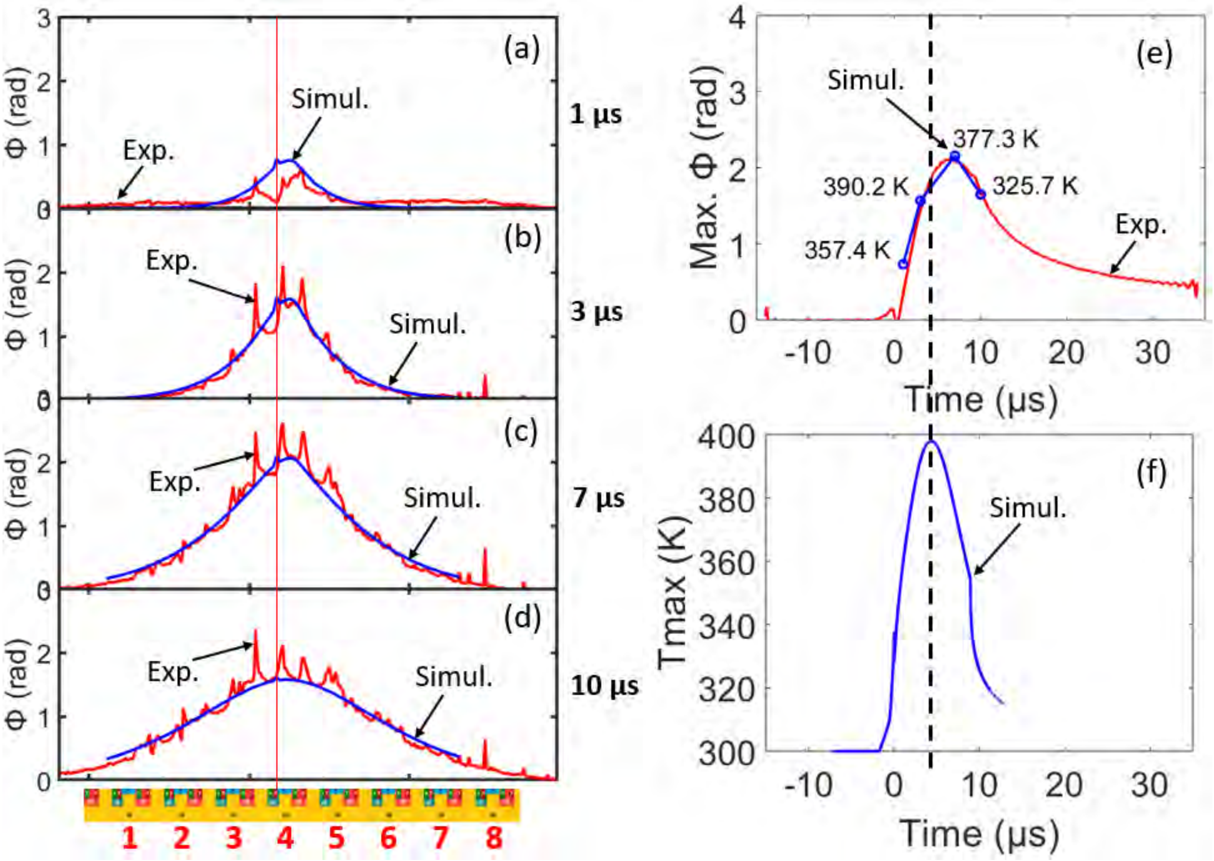

Figure 2.33: (a)-(d) Comparison of the phase shift values from experiments and simulations at some selected time instants for triggering of one finger (SCR4) under the 12 V half sinusoidal pulse. The origin of the time instances is the triggering of SCR4. (e) Comparison of the maximum phase shift values. (f) The maximum temperature values during the simulation.

(175.1 Ω) is bigger than the effective resistance of $R_{\text{n-well}}$ (31.2 Ω), a potential drop on $R_{\text{p-well}}$ which is sufficient to trigger the npn is reached earlier and so npn triggers. Since now npn becomes active, the collector current, $I_{c,\text{npn}}$, of the npn flows through the n-well. Then, once the potential drop on $R_{\text{n-well}}$ becomes sufficiently high to bias the emitter/base junction of pnp (p+/n-well junction of the SCR finger), the p-emitter current of the pnp starts to inject and so the device is driven into self-sustaining SCR action. This indicates the triggering moment of the SCR. The situation can be depicted in a lumped element representation of SCR as shown inside of the dashed box in Figure 2.34.

2.2.4.3 Current and voltage waveforms for triggerings in the easy and dificult directions

Since we have a very well calibrated simulation setup, now we can simulate the triggering in the difficult and easy directions observed in the experiments by applying the same pulses that we applied in the experiments. For the triggering in the difficult direction, a 42 V

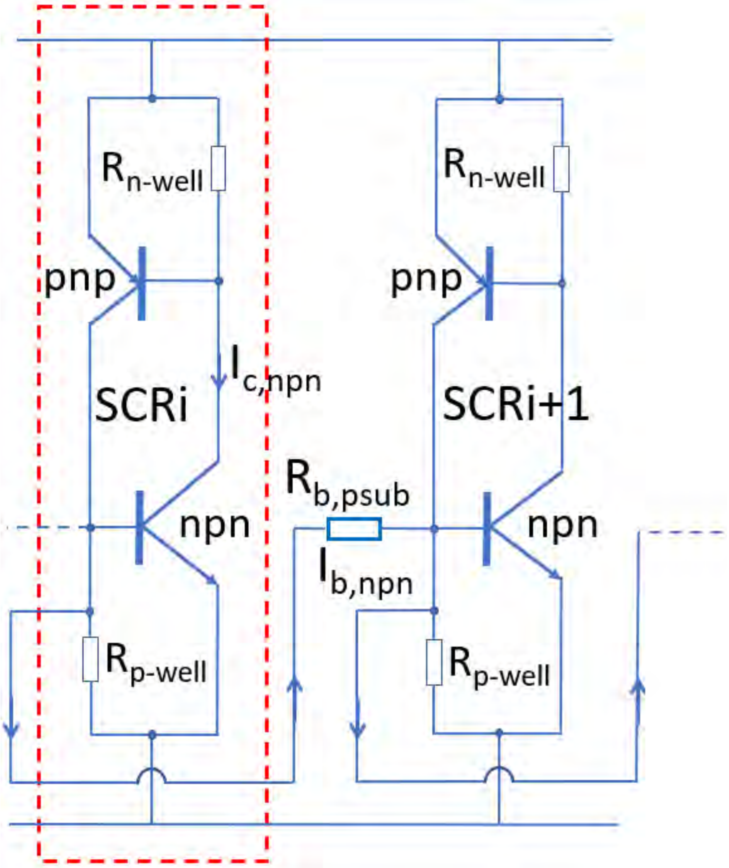

Figure 2.34: Lumped element representation of two SCRs. The hole base current $I_{b,npn}$ from SCRi to SCRi+1 is indicated

half sinusoidal pulse; therefore, is applied to the simulation setup as in the experiments. Figure 2.35 (a) shows the simulated p-emitter and n-well currents while Figure 2.36 (a) presents the simulated n-emitter and p-well currents. Total current and voltage waveforms are also given in these figures. Figure 2.35 (b) and Figure 2.36 (b), on the other hand, show the enlarged current waveforms by zooming inside of the dashed rectangles in Figure 2.35 (a) and Figure 2.36 (a), respectively. The dotted lines relate the particular current component to its corresponding contact. If we put all the waveforms in one plot, it was becoming very hard to differentiate the waveforms from each other. Therefore, in order to help reader to understand the drawings, we put them as separate plots. In addition to that, the waveforms for the total current on the device and the voltage can also be found in Figure 2.28 (a) and (b), respectively. As it can be seen in Figure 2.28, the simulated current and voltage waveforms show quite good matching to the experimental results. If we extract the current per triggered finger at the moment of the triggering of the next finger, the simulation data again matches quite well to the experimental result as shown in Figure 2.29 (compare Simul.(Difficult) and Exp. (Difficult) curves in Figure 2.29).

In Figure 2.35 (a) and (b), the rapid rise of the p-emitter currents, which dominate

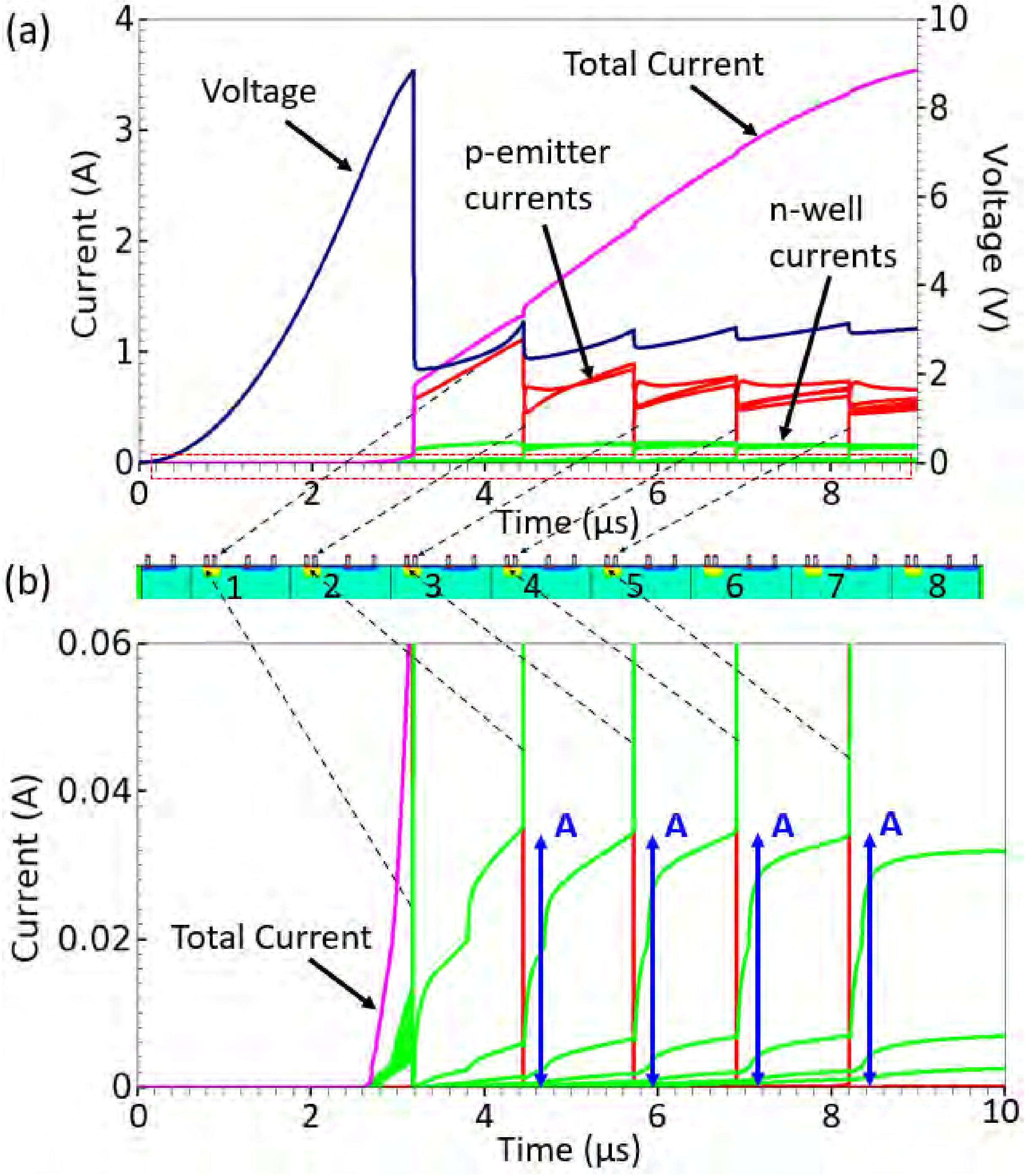

Figure 2.35: (a) Simulated p-emitter and n-well currents for the triggering in the difficult direction under the 42 V half sinusoidal pulse. (b) Enlarged current waveforms from (a) by zooming inside of the dashed rectangle. In (a) current and voltage waveforms are also given.

the n-well currents in the on-state, indicate the onset of SCR action. In this respect, it can be observed that SCR1 triggers first at $V_{TR} \sim 8.8$ V and then the inner fingers SCR2, SCR3, SCR4 and SCR5 trigger sequentially. There is no special reason for SCR1 to trigger first. Since all fingers are the same, the position of the first triggering finger is

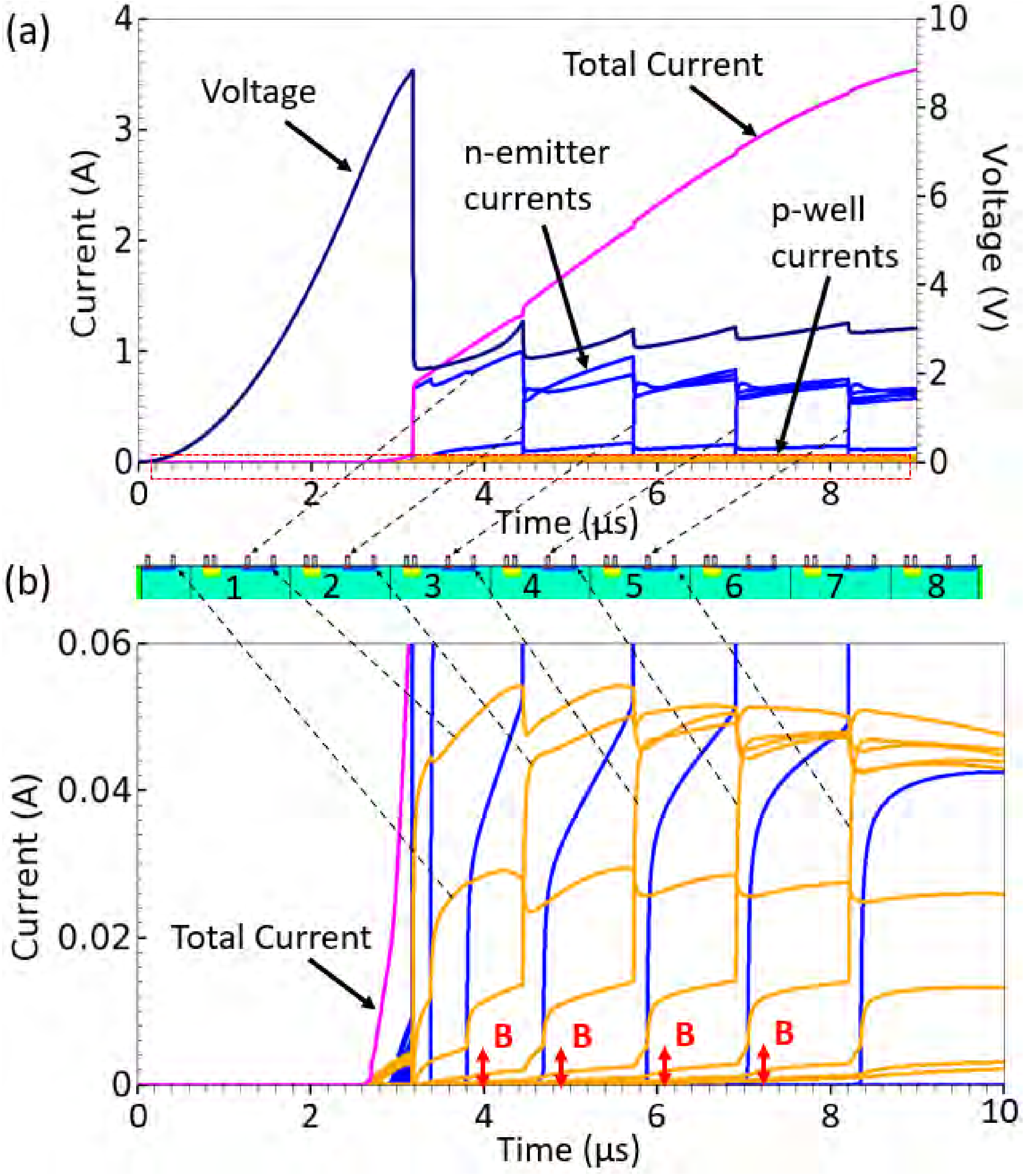

Figure 2.36: (a) Simulated n-emitter and p-well currents for the triggering in the difficult direction under the 42 V half sinusoidal pulse. (b) Enlarged current waveforms from (a) by zooming inside of the dashed rectangle. In (a) current and voltage waveforms are also given.

determined by the small fluctuations in the mesh. In the experimental structure this may be due to small variations from finger to finger. The inner fingers are activated near the holding voltage without impact ionization. In addition, with the triggering of each new finger a voltage drop occurs and the current density in the triggered fingers equalize. This equalization occurs by decreasing the current density in already triggered fingers while increasing in the newly triggered finger.

Since the current and voltage waveforms for the triggering in the easy direction under the 30 V half sinusoidal pulse are similar to what is shown in Figure 2.35 and Figure 2.36, we did not put the results for this simulation in order not to repeat the similar things. A significant difference between these two simulations is the direction of finger triggering. In simulations with 30 V half sinusoidal pulse, SCR8 is triggering first and the inner fingers SCR7, SCR6, ... until SCR3 are triggering. The the total current and the voltage waveforms for the latter; however, can be found in Figure 2.28 (d) and (e), respectively. As it can be observed in Figure 2.28, the simulated current and voltage waveforms are very well matched to the experimental results. If we compare experimental and simulation data for the current per triggered finger at the moment of the triggering of a new finger, a quite well matching is observed again as shown in Figure 2.29 (compare Simul.(Easy) and Exp. (Easy) curves in Figure 2.29).

2.2.4.4 Sequential finger triggering mechanism

Now we will go into detail and investigate the physical origin of the inter-finger coupling between the fingers, which appears at voltages well below V_{TR}, where there is no impact ionization. We will start our analysis with the triggering in the difficult direction.

2.2.4.4.1 Mechanism for triggering in the difficult direction For that purpose, we will consider the triggering of SCR3 after the triggering of SCR2. There is no special reason for this selection. For any other two neighbor fingers, which trigger sequentially, the mechanism is also the same. Figure 2.37 shows the simplified schematics for our consideration, which is based on the analysis of the 2D TCAD profiles of the total current density, hole current density and electron current density distributions. With the triggering of SCR2, holes are injected from the p-emitter and form the dominant lateral SCR path which is shown with the blue arrow Figure 2.37 (a). The supporting flow of electrons via n-well, on the other hand, is indicated with the red arrow. With these electrons and holes, the region below SCR2 is filled with an electron-hole plasma as shown with the dashed region in Figure 2.37 (b). While this is happening, the vertical pnp, which is shown with the vertical blue arrow in Figure 2.37 (c) becomes activated and causes further hole injection and their movement along the p-sub towards the n+-GND contact of SCR3. This hole current then forms the base current, $I_{b,npn}$, for the triggering of the npn transistor of SCR3. The situation can be schematically depicted with Figure 2.34. In that case, $R_{b,psub}$ denotes the p-sub resistance and the left and right SCRs correspond to SCR2 and SCR3, respectively. With the movement of holes, as shown with the dashed region in Figure 2.37 (d), part of the holes fills the region around the GND region of SCR3. Thus, some holes move through the $R_{p\text{-well}}$ resistance and help to forward bias the p-well/n+-GND junction (base/emitter junction of the npn of SCR3). When a sufficient voltage on the $R_{\text{p-well}}$ resistance is reached, the npn of SCR3 triggers. This is also the time point that ~5 mA difference between the p-well and n-emitter currents is reached as shown with arrow B in Figure 2.36 (b). The current inside of the n-well of SCR3 ($I_{c,npn}$); therefore, increases as shown with the right-side red arrow in Figure 2.37 (e). When the n-well current reaches a critical value, a certain voltage drop on the $R_{\text{n-well}}$ is reached and so the pnp of SCR3 triggers (see the right-side blue arrow in Figure 2.37 (f)). This is also the time point that ~35 mA difference shown with arrow A in Figure 2.35 (b) is reached between the n-well and p-emitter currents.

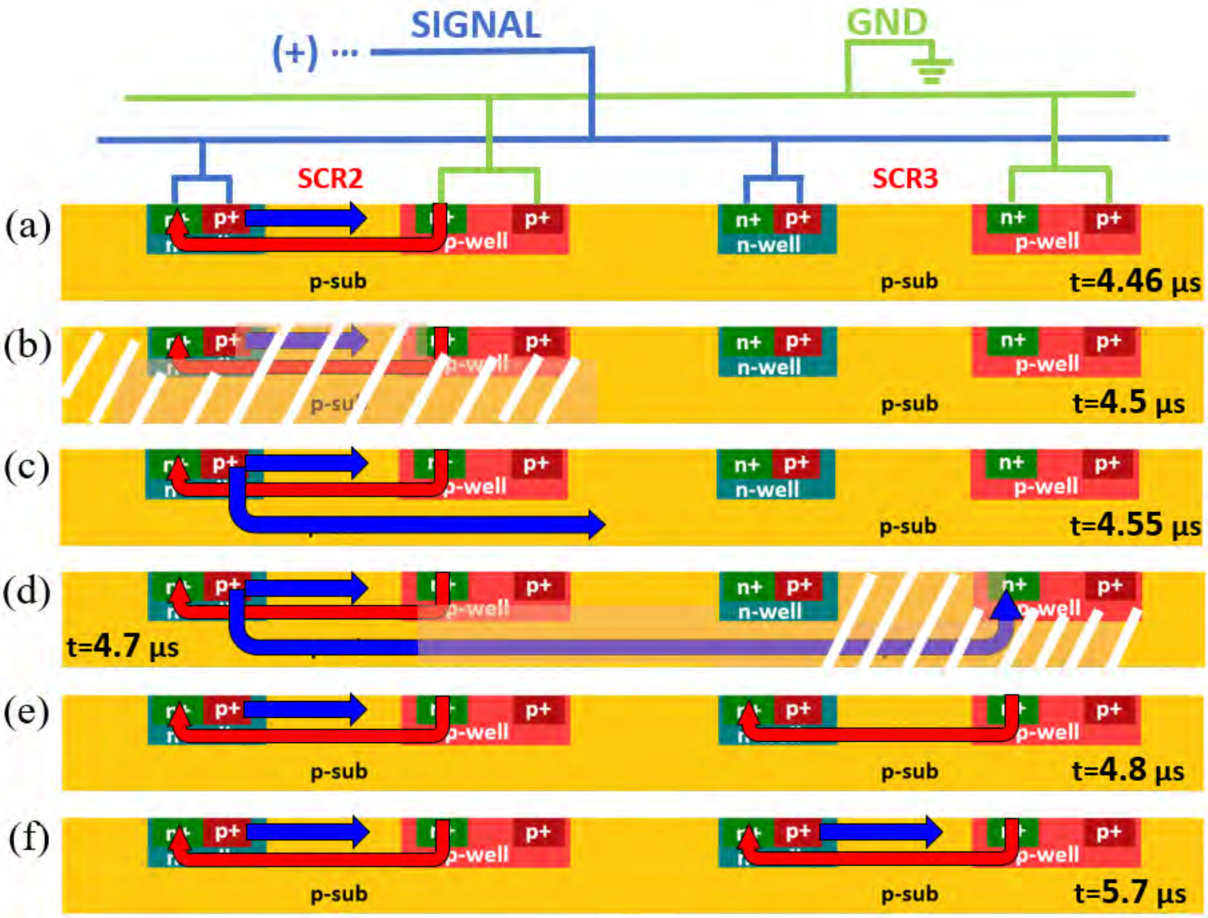

Figure 2.37: Schematics to explain the mechanism for triggering in the difficult direction (towards the right-side). The movement directions of electrons (red) and holes (blue) between the triggering of SCR2 and SCR3 are given: (a) the moment of triggering of SCR2, (b-c) are the moments before triggering of SCR3, (d) GND region of SCR3 is filled by holes, (e) triggering of the npn of SCR3, (f) triggering of pnp of SCR3 and so the triggering of SCR3. The indicated time moments are consistent with Figure 2.35 and Figure 2.36. The orientation of the arrows indicate the electron or hole flow vectors, not the corresponding electrical currents.

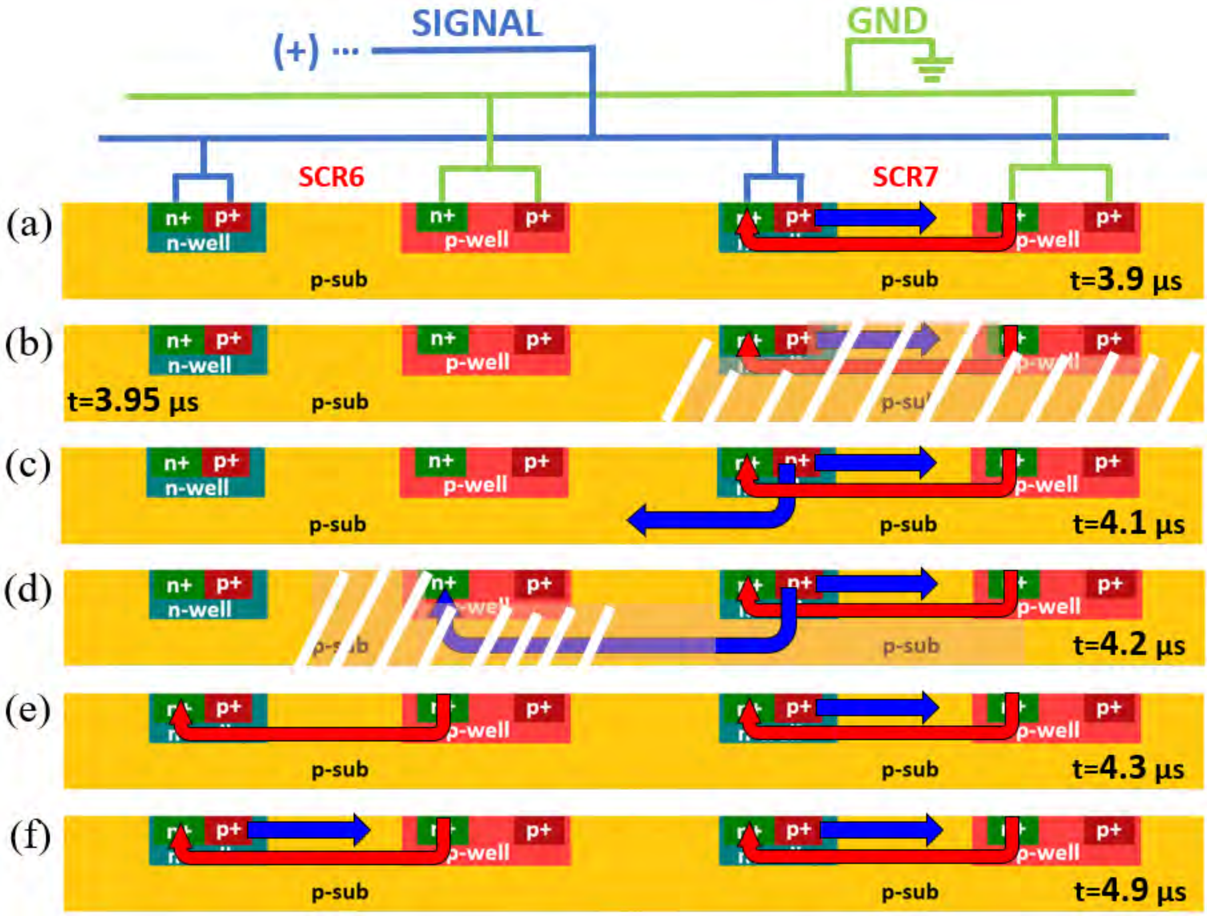

Figure 2.38: Schematics to explain the mechanism for triggering in the easy direction (towards the left-side). The movement directions of electrons (red) and holes (blue) between the triggering of SCR7 and SCR6 are given: (a) the moment of triggering of SCR7, (b-c) are the moments before triggering of SCR6, (d) GND region of SCR6 is filled by holes, (e) triggering of the npn of SCR6, (f) triggering of pnp of SCR6 and so the triggering of SCR6. The orientation of the arrows indicate the electron or hole flow vectors, not the corresponding electrical currents.

2.2.4.4.2 Mechanism for triggering in the easy direction After the explanation of the mechanism for triggering in the difficult direction (towards the right), one can deduce the mechanism for triggering in the in easy direction (towards the left). However, for completeness purposes, we will also explain it here. For that purpose, we will consider the triggering of SCR6 after triggering of SCR7. Again there is no special reason for this selection. Figure 2.38 shows the simplified schematics for our consideration. With the triggering of SCR7, holes are injected from the p-emitter and form the dominant lateral SCR path as shown with the blue arrow Figure 2.38 (a). The supporting flow of electrons via n-well, on the other hand, is indicated with the red arrow. With these electrons and holes, the region below SCR7 is filled with an electron-hole plasma as shown with the dashed region in Figure 2.38 (b). While this is happening, the vertical pnp, which is shown with the vertical/left blue arrow in Figure 2.38 (c) activates and causes further hole injection and their movement towards the n+-GND contact of SCR6 along the p-sub. This hole current then forms the base current, $I_{b,npn}$, for the triggering of the npn transistor of SCR6. The situation can be schematically depicted with Figure 2.34. In that case, $R_{b,psub}$ denotes the p-sub resistance and the left and right SCRs correspond to SCR7 and SCR6, respectively. Part of the holes fill the region around the GND region of SCR6 as shown with the dashed region in Figure 2.38 (d). Thus, some holes move through the $R_{p\text{-well}}$ resistance and help to forward bias the p-well/n+-GND junction (base/emitter junction of the npn of SCR6). When a sufficient voltage on the $R_{p\text{-well}}$ resistance is reached, the npn of SCR6 triggers. The current inside of the n-well of SCR6 ($I_{c,npn}$); therefore, increases as shown with the left-side red arrow in Figure 2.38 (e). When the n-well current reaches a critical value, a certain voltage drop on the $R_{n\text{-well}}$ is achieved and so the pnp of SCR6 triggers (see the left-side blue arrow in Figure 2.38 (f)).

So at that point we come to the most crucial question of this section: Although their mechanisms are similar, why is there easy and difficult triggering directions? Why for the triggering in the easy direction less amount of current is required to apply at the triggering of a new finger (see Figure 2.29)? The answer to all these questions is the geometry of the device. As it can be observed, the sequential finger triggering (SFT) in our structure is determined by the movement of holes. Therefore, once a finger triggers, which neighbor finger will trigger next depends on how much hole moves to bias their p-well/n+-GND junctions. In our structure, the p-well/n+-GND junction of the non-triggered neighbor finger on the left side is closer to the p+-SIGNAL contact of the triggered finger, compared to that on the right side (see Figure 2.37 or Figure 2.38). Therefore, once a finger triggers it takes less amount of time for holes to bias the p-well/n+-GND junction of fingers at the left side and so fingers trigger towards the left side easier. With the same logic, a smaller amount of applied current becomes sufficient to trigger fingers towards the left side compared to triggering of fingers towards right side.

2.2.4.5 The ratio of p-emitter current moving to the right and left sides of a finger after triggering

During simulations, it took our attention that after the triggering of a finger some part of its p-emitter current was going to the ground (GND) of the neighbor finger at left instead of its own ground. To exemplify, for the triggering in difficult direction (towards the right) under the 42 V half sinusoidal pulse, some part of the p-emitter current of SCR3 and SCR2 was going to the GND of SCR2 and SCR1, respectively. Therefore, to investigate how much of the p-emitter current goes to the left and right sides of the signal contacts after triggering, we extracted the total current densities around the signal contacts of SCR2 and SCR3 through the lines A and B at $t = 8.5$ µs as shown in Figure 2.39 (a) and (b). At $t = 8.5$ µs, all of the fingers from SCR1 to SCR5 already triggers, and no new finger triggering occurs (see Figure 2.28, 2.25 and 2.36) later. The analysis revealed that for both fingers 78% and 22% of the total p-emitter current is going towards the right and left sides of the signal contacts of the fingers. The majority of the p-emitter currents which move towards right, goes to the ground of the finger itself whereas majority of the holes which moves towards left, goes to the ground of the finger at left. We are saying majority because some negligible part of holes moves towards the other fingers and the deeper regions of the silicon layer.

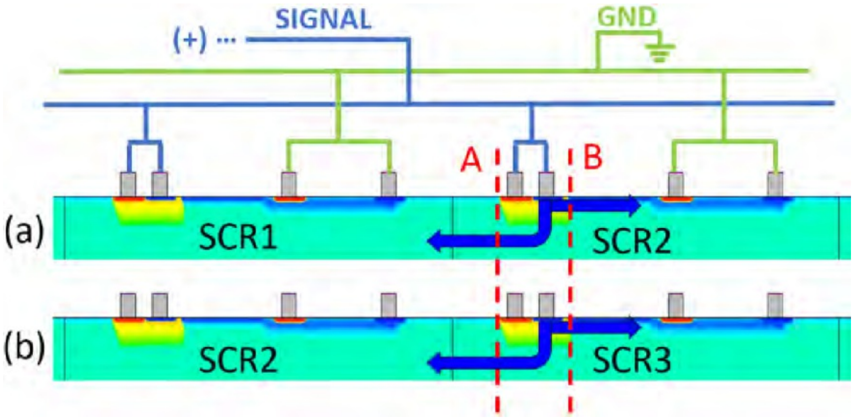

Figure 2.39: The total current densities around the signal contacts of (a) SCR2 and (b) SCR3 through the lines A and B are extracted at t = 8.5 µs

2.2.4.6 Effect of trigger tap on trigger delay

As it is presented in Figure 2.30, all of the fingers in our 8-finger simulation structure has the trigger tap (TT). Therefore, in order to understand the effect of TT on finger triggering, we put TT just on the SCR1 and removed it from the other fingers as shown in Figure 2.40. Since SCR1 has TT, it triggered first and so other fingers triggered sequentially in the difficult triggering direction (towards the right). During our analysis, it turned out that compared to the simulations with structure which have TT at all fingers, the fingers in this new structure was triggering at a smaller applied current value and so the current per triggered finger at the triggering moment of the new fingers was becoming smaller. Figure 2.41 shows this comparison. The reason for this behavior is the attraction effect of TT. We are running here a 2D simulation and so the simulation solver is assuming a TT through all over the device width. Therefore, since TT is p-doped, the holes moving from a triggered finger to the non-triggered neighbor finger are heavily attracted by the low resistivity of TT (There is also a higher valence band energy at that part of the silicon to attract the holes). Due to this attraction, more amount of holes are needed to move through the $R_{\text{p-well}}$ resistance to bias the base-emitter junction of the npn transistor. More amount of holes; therefore, requires more current to be applied. In this respect, when we remove TTs, we also eliminate the attraction effect for the holes and so they bias the next finger at smaller applied current values.

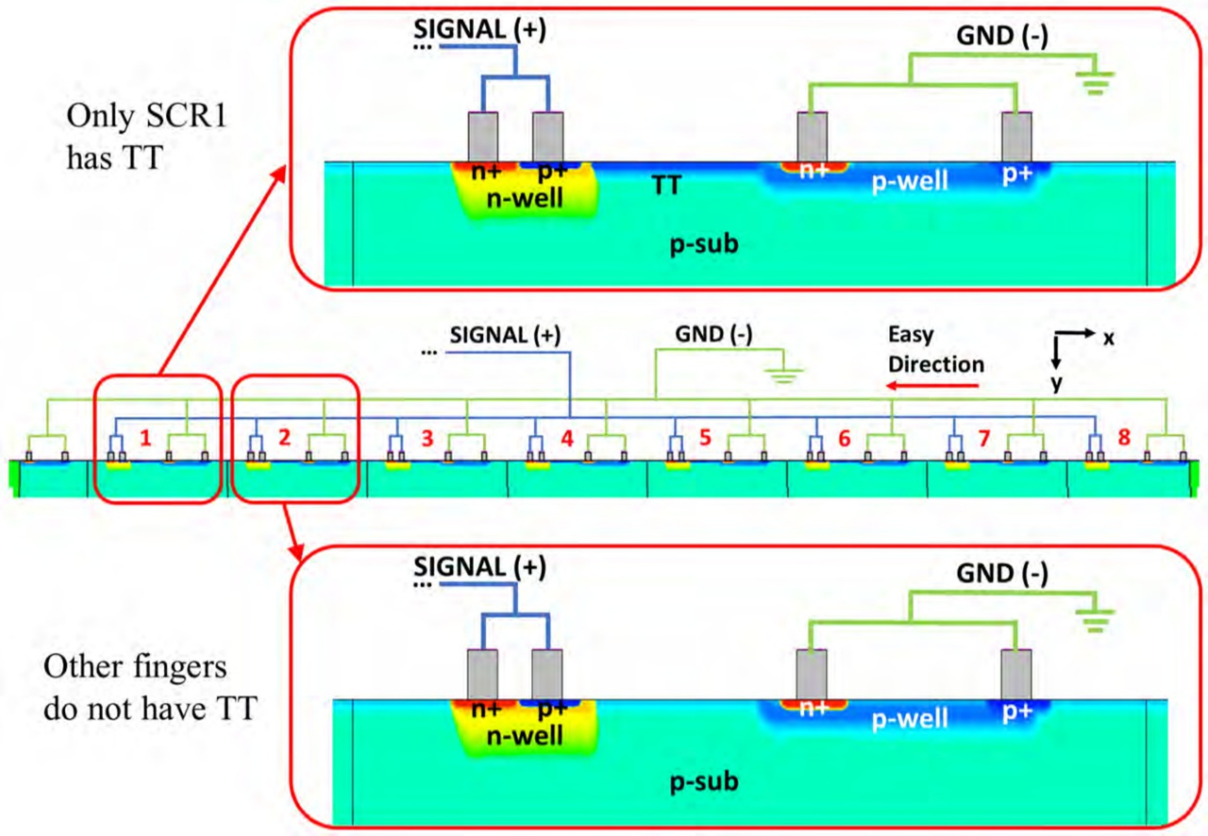

Figure 2.40: The simulation structure which has TT only on SCR1.

2.2.4.7 Effect of a missing finger on triggering behavior

We also wanted to find an answer for the question of what happens if we remove one of the fingers from the simulation structure. For that purpose, at the simulations which show finger triggering in the difficult direction, SCR3 and SCR4 are separately removed as shown in Figure 2.42 (a) and (b). In these new simulations, SCR1 triggered first also. However, for the structure shown in Figure 2.42 (a), only SCR1 and SCR2 triggered whereas for the structure in Figure 2.42 (b) only SCR1, SCR2 and SCR3 triggered. In the original structure which has no missing finger, on the other hand, SCR1, SCR2 and alternately up to SCR5 was triggering sequentially. If we plot the maximum device temperatures as shown in Figure 2.43, on the other hand, it turned out that the temperature value was reaching very high values after the triggering of SCR2 and SCR3 for the simulations of structures shown in Figure 2.42 (a) and (b), respectively. So this means that when a finger is missing, before the triggering of the finger at the right side of the missing finger, the temperature in the triggered fingers was rising too much due to the self-heating effect and so causing the thermal runaway. The triggering time of fingers, on the other hand,

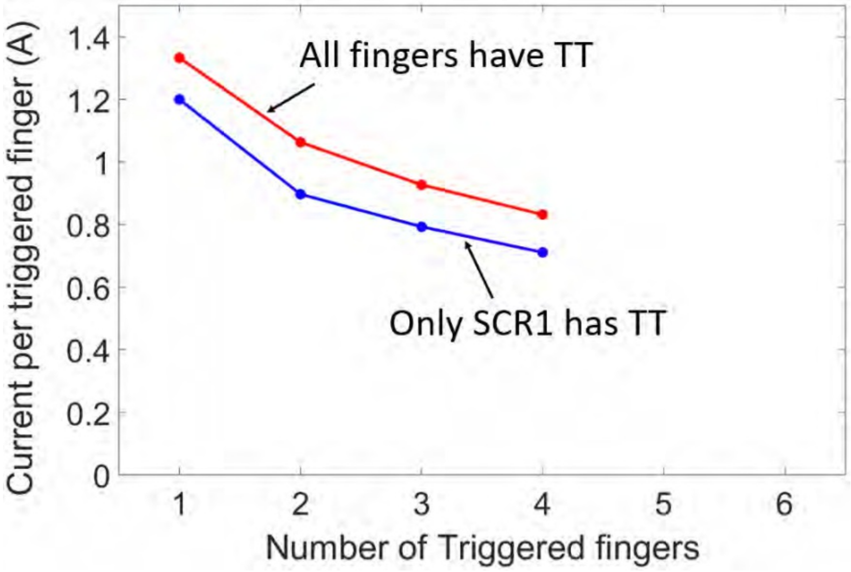

Figure 2.41: Comparison of the current per triggered finger values at the moment of the triggering of a new finger for the simulation structure which have TT at all fingers and the simulation structure which have TT only on SCR1.

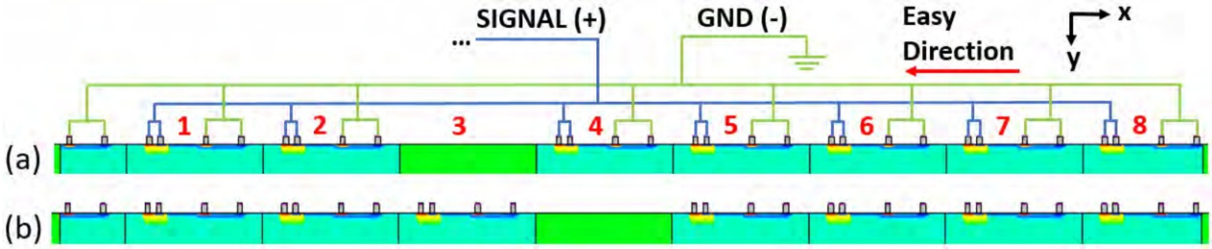

Figure 2.42: The simulation structure with missing (a) SCR3 and (b) SCR4

nearly do not change between simulations for the triggered fingers.

In conclusion, although a sequential finger triggering mechanism was observed in chapter 2.1 under HBM-like TLP stresses with RT = 10 ns and in chapter 2.2 under Surge-like half sinusoidal pulses, the triggering behaviour was slightly different due to geometry of the devices. While for the device in chapter 2.1, the holes produced by the impact ionization in the inactive outer fingers were helping the outer fingers to trigger first, due to nonexistence of a finger like that, the position of first triggered finger was changing from device to device for devices in chapter 2.2. However, the geometry was showing its impact on the devices in chapter 2.2 after the first triggering. Although the triggering of devices in chapter 2.1 was always in one direction, which is from outer fingers into inner fingers, for devices in chapter 2.2, there were two options: towards left or right sides. The triggering towards the left side was more preferable. However, triggering towards the right side was also possible. All fingers, nevertheless, were triggering once a

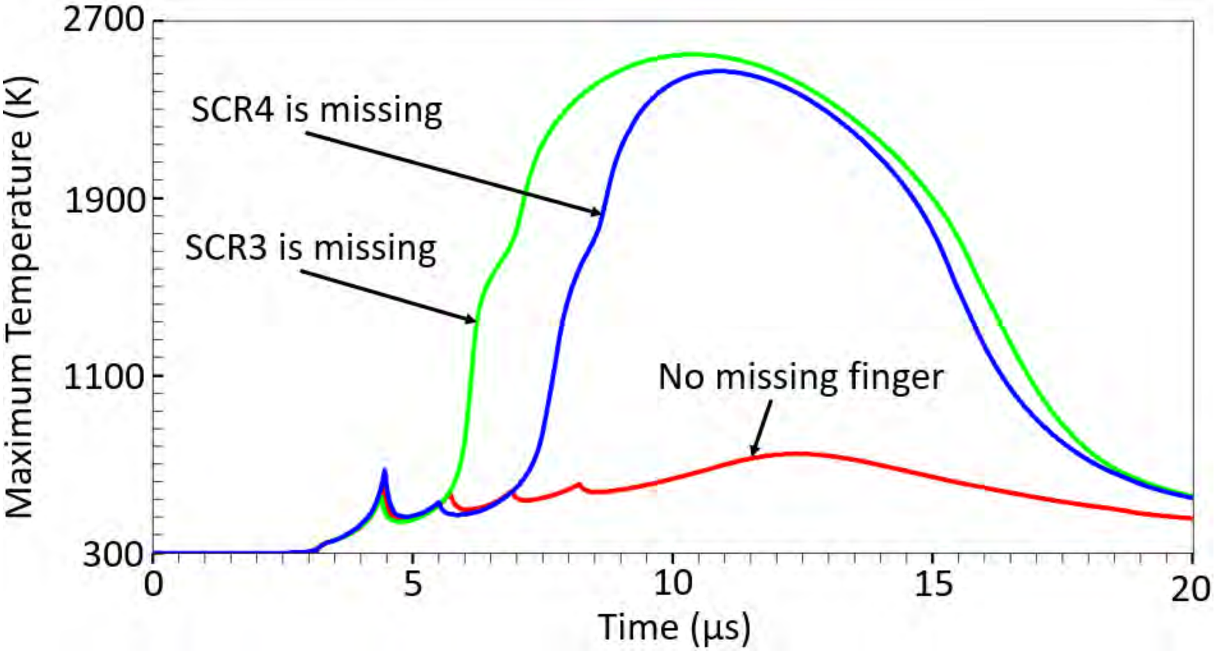

Figure 2.43: Comparison of maximum device temperature values for the simulation structures of has no missing finger, SR3 is missing and SCR4 is missing.

certain current, which is peculiar to the investigated device, on the n-well resistance is reached.

In addition to that since the duration of pulse width for HBM-like TLP stress is in the nanosecond range, the lateral distance between the neighboring fingers of the investigated device in chapter 2.1 was becoming larger than the thermal diffusion length determined by the trigger delay. In this respect, the self-heating effect was not needed to be included in the simulations and so an isothermal drift-diffusion simulation model instead of a thermodynamic model became sufficient to reveal the correct device behaviour. In this respect, we got rid of the time consumption due to solving of complex thermal equations. As for Surge-like half sinusoidal pulse in chapter 2.2, on the other hand, since the pulse width duration is in the microsecond range, the self heating effect was needed to be included and so simulations with thermodynamic model were conducted.

Chapter 3

Filamentary States in SCRs

Silicon Controlled Rectifiers (SCRs) are popular devices for electrostatic discharge (ESD) protection due to their high ESD robustness [6, 11, 13]. Discrete devices on low-doped or silicon on insulator (SOI) substrate, for instance, are often used for system-level ESD protection due to their low capacitance and high failure current I_{t2} [6, 7, 13–16]. The low capacitance of SCRs makes them suitable for high-frequency or large bit-rate applications such as USB3 and Thunderbolt [6, 7]. For latch-up safe operations, in addition, high holding voltage, V_{HOLD}, and high holding current, I_{HOLD}, are often requested [39, 40]. Although V_{HOLD} has been studied extensively [40, 74], there is less literature related to optimization of I_{HOLD} [79, 92, 93]. Moreover, the previous design measures to increase I_{HOLD} have been conducted by 2D technology computer-aided design (TCAD) simulations [79, 92].

I_{HOLD} is basically the smallest current in the SCR on-state. However, the position of it on the IV curve exhibits a non-trivial dependence on the device width, depending on whether a current filament (CF) [26] is created or not. In small width devices, current flows homogeneously along the device width [38] and a CF (i.e. inhomogeneous current density distribution over the device width) does not form. I_{HOLD}; therefore, is determined as the current in the SCR on-state where the lowest voltage value [94, 95] on the IV curve of the device occurs [26, 38]. In sufficiently wide structures; however, due to negative differential resistance (NDR)–induced instability [27–30], current flow along the device width becomes inhomogeneous [26] and so a CF emerges [26, 28–32, 34, 35, 56, 96]. The resulting filamentary IV curve; thus, becomes quite complex and, as it has also been observed experimentally in power thyristors [33, 34, 97] and ESD protection devices [7, 18, 26, 70, 94, 98–102], typically exhibits a double-hysteresis behavior. The origin of this double-hysteresis IV behavior is comprehensively explained in the introductory part of [26]. I_{HOLD}, in this case, is determined as the current value where the smallest possible CF occurs while the self-sustaining SCR action takes place. Since the existence of CF is dependent on the device width and the conventional 2D TCAD simulations always assume a homogeneous current distribution along the device width, 2D TCAD simulations, in principle, cannot treat this phenomenon [103, 104]. 3D TCAD simulations are needed instead. The values of I_{HOLD} and V_{HOLD}; thus, can be different, depending on whether they are calculated by 2D or 3D TCAD.

Besides that, although there exist some theoretical approaches about how to qualitatively model the filamentary IV curves in simple structures with 1D doping profile extended in the width direction [33, 34], the ESD protection devices typically have a complex 2D cross section and so the analytical analysis would be difficult or even impossible to perform. A 3D TCAD analysis of grounded-gate MOSFETs, for instance, has demonstrated differences between the IV curves calculated by 3D and 2D TCAD simulations [94, 103].

In this respect, we present a 3D TCAD methodology to investigate the CF-related double-hysteresis filamentary IV behavior and its related I_{HOLD} value in sufficiently wide structures which cannot be observed in 2D TCAD simulations. For this purpose, we apply quasi-DC up and down current sweeps to the 3D TCAD simulation structures of single-finger ESD protection SCRs to reveal their IV characteristics, and determine the smallest current from the down sweep IV characteristics, where the SCR is still in the on-state, as I_{HOLD}. This novel methodology has practical relevance for protection design and excludes 2D TCAD as a tool for reliable I_{HOLD} estimation. To our knowledge, previously, the double-hysteresis behavior has not been simulated in ESD protection devices, and 3D TCAD has not been applied to I_{HOLD} analysis. All of the simulations are conducted with TCAD from Synopsys Sentaurus [105].

In the experiments, on the other hand, up and down DC current sweeps are applied by using the Keithley 2410 Source Measurement Unit (SMU) or HP 4155A Semiconductor Parameter Analyzer in the current controlled-mode and the resulting double-hysteresis DC IV curve is recorded. To monitor the current distribution over the device width as a function of total current, in addition, emission microscopy (EMMI) [20, 70, 106] is conducted simultaneously with IV recording. The EMMI pattern is recorded from the polished backside of the chip by an InGaAs Focal Plane Array (FPA) Infrared camera [7] as discussed in section 1.5.3.

3.1 EMMI results for multifinger devices

Although in this chapter we investigate the single-finger SCR structures in detail, what complicates the matters even more during the application of this methodology is the fact that ESD protections are usually laid out as multi-finger devices [19, 70]. The IV curves of multi-finger devices show multiple branches instead of a double-hysteresis behavior [7, 107, 108]. Figure 3.1 (a), for instance, shows the background infrared (IR) reflectivity image of an 8-finger SCR with three segments per finger separated by trigger taps (TTs). There are; therefore, 24 segments in total. The IV curve for this device, on the other hand, is presented in Figure 3.1 (b). It is obtained by sweeping up and down the current and the red arrows in Figure 3.1 (b) indicate the sweeping direction. During the sweeping, with the triggering or turn off of each new segment pair, which shares the same ground, a voltage jump on the IV curve occurs. If a few segment pairs trigger or turn off together, on the other hand, the voltage jump becomes bigger. In order to help the reader to understand finger triggering, Figure 3.2 presents the EMMI images, aligned with the backside reflectivity image of the device in Figure 3.1 (a), at some selected points on the IV curve. The number of triggered segments, N, is also shown on top of the EMMI images.

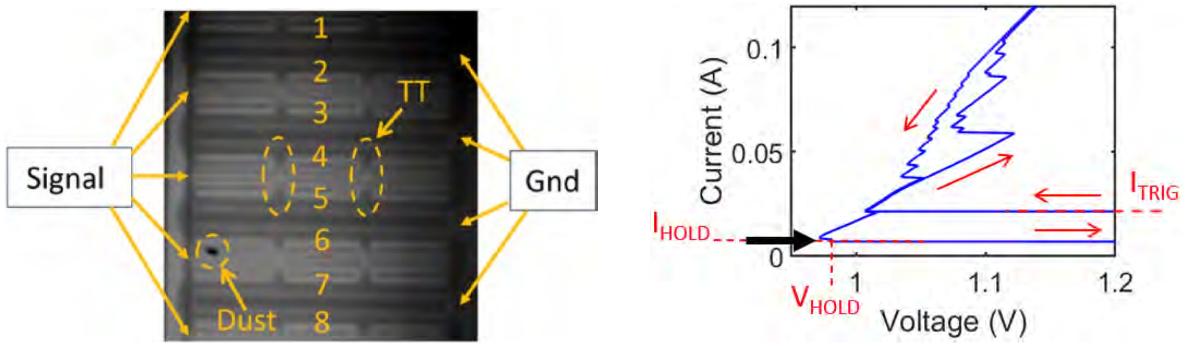

(a)

(b)

Figure 3.1: (a) The background infrared (IR) reflectivity image of an 8-finger SCR with three segments per finger separated by trigger taps (TTs). (b) The IV curve for the device in (a). The arrows in (b) indicate the sweeping direction of the current.

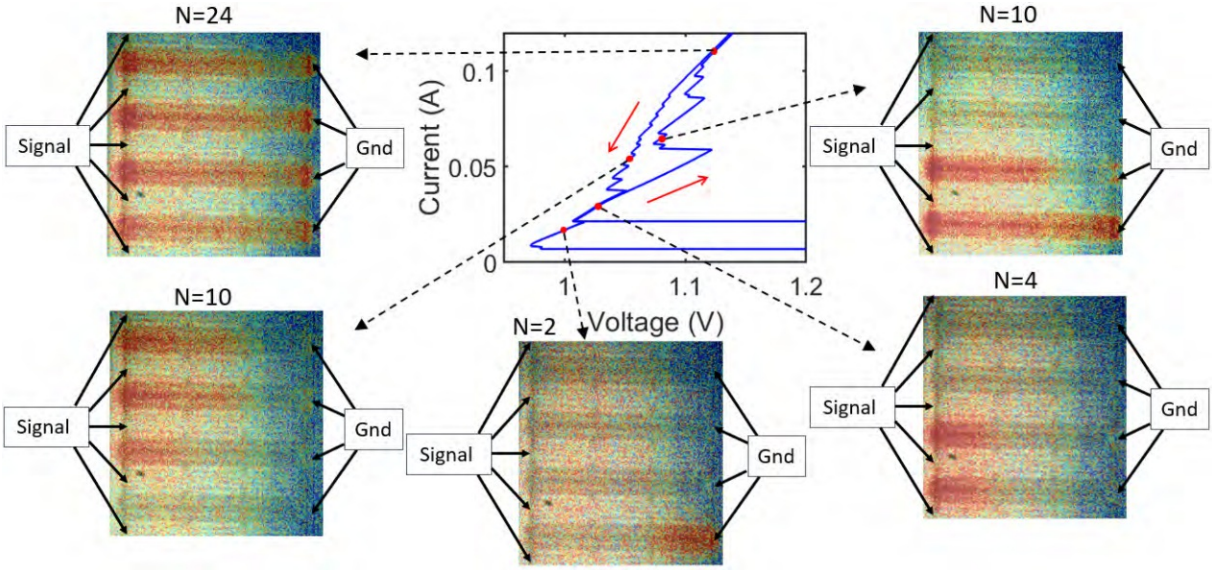

Figure 3.2: EMMI images at some selected points on the IV curve in Figure 3.1 (b) to help reader to understand the finger triggering in multi-finger SCR structure shown in Figure 3.1 (a). The number of triggered segments, N, is shown on top of the EMMI images.

If we compare the IV curves of multi-finger devices with that of single-finger devices further, it turns out that although the trigger current, I_{TR}, scales with the total device width, the holding current I_{HOLD} is determined by the activity of the last triggered finger/segment when sweeping down the current [7, 107]. In Figure 3.1 (b), for instance, although there are 12 segment pairs, which shares the same ground, there are 13 jumps in total when sweeping the current down. This is because the current flows through only one segment instead of a segment pair around $I = I_{HOLD}$ and so an extra jump in the voltage emerges. The black thick arrow in Figure 3.1 (b) shows the position of this extra jump on the IV curve. Therefore, it is the behavior of a single finger/segment that determines I_{HOLD}. Figure 3.3 (a) and (b), on the other hand, compares I_{HOLD} if we sweep the current up and down multiple times on the device in Figure 3.1 (a). The IV curves in Figure 3.1 (b) and Figure 3.3 (a) are the same. The current in Figure 3.3 (a) is swiped up and down one time whereas that is two times in Figure 3.3 (b). The red arrows indicate the sweeping direction. The related EMMI images, aligned with the backside reflectivity image of the device, are also given for some selected points on the IV curve with total number of triggered segments, N, together. As it can seen, although different emission patterns occur at different sweeps, the same I_{HOLD} is observed every time. This is because I_{HOLD} is independent from position of the last active finger/segment. In addition to that in Figure 3.3 (b) there are again 13 jumps in total when sweeping down the current.

Figure 3.4 presents the measured current density per triggered segment (I/N) as current rises for the IV curve shown in Figure 3.2 and Figure 3.3 (a). The number of triggered segments, N, is also shown. N = 24 label at low current density values shows the current conduction just on npn before the triggering of any finger/segment. As it can be observed, nearly the same current density exists at the triggering of each neighbor segment. As for mechanism of triggering, on the other hand, the device triggers due to substrate coupling of fingers/segments. In this respect, the triggering mechanism shows a similarity to sequential finger triggering (SFT) mechanism discussed in chapter 2.

The analysis of I_{HOLD} in a different type of multi-finger device and its related EMMI images that support our argument that I_{HOLD} is determined by the last active finger/segment can be found in [7].

3.2 Single finger devices under study

Figure 3.5 (a) and (b) show the simplified cross section view and the top view of the studied single-finger SCRs, respectively. The structures are fabricated on lightly p-doped silicon on an insulated substrate (BOX). The shallow p+, n-well and deep p-well under the Signal terminal serve as emitter (E), base (B) and collector (C) of the pnp transistor, respectively. The n-well, in addition, serves as a substrate resistance of the pnp. The highly doped n+-region of the Ground terminal, p-substrate/deep p-well and n-well, on

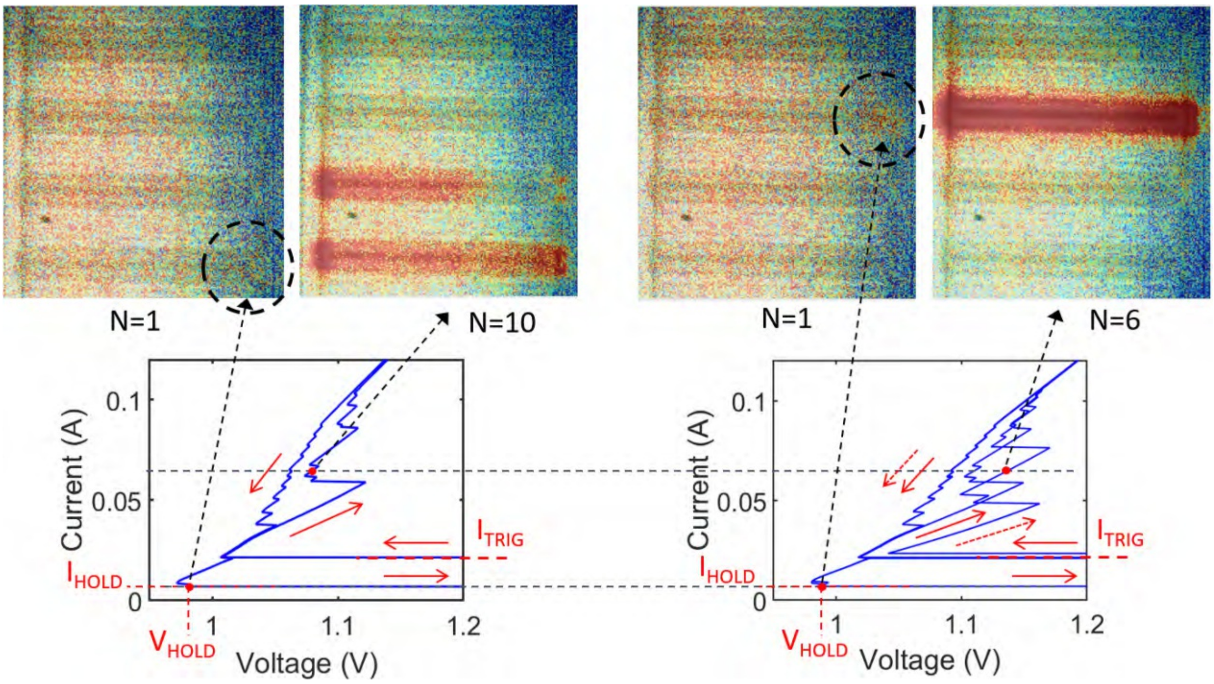

Figure 3.3: IV curves to show what happens I_{HOLD} if we sweep the current up and down multiple times on the device in Figure 3.1 (a). In (a) and (b) the current is swiped one and two times, respectively. The related EMMI images at some selected points on the IV curve are also given with total number of triggered segments, N. The red arrows indicate the sweeping direction.

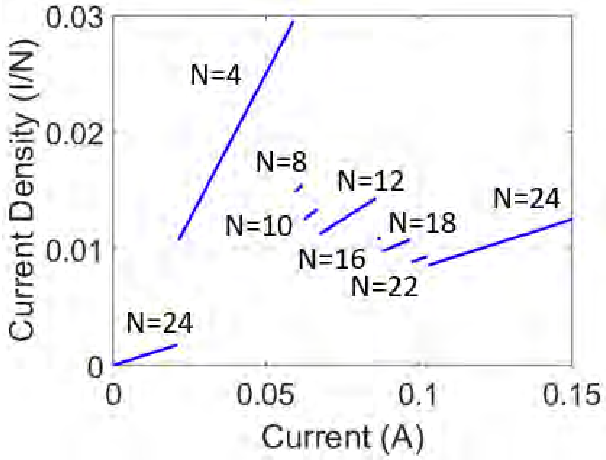

Figure 3.4: Tthe measured current density per triggered segment (I/N) as current rises for the IV curve shown in Figure 3.2 and Figure 3.3 (a). The number of triggered segments, N, is also shown.

the other hand, form the E, B and C regions of the npn, respectively. The n+ contact to the n-well is short-circuited with the p+-emitter by metallization and the DC sweeping current is applied on them. The contact on n+-emitter, on the other hand, provides the ground connection. Since the p-substrate and the deep p-well are left floating, we call this device as floating-base SCR. Devices with different widths W (31.3 µm, 62.2 µm, 93.1 µm, 124 µm, 154.9 µm and 185.8 µm) and the layout parameter L were investigated. The default value of L will be denoted as L_0 in the further subjects.

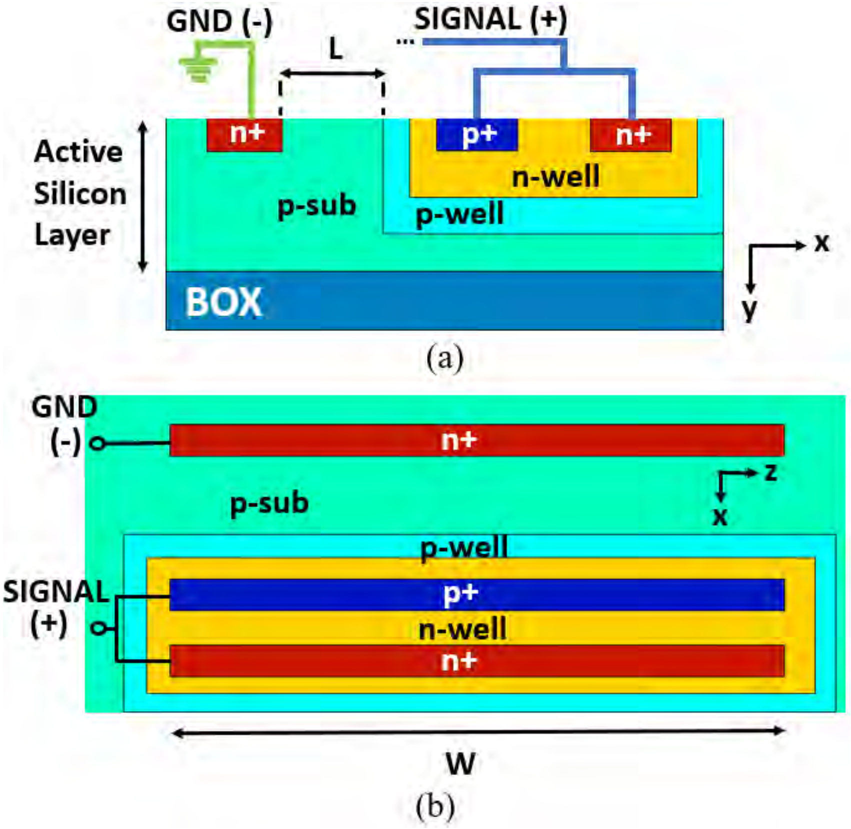

Figure 3.5: (a) The simplified cross section view of the studied single-finger SCRs. (b) The top view of the layout. Some layout parameters are also indicated.

3.3 Experimental results

3.3.1 DC IV with EMMI measurements

Figure 3.6 (a) and (b) show the experimental DC IV curve, recorded during the up and down current sweeping on a single-finger device with standard layout parameters and width of W = 124 µm, in full and zoomed scales, respectively. As it can be observed, the IV curve exhibits a double hysteresis behavior. Although the lower hysteresis is well pronounced, the upper one (see encircled region Figure 3.6 (a)) might be overlooked in the scale of Figure 3.6 (a). The points A-K indicate the device states at which EMMI images in Figure 3.7 are recorded. All of the EMMI images in Figure 3.7 are aligned with the backside reflectivity image of the device. In addition to that in Figure 3.6 (a) and (b), on-state, off-state and filamentary parts of the IV curve are indicated. One can also notice in Figure 3.6 (a) that , there exists a small voltage peak around V = 7.5 V (labeled V_{npn}) at low currents below 100 µA. This is due to avalanche and snapping-back of the open base npn.

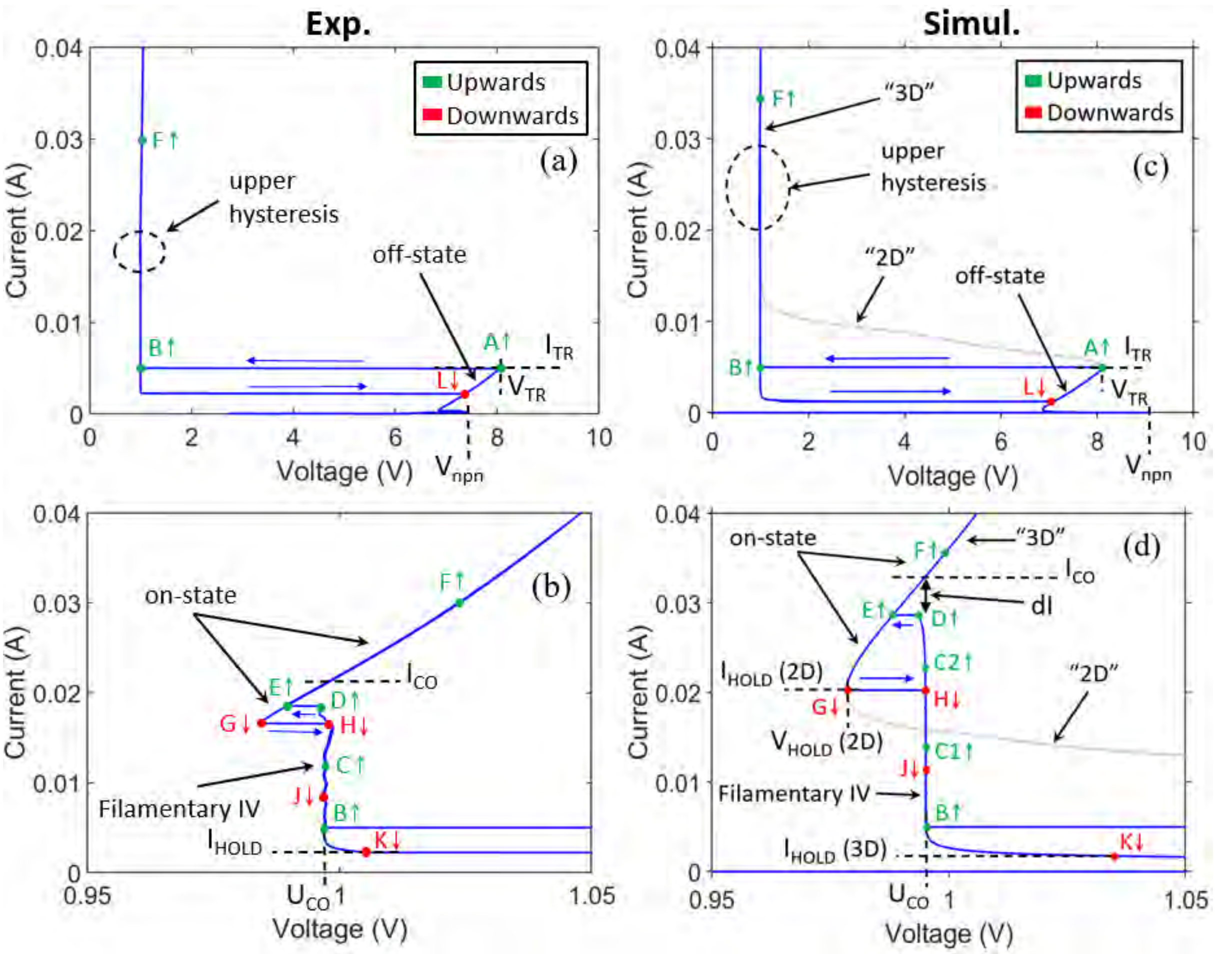

Figure 3.6: (a) Overall and (b) zoomed view of the experimental IV curve for a device with standard layout parameters and W = 124 µm. The points A-K indicate the device state at which EMMI images in Figure 3.7 are recorded. (c) Full and (d) zoomed scale view of the simulated 3D IV characteristics (curve "3D") for a simulation structure with standard layout parameters and W = 124 µm. The labels A-K indicate the working points at which J(z) distribution is extracted in Figure 3.16. Curve "2D" in (c) and (d), in addition, represents the 2D IV behavior with the homogeneous current flow. The current sweeping direction is indicated by arrows and color. The points in (a, b) and (c, d) are labeled identically according to the same qualitative behavior. However, the exact values of current and voltage can slightly differ. On-state, off-state and filamentary parts of the IV curve are also indicated.

During the increase of the total current from zero to trigger current I_{TR}, SCR remains in the off-state and the current flows homogeneously over the entire device width as can be seen in the EMMI image in Figure 3.7 (A). When the current reaches $I = I_{TR} \approx 5$

mA; however, the device is driven into the negative differential resistance (NDR) region and so a voltage snap-back occurs (see point B in Figure 3.6 (a) and (b)). Then, since the experimental device is sufficiently wide ($W \geq 62.2$ µm, this will be discussed later in detail), a CF develops and this results in the vertical or filamentary IV curve at the so-called coexistence voltage, U_{CO}, [26, 33] (see Figure 3.6 (b)). The related emission pattern is shown in Figure 3.7 (B). The width of this initial current filament, on the other hand, is $W_{CF} = 29$ µm and it is consistent with its estimation from I_{TR}/J_{CO}, where $J_{CO} = I_{CO}/W = 21.3$ mA/124 µm ≈ 0.17 mA/µm. J_{CO} is called as the one-dimensional current density and its value is independent from the applied sweeping current along the filamentary IV branch [26]. In other words, the value of J_{CO} in this experiment remains constant as 0.17 mA/µm all over the filamentary IV curve. In addition, on the filamentary IV branch, since there exists an inhomogeneous current distribution, the on-state region with the high current density $J_{CO} = I_{CO}/W$ (i.e. inside of the CF) coexists with a low current density (i.e. off-state) elsewhere [26, 38]. If we move further on the filamentary IV curve by ramping up the current, on the other hand, we reach point C (see Figure 3.6 (b)). Figure 3.7 (C); therefore, shows us that width of CF, W_{CF}, increases with increasing current I, according to:

$$W_{CF} \approx \frac{I}{J_{CO}} \tag{3.1}$$

Once we reach point D (see Figure 3.6 (b)); however, the inhomogeneous filamentary state becomes unstable and so the current conduction reverts back to a homogeneous state. The voltage; therefore, jumps to point E (see Figure 3.6 (b)). Figure 3.7 (D) and (E) show the related EMMI images at point D and E, respectively. Above point E the current flows homogeneously as shown in Figure 3.7 (F). When the current decreases, moreover, the homogeneous current distribution still stays stable until the point G (see Figure 3.7 (G)). Below point G; however, the device enters the NDR region again and a CF is created. Hence, the voltage jumps to point H (see Figure 3.6 (b)) on the filamentary IV curve. The pronounced filamentary state for point H can be seen in Figure 3.7 (H). With the further reduction of current, on the other hand, W_{CF} decreases until point K (see Figure 3.6 (b)) in accordance with Equation 3.1, as shown in Figure 3.7 (J). At point K, finally, the lowest current where the SCR still operates in the on-state, i.e. I_{HOLD}, is reached. It is also here better to emphasize that this is the I_{HOLD} value that has to be considered in latch-up considerations. Below point K, the self-sustaining operation of SCR in the CF is not possible anymore and so the current flows again homogeneously (see point L in Figure 3.6 (a)).

3.3.2 The way we measure plays a role

During our measurements we recognized that the way we measure plays a role on the IV curve results we get. Although the IV curves that we obtain with HP 4155A Semicon-

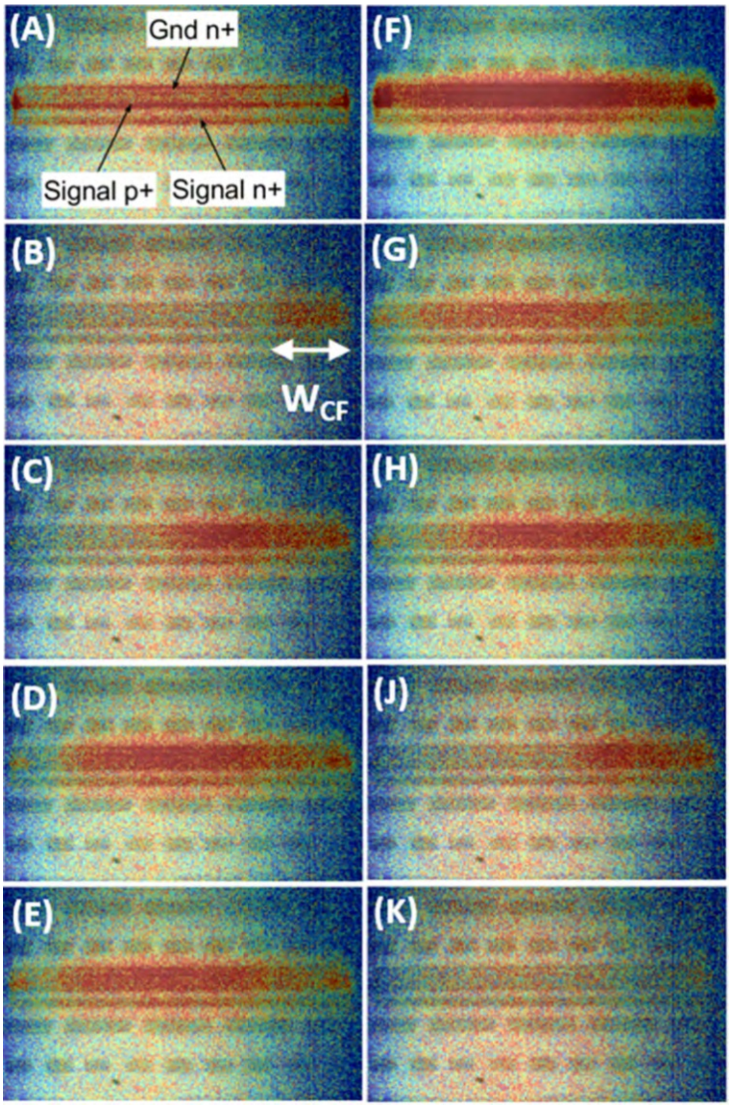

Figure 3.7: EMMI images at the working points A-K in Figure 3.6 (a) and (b). All images are aligned with the backside reflectivity image of the device. In B, the current filament width W_{CF} is also indicated.

ductor Parameter Analyzer in sufficiently long width devices (W ≥ 62.2 µm, this will be clear later) exhibits a double hysteresis behavior like in Figure 3.6 (a) and (b), once we remeasure the same experimental device with Keithley 2410 Source Measurement Unit (SMU), serious oscillations due to parasitic elements (L,C) in the measurement chain were observed. Figure 3.8 (a) and (b), for instance, compares the experimental IV curves for the same device, which has the standard layout parameters and width of W = 93.1 µm, from Keithley 2410 SMU and HP 4155A Semiconductor Parameter Analyzer, respectively. When we used TDK ZCAT ferrite beads on the measurement cables, on the other hand, the oscillations that we observed in Figure 3.8 (a) were damped in devices with W ≥ 62.2 µm while they continued in small width devices like W = 31.3 µm. After damping out the oscillations; therefore, the IV curves with Keithley 2410 Source Measurement Unit (SMU) also showed a double hysteresis behavior for devices with W ≥ 62.2 µm like in Figure 3.6 (a) and (b).

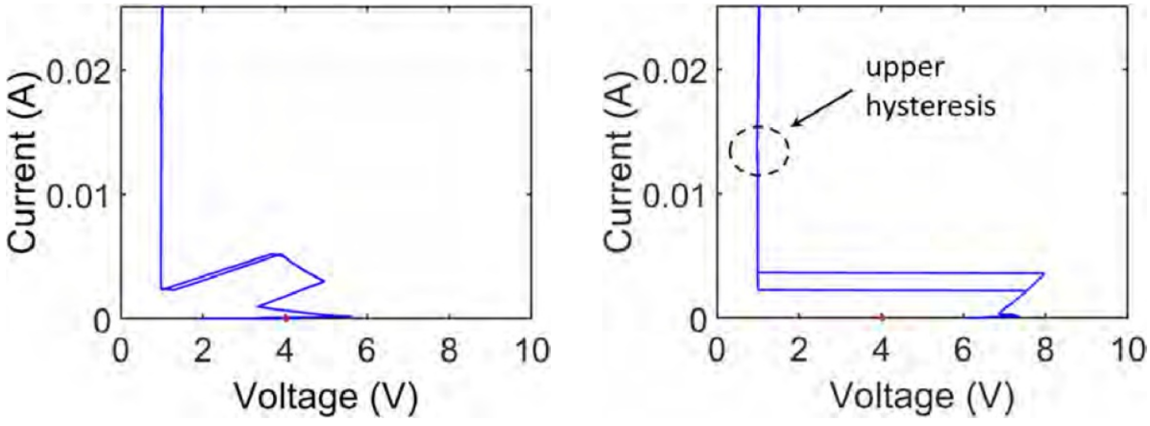

(a) (b)

Figure 3.8: The experimental IV curves for a device, with W = 93.1 µm and the standard layout parameters, from (a) Keithley 2410 Source Measurement Unit (SMU) and (b) HP 4155A Semiconductor Parameter Analyzer.

3.4 TCAD simulation approach

Figure 3.9 (a) and (b) presents the layouts of the 3D simulation structures of the single-finger SCRs that we used to investigate the current density distribution and IV curves. Figure 3.9 (c), on the other hand, shows the 2D cross section view with some layout parameters. The structure in Figure 3.9 (a) is obtained by extending the 2D profiles in the width (i.e. z-axis) direction. For simplicity, in the rest of the chapter, we will call this device as the "width-extended" structure. The structure in Figure 3.9 (b), on the other hand, in addition to structure in Figure 3.9 (a) includes also the edge terminations as in the experimental device. Therefore, it resembles the real structures better. For simplicity again from now on we will call this device as the "terminated" structure. For W = 124 µm, the 3D TCAD simulations with the terminated device was taking three days whereas it was one day with the width-extended structure. Hence, in order to gain time we have used the width-extended device to study variations in different layout parameters such as W, L, L_p and L_{pn}. The default values of L, L_p and L_{pn} are denoted as L_0, $L_{p,0}$ and $L_{pn,0}$, respectively, in further subjects. The terminated structure; however, helped us to understand the effects of edges on the IV curves. One may also notice that there exists a low p-doping at the surface of the active silicon layer all over the device. This is for elimination of influence of the oxide charges between silicon and the silicon-oxide passivation layer, which is at the top of the device. The passivation layer; however, is not shown so that the reader can see the doping profile distributions in Figure 3.9 (a) and (b) clearly.

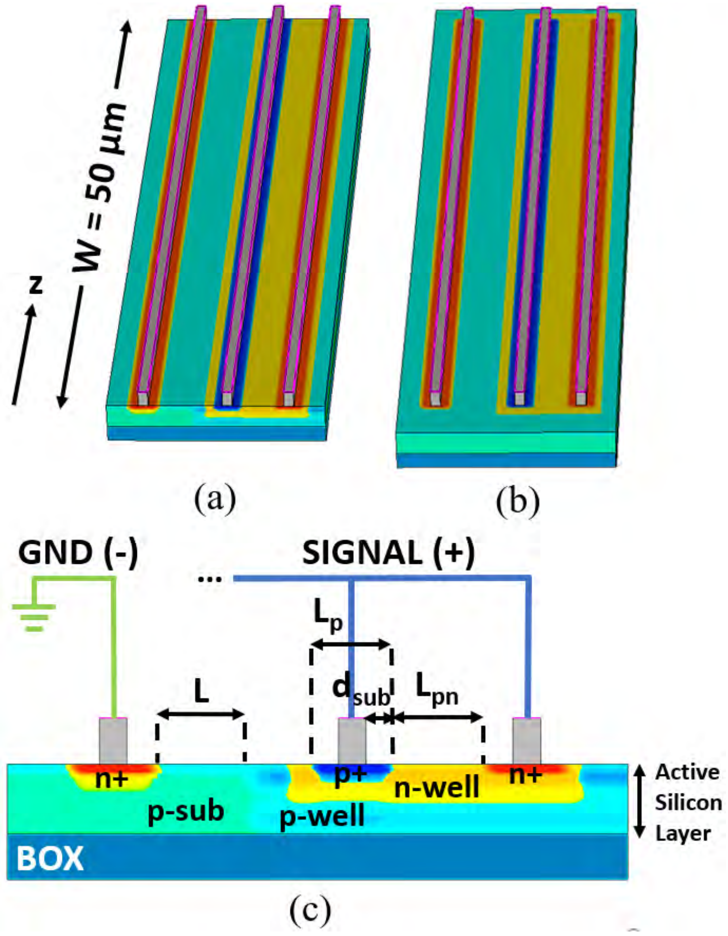

Figure 3.9: Devices used in 3D TCAD analysis with: (a) width-extended 2D profile and (b) edge termination. (c) 2D cross section view with some indicated layout parameters.

As the main approach corresponding to our TCAD methodology, up and down current sweeps with a rate of ±50 mA/s are used to produce the quasi-DC IV curve and to reveal the possible hysteresis behavior. Since the solution at the next iteration step depends on the previous distribution of internal state parameters like current densities, carrier concentrations, and electrical potential, the device prehistory is well taken into account. Besides that Neumann boundary conditions are applied at the edges of simulation region and since the self-heating effect at the applied low currents is negligible, isothermal simulations are employed. Separate contacts are implemented on top of p+-SIGNAL, n+ region of n-well and n+-GND regions to make individual analysis of current components. Total device current, on the other hand, is calculated as the sum of currents from the contacts at the Signal side.

During our first simulations, we have recognized that although in some simulations, which have structures with sufficiently long widths (W ≥ 45 µm, this will be clear later), we have a current filament and so a double hysteresis behavior, in other simulations we were not getting it. A double hysteresis behavior was not always emerging. For instance, in two simulations with different widths (W = 60 µm and W = 124 µm) we were getting a double hysteresis behaviour but in another simulation which has a width between theirs (W = 90 µm), we were not. This was understandable because the experimental devices have fluctuations in temperature, current density, doping concentration, lithography etc which results in an inhomogeneous current distribution while entering the NDR region. These parameters in our simulation structures, however, were quite homogeneous in spite of the natural asymmetry in mesh triangle orientation. In this respect, we made some attempts to introduce asymmetry in our 3D simulation structures so that we can have a double hysteresis behavior in all sufficiently wide devices. The purpose here was that while entering the NDR region, this asymmetry was going to amplify and always result in an inhomogeneous current flow.

3.4.1 Numerical aspects to induce instability

3.4.1.1 Adding a small doping to create inhomogeneity

The first trial to create inhomogeneity in the current flow was adding a small high n-doping within the n-well side of the reverse biased n-well/deep p-well junction as shown in Figure 3.10. Since the device part with this extra high n-doping will trigger at lower current density compared to the other sides, it was going to provide an inhomogeneous current flow through the device width and so cause a double hysteresis IV behavior. Different sizes of this extra doping was implemented but although the transition from homogeneous state (off-state) to filamentary state in the lower hysteresis part and the transition from filamentary state to homogeneous state (on-state) in the upper hysteresis part were created properly, the transition from homogeneous state (on-state) to filamentary state in the upper hysteresis part did not form. In addition, since there was no filamentary state while sweeping the current down, the transition from filamentary state to homogeneous state (off-state) in the lower hysteresis part was not also created. Table 3.1 summarizes the results and Figure 3.11 (a) and (b) shows the simulated IV curve for the case of 0.01µm*0.01µm*0.01µm extra doping size in full and zoomed scales, respectively. The device width is W = 124 µm and the blue arrows in Figure 3.11 indicate the current sweeping direction. The simulation model is not calibrated in details, so there is a small deviation between the experimental and simulated IVs (compare Figure 3.11 with with 3.6 (a) and (b)). The IV curve in Figure 3.11; however, can still qualitatively explain the behaviour observed in the experiments.

While the current is rising up, the extra doping was, indeed, causing an inhomogeneity in the current flow and so a current filament was emerging. This current filament; hence, was resulting in a vertical IV curve and briefly, the IV curve from point A to G (see Figure

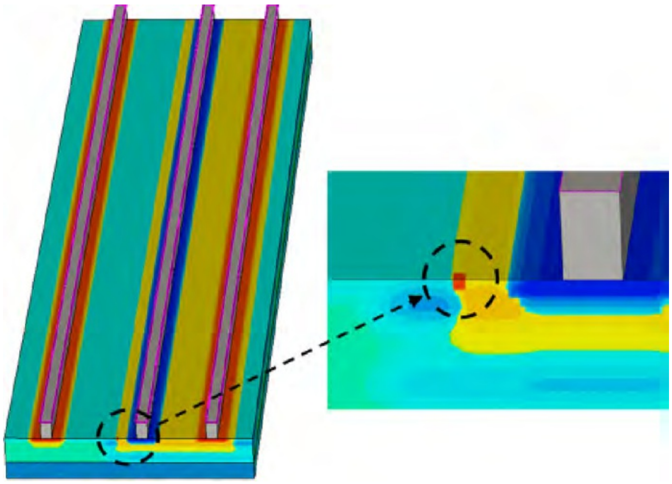

Figure 3.10: Adding a small extra high n-doping within the n-well side of the reverse biased n-well/deep p-well junction to induce instability.

Extra Doping Size	Transitions during Up-sweep	Transitions during Down-sweep
0.01µm*0.01µm*0.01µm	✓	✗
0.05µm*0.05µm*0.05µm	✓	✗
0.1µm*0.1µm*0.1µm	✓	✗

Table 3.1: The simulated IV curve for the case of 0.01µm*0.01µm*0.01µm extra doping size

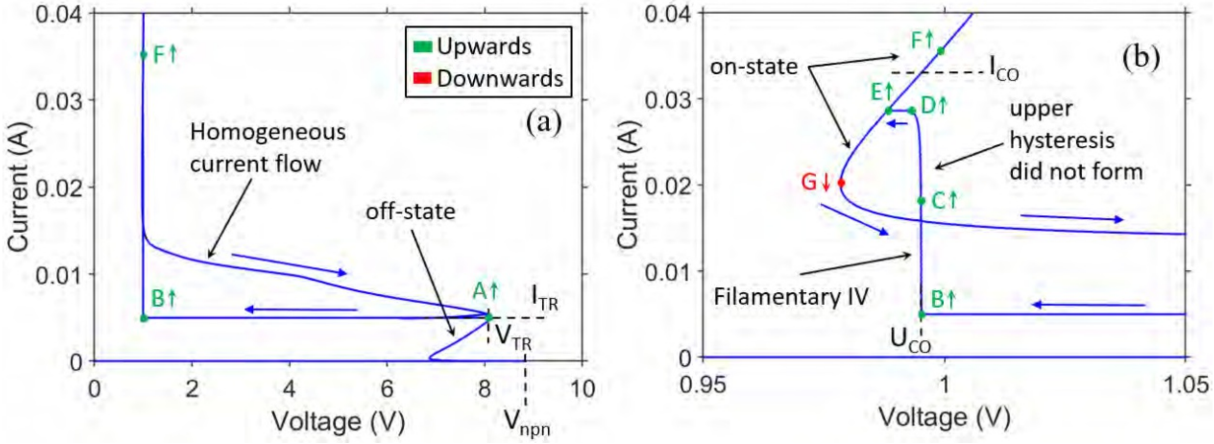

Figure 3.11: Simulated IV curve for the case of 0.01µm*0.01µm*0.01µm extra doping size in (a) full and (b) zoomed scales. The device width is W = 124 µm and the blue arrows indicate the current sweeping direction. The labels A-G in (a) and (b) are labeled according to the same qualitative behavior observed in Figure 3.6 (a) and (b).

3.6) was forming as discussed above in section 3.3. The problem was emerging when there has to be a jump from point G to point H (see Figure 3.6). This jump was not happening and so instead of forming a current filament, the current was decaying homogeneously through the device width like in 2D TCAD simulations [26, 38]. The reason for that was the ineffectiveness of the extra doping while there is a lot of free charges around. At point G, there was a homogeneous current everywhere and the number of carriers through the width of the device was comparable to the concentration of the extra doping. Thus, the extra doping was becoming ineffective to create an inhomogeneity in the current flow while sweeping the current down. During rising up the current, on the other hand, the number of carriers in the SCR off-state was small compared to the concentration of the extra doping and so the filametary states was appearing properly. Since this method did not allow us to observe double hysteresis behaviour in the IV curve as observed in the experimental devices, which has the same layout parameters, we decided to try another method.

3.4.1.2 Changing n-well doping concentration at one side of the device

Since adding a small extra doping in the previous attempt was ineffective to cause a jump from homogeneous state (on-state) to filamentary state in the upper hysteresis part (i.e. a jump from point G to H, see Figure 3.6), we thought that if we make the change in the size of the doping concentration bigger, we could achieve this. For this purpose, we have played with the n-well doping concentration at one side of the device by some percentages for 0.1 µm long width with respect to the original concentration. Figure 3.12 summarizes the method and Table 3.2 gives the results.

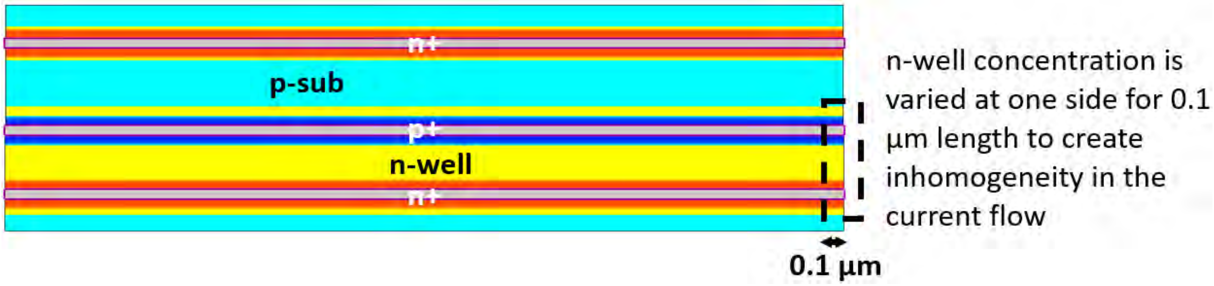

Figure 3.12: Varying the n-well doping concentration at one side of the device by some percentages for a length of 0.1 µm with respect to the original concentration

With these trials also although the current states during up-sweep were created successfully, they did not form during down-sweep. While the current is sweeping down; therefore, a inhomogeneous current distribution as in points H-K (see Figure 3.6 (b) and Figure 3.7) did not emerge. Instead of that, the current decayed homogeneously through the device. The resulting IV curves were similar to Figure 3.11.

3.4.1.3 Having missing contacts at one edge

Another attempt that we made to get a double hysteresis behavior was varying the length of the contacts and leaving some device region without contact. Figure 3.13 shows the

n-well conc. w.r.t. original (%)	Transitions during Up-sweep	Transitions during Down-sweep
95	✓	✗
99	✓	✗
101	✓	✗
105	✓	✗

Table 3.2: Summary table for IV behavior after varying the n-well doping concentration at one side of the device by some percentages for a length of 0.1 µm with respect to the original concentration

method we follow and Table 3.3 summarizes the results.

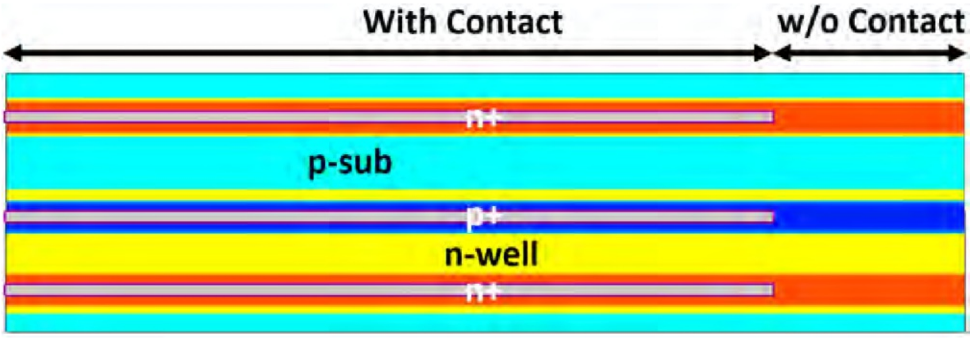

Figure 3.13: Varying the length of the contacts by leaving some device region without contact

Length of missing contact	Transitions during Up-sweep	Transitions during Down-sweep
0.01 µm	✓	✗
0.1 µm	✓	✗
1 µm	✓	✗
10 µm	✓	✗

Table 3.3: Summary table for IV behavior after having missing contacts at one edge

As it can be observed, the results were not different than the previous ones. The resulting IV curves were also similar to Figure 3.11. The current states during up-sweep were forming but they were not properly appearing during down-sweep. The double hysteresis behaviour; therefore, was not created. The reader may notice that in some trials the length of missing contact is quite huge compared to the experimental device widths. Since our trials with small changes did not work, we also made some big ones.

3.4.1.4 Adding an asymmetric finer mesh to one of the edges

After a lot of trial, it was later understood that the reason for not always getting a double hysteresis behavior in our 3D simulation structures which have sufficiently long width ($W \geq 45$ µm, will be clear later) was the mesh. The mesh in our simulation structures such as in region B of Figure 3.14 was quite symmetric through the device width. Thus, the natural mesh asymmetry created by the mesh generator was insufficient to induce a large enough inhomogeneity which causes a filamentary state in a wide device when entering the NDR region. In this respect, in order to induce the filamentary instability in devices with $W \geq 45$ µm, it was necessary to introduce an inhomogeneity into the mesh. For this purpose, we have added an extra finer mesh region as shown in region A of Figure 3.14. Table 3.4 summarizes the IV behavior for a device with $W = 50$ µm after applying this finer mesh in various widths. The most important criteria with this extra fine mesh was that the maximum refinement values of fine mesh (region A in Figure 3.14) and background mesh (region B in Figure 3.14) should mismatch with each other. They should not be a multiple of each other. For example, if the maximum mesh distance between the mesh points in z-direction is attained as 2 µm in the background mesh (region B in Figure 3.14), this variable should not be a value like 1 µm or 0.5 µm in the fine mesh (region A in Figure 3.14). Instead, it must be a value like 1.7 µm or 1.3 µm. Otherwise, in some simulations the extra fine mesh region was failing to create an asymmetry in the mesh distribution and so an inhomogeneous current flow was not happening. The same statement was also valid in other (x and y) directions. As for the minimum refinement values, on the other hand, there was not a criteria like that. They could be multiples of each other. In our simulations the used refinement values in both mesh regions (fine mesh and background mesh) for different refinement parameters are given in Table 3.5.

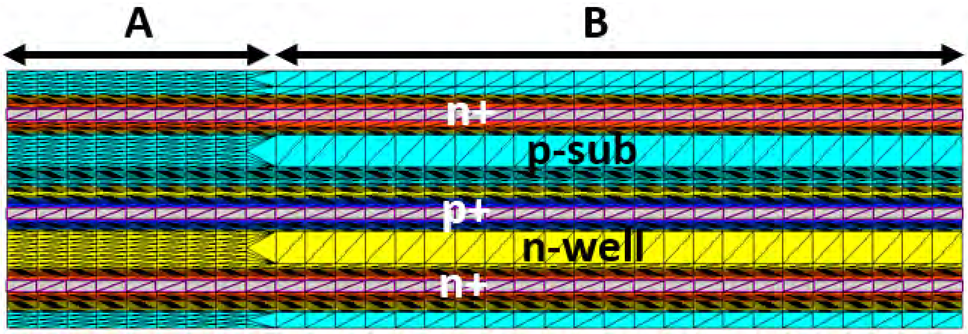

Figure 3.14: Adding an extra fine mesh (region A) in different widths in addition to a background mesh (region B)

As it can be observed, for fine mesh regions with width of 12.5 µm, 20 µm, 30 µm and 37.5 µm, both lower and upper hysteresis appears and so we get a double hysteresis behavior on the IV curve. This is because the filamentary instability can develop in wide devices only if the initial inhomogeneity extends over a large enough region, which is

Width of fine mesh (µm)	**Transitions during Up-sweep**	**Transitions during Down-sweep**
0.5 µm	✗	✗
1 µm	✗	✗
2 µm	✓	✗
5 µm	✓	✗
12.5 µm	✓	✓
20 µm	✓	✓
30 µm	✓	✓
37.5 µm	✓	✓
40 µm	✓	✗
45 µm	✓	✗

Table 3.4: Summary table for IV behavior for a device with W = 50 µm after adding an extra fine mesh (region A in Figure 3.14) in different widths in addition to a background mesh (region B in Figure 3.14)

Refinement parameters in a mesh	**Background mesh (µm)**	**Fine mesh (µm)**
max. in x-direction	2	0.3
max. in y-direction	2	0.3
max. in z-direction	2	1.7
min. in x-direction	0.1	0.05
min. in y-direction	0.1	0.05
min. in z-direction	2	1.7

Table 3.5: The used refinement values in both mesh regions (fine mesh and background mesh) for different refinement parameters

typically wider than the filamentary wall thickness L_{CF} [33, 34]. In our studies L_{CF} is around 9 µm. Therefore, having an asymmetric mesh of about 12.5 µm width or more than that fulfills the condition. Since with extra fine mesh, the simulation time increases, we have taken the minimum width of fine mesh that can create all filamentary states. Hence, we applied 12.5 µm fine mesh to our structures. Table 3.6 shows some data about duration of the 3D TCAD simulations depending on the width of fine mesh region, device width, device type.

Width of fine mesh region	Duration (hours)	Position of CF
0 µm (device width = 50 µm) (width-extended device)	6	CF does not occur without a finer mesh region
12.5 µm (device width = 50 µm) (width-extended device)	11	Starts at the edge with coarse mesh (B) region and ends at the edge with fine mesh (A) region
20 µm (device width = 50 µm) (width-extended device)	15.2	Starts at the edge with coarse mesh (B) region and ends at the edge with fine mesh (A) region
30 µm (device width = 50 µm) (width-extended device)	21	Starts at the edge with coarse mesh (B) region and ends at the edge with fine mesh (A) region
0 µm (device width = 62.2 µm) (width-extended device)	7.5	Starts and end at the same side
0 µm (device width = 62.2 µm) (terminated device)	19	
0 µm (device width = 124 µm) (width-extended device)	24	Starts and end at the same side
0 µm (device width = 124 µm) (terminated device)	72	

Table 3.6: Some data about duration of the 3D TCAD simulations and the position of CF depending on the width of fine mesh region, device width, device type.

3.5 Simulation results

3.5.1 Double hysteresis behavior in quasi-DC IV with a better calibrated structure and its explanation

The curve “3D” in Figure 3.6 (c) and (d) shows the simulated quasi-DC IV curve by sweeping the current up and down on a 3D TCAD simulation structure with width of W = 124 µm in full and zoomed voltage scales, respectively. As it can be observed, it exhibits a double hysteresis IV behavior. The IV curve “2D” in the same figures, on the other hand, represents a 2D IV behavior with homogeneous current flow over the width. Due to this homogeneity, the IV curve “2D” does not show any hysteresis behavior. For the reason of comparison, 2D TCAD IV simulation has been performed with a current ramp of 50mA/s (rising slope) as in the 3D TCAD IV simulations. Since the on-state and off-state regions of ”3D” and ”2D” IV curves are the same, to get a better calibrated “3D” curve, instead of running 3D TCAD simulations, we first did 2D TCAD simulations and calibrated the off-state and on-state regions of the IV curve. Once, the off-state and on-state regions of the 2D TCAD simulations were calibrated enough and we got ”2D” IV curve, we run the 3D TCAD simulation and obtained the ”3D” IV curve. The reason for this is that 2D TCAD simulations take less time compared to the 3D TCAD simulations. Nevertheless, the simulation model is not calibrated in details, so there is a small deviation between the experimental and simulated IVs (compare Figure 3.6 (a, b) with Figure 3.6 (c, d)). Our purpose here; however, is to concentrate on qualitative tendencies. For example, although the labels A-K in Figure 3.6 (a, b) and Figure 3.6 (c, d) are labeled identically according to the same qualitative behavior, the exact values of current and voltage can slightly differ. As in the experimental IV curve figures (see Figure 3.6 (a) and (b)), however, while the lower hysteresis is well pronounced in Figure 3.6 (c), the upper one (see encircled region in Figure 3.6 (c)) may seem to be overlooked.

Figure 3.15 shows the 3D plots of the current density distributions for the selected working points (the labels A-K) on the simulated IV curve in Figure 3.6 (c) and (d). In addition to that, in order to clearly see the current distribution in the z-direction, current density values across the line Ω-Ω’ (depicted in Figure 3.15 (A)) are extracted and plotted in Figure 3.16. The labels A-K in Figure 3.6 (c) and (d); therefore, also indicate the working points at which current density distribution, J(z), is extracted in Figure 3.16. For Figure 3.15 (C), moreover, the corresponding working point in Figure 3.6 (d) and Figure 3.16 is point C1.

While the total current is swiped up until the trigger current I_{TR}, SCR remains in the off-state as discussed in the experimental results (see Figure 3.7(A)) and mostly via the n-well substrate resistance of the pnp (cf. Figure 3.9 (c)), the off-state current flows homogeneously over the entire width (see Figure 3.15 (A) and curve A in Figure 3.16). Due to this homogeneous current flow in this regime, moreover, the same 3D and 2D

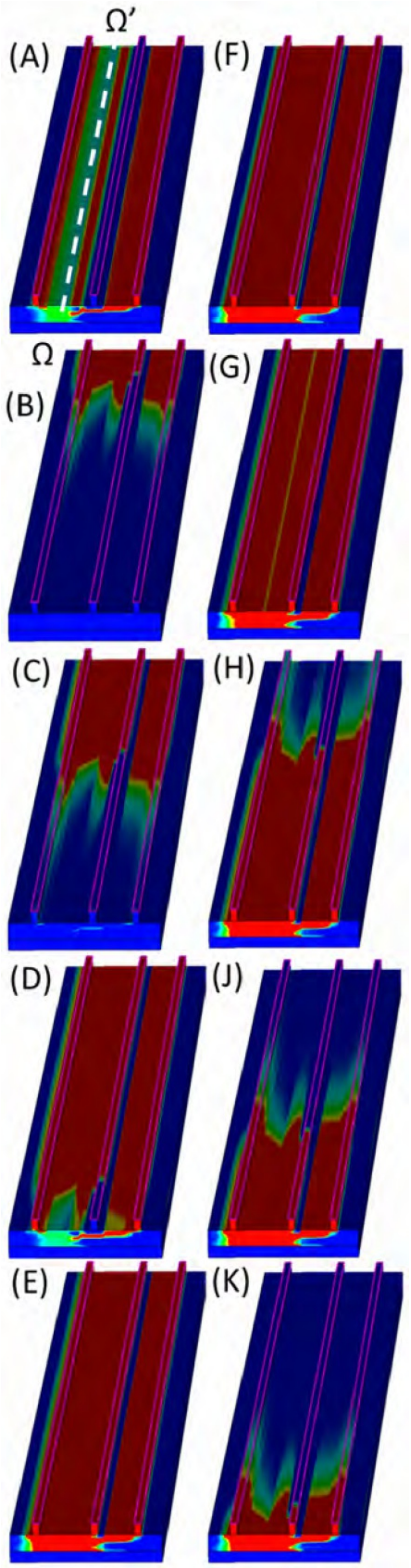

Figure 3.15: 3D TCAD simulated total current density distribution in width-extended device at working points A-K, from Figure 3.6 (c, d). In (C) the working point corresponds to C1 in Figure 3.6 (d) and Figure 3.16. The J(z) distribution is extracted along lines as Ω-Ω' indicated in (A).

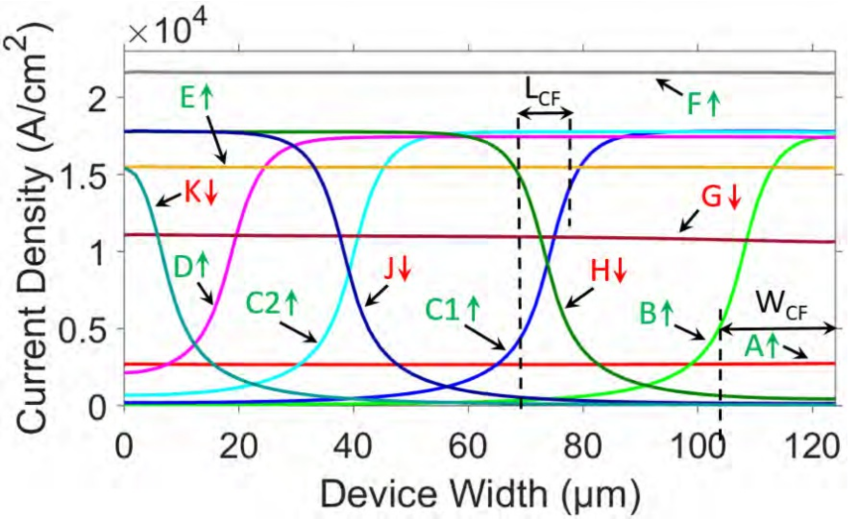

Figure 3.16: Extracted distribution of simulated total current density along the device width at different working points (A-K) from Figure 3.6 (c) and (d). The J(z) distributions are extracted from data of Figure 3.15, along lines such as Ω-Ω' in Figure 3.15 (A). The filament width W_{CF} is indicated in curve B. The filamentary wall thickness L_{CF} is indicated in curve C1.

IV behavior is observed below I_{TR} (see Figure 3.6 (c)). The small voltage peak V_{npn} seen in experiments, on the other hand, is qualitatively well reproduced (compare Figure 3.6(a) and (c)). Similar to the experiments, once the current reaches $I = I_{TR} = 5$ mA, a sufficiently high lateral potential drop across the p+/n-well junction (i.e. on the n-well resistance) at Signal occurs and the p-emitter starts to inject. The device; therefore, is driven into the NDR region and the voltage snaps back (see point B in Figure 3.6 (c) and (d)). The J(z) distribution at point B is shown in Figure 3.15 (B) and curve B in Figure 3.16. Then, since the simulated device is large enough ($W \geq 45$ µm, will be clear later), a CF develops and so at $V = U_{CO}$ [26, 33] (see Figure 3.6 (d)) a filamentary IV curve appears. The experimental U_{CO}, in addition, is accurately reproduced by the 3D TCAD (compare Figure 3.6 (b) and (d)). Here, we recommend reader to note that U_{CO} is higher than the holding voltage in the device with homogeneous current flow, V_{HOLD} (2D) (see Figure 3.6 (c) and [26]). Besides that the width of the initial CF appers to be $W_{CF} = 20$ µm (see Figure 3.16) which is consistent with its estimation from I_{TR}/J_{CO}, where $J_{CO} \approx 0.25$ mA/µm. The CF is created and pinned at the right boundary (see Figure 3.15 (B) and curve B in Figure 3.16) but a CF creation at the left one is also possible depending on the actual mesh inhomogeneities (for details, see Table 3.6).

On the filamentary IV part, the J(z) distribution can be directly related to the distribution of the B-E voltage of the pnp transistor, which controls the SCR action. The on and off state regions, in addition, can be separated by a transition region called the filamentary wall having the thickness of L_{CF} (see Figure 3.16 and [26, 29, 33]). The balance between the on and off states at the filamentary wall, on the other hand, determines the value of U_{CO} [29, 33, 34]. W_{CF} increases with current according to Equation 3.1 as in the experiments (see points C1 and C2 in Figure 3.6 (d), Figure 3.15 (C) and curves C1 and C2 in Figure 3.16). Once we reach point D (see Figure 3.6 (d)); however, due to instability of the inhomogeneous filamentary state, a transition to homogeneous on state occurs (see points E in Figure 3.6 (d), Figure 3.15 (E) and curve E Figure 3.16). The voltage jump from working points D to E, in this respect, represents an energy gain related to the disappearance of the CF wall [26, 33]. The current difference dI between point D and the point at the on-state IV curve at U_{CO}, (see Figure 3.6 (d)), on the other hand, is related to a missing current flow over the region with thickness of nearly L_{CF}.

At high currents above point E (see Figure 3.6 (d)), the current flows homogeneously as in the experiments (see Figure 3.15 (F) and curve F in Figure 3.16) and this homogeneity also continues while sweeping the current down until the point G (see Figure 3.6 (d)). Here, it can be also noticed that since the current is homogeneous in the on-state, 3D IV (curve "3D") and 2D IV (curve "2D") characteristics in Figure 3.6 (d) are identical. Below point G; however, a transition from homogeneous on state to filamentary state occurs due to entrance of device into the NDR region and a CF is created again. The voltage; therefore, jumps to point H (see Figure 3.6 (d)). Interestingly, in this simulation the CF at point H is pinned at the left boundary, which is the opposite side of the device compared to the side that the current rose initially (compare curves H and B-D in Figure 3.16). However, the CF can be pinned also at the right boundary, depending on mesh details, current step, etc. With further reduction of the current, W_{CF} decreases (see Figure 3.15 (J) and curve J in Figure 3.16) and at the working point K (see Figure 3.6 (d)) the lowest current where the SCR still operates in the on-state, called 3D I_{HOLD}, or I_{HOLD}(3D), is reached. Figure 3.15 (K) and curve K Figure 3.16; thus, show a small CF at the structure edge. The width of CF, W_{CF}, at the working point K is equal to L_{CF}. If we calculate the value of L_{CF} from $I_{HOLD}(3D)/J_{CO}$, we find its value as approximately 9 µm. This value, in addition, is consistent with the 20% to 80% variation in J(z) (see Figure 3.16). In other words, the distance between 20% and 80% of the maximum current density on a filamentary wall gives us the filamentary wall thickness L_{CF}. This criteria is important to note here because in our further analyses, L_{CF} values will be calculated according to 20% to 80% variation in J(z). Besides that, due to the filamentary nature of conduction, I_{HOLD}(3D) of about 2 mA is much lower than $I_{HOLD}(2D) \approx 20$ mA (see Figure 3.6(d)). The current density, inside of the CF, of nearly $J_{CO} = 0.25$ mA/µm, on the other hand, is higher compared to that at I_{HOLD}(2D) of $I_{HOLD}(2D)/W \approx 0.16$ mA/µm. This shows us that the SCR action in CF at I_{HOLD}(3D) is supported by a sufficiently high current density. Finally, below point K, the self-sustaining operation of SCR is not possible anymore as in the experiments. Hence, through the open base npn (see Figure 3.9 (c)) the current flows again homogeneously over the device width (see point L in Figure 3.6 (c)).

3.5.2 Effect of different layout parameters on I_{HOLD}

According to the theory in [29, 109], the filamentary instability occurs in devices wider than about 5xL_{CF}. Therefore, since in our case L_{CF} is about 9 µm, IV characteristic in devices with a width of $W \geq 45$ µm show a double hysteresis behavior. In this respect, in order to cover regimes below and above 5xL_{CF}, we have carried out simulations of both types of devices (width-extended and terminated) with W in the 2 µm 185 µm range. Within the measured devices, on the other, hand, only the devices with $W = 31.3$ µm stays below this criterion.

3.5.2.1 Effect of width

Examples of experimental and 3D-simulated IV curves for width-extended devices are given in Figure 3.17 (a, b) and Figure 3.17 (d, e), respectively, in different scales. For better visibility, the curves in Fugure 3.15 (a) and (d) are subsequently horizontally fanned out with 20 mV distance between two curves. So one should not think that the U_{CO} value change with device width W. Rather, it does not depend on W. As it can be observed the experimental devices with $W \geq 62.2$ µm and simulated devices with $W \geq 50$ µm show a double hysteresis behavior. The devices with smaller widths, on the other hand, shows an IV behavior similar to curve "2D" in Figure 3.6 (c) and (d). In addition to that, although I_{TR} values increase with the enhancing width values as shown in Figure 3.17 (c), V_{TR} stays the same.

The I_{HOLD} values extracted from the IV data of Figure 3.17 (a) and (d) are given in Figure 3.17 (f). As it can be observed, in the experiments, I_{HOLD} for $W = 31.3$ µm is slightly smaller than the values for $W \geq 62.2$ µm. As for simulation, on the other hand, the simulated I_{HOLD} first shows a linear increase with W until $W = 40$ µm and then it jumps to a constant value for $W \geq 45$ µm. This is because for $W < 45$ µm the device is not large enough to induce the NDR instability which is consistent with the 5xL_{CF} criterion and so the values of I_{HOLD} from 2D and 3D TCAD are identical. Thus, I_{HOLD} scales linearly with W. This can be directly seen in the IV curves where the double hysteresis and ideal filamentary IV behavior is not formed for the device with $W = 31.3$ µm in experiments (Figure 3.17 (a)) and for $W = 10$ µm and $W = 30$ µm in simulations (Figure 3.17 (d)). At that point we also notice that the lack of devices with widths in the 30 - 50 µm range prevents us to see the linearly increasing part in the I_{HOLD} - W dependence in the experimental data. For the devices with $W \geq 62.2$ µm in experiments (Figure 3.17 (a)) and for $W = 50$ µm, $W = 90$ µm and $W = 124$ µm in simulations (Figure 3.17 (d)), on the other hand, I_{HOLD} values determined from experiments and 3D TCAD are almost width-independent and substantially lower than those evaluated from 2D TCAD. In this respect, the conventional 2D TCAD can provide unwanted over-estimation of I_{HOLD}.

Since IV curves in ESD community are usually plotted normalized according to device width (i.e. I/W), Figure 3.18 (a) shows the comparison of the simulated IVs near U_{CO}

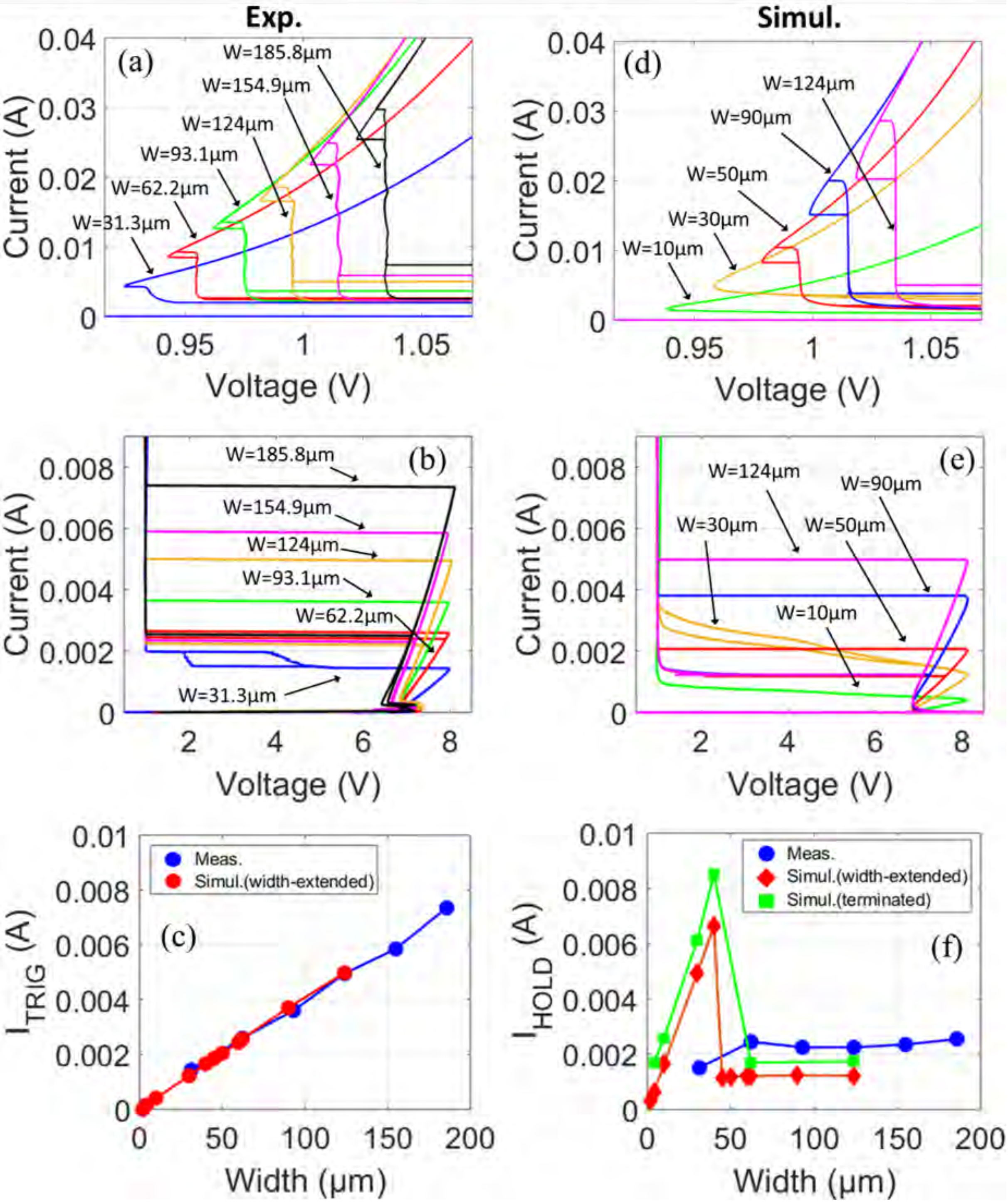

Figure 3.17: Experimental (a, b) and 3D TCAD simulated (d, e) IV curves for the width-extended device with the device width W as a parameter. For better visibility the curves in (a) and (d) are fanned out with 20 mV distance between two curves. The U_{CO} value does not depend on the device width W. (c) I_{TR} dependence on W, extracted from data of (b) and (e). (f) Measured and simulated I_{HOLD} values extracted from data of (a) and (d). The data points for the terminated device are also included. In the case of no CF creation for W < 45 µm, the value of I_{HOLD} (2D) is considered for I_{HOLD}.

for the width-extended devices in the normalized scale. As it can be obviously seen, the matching for W ≥ 50 µm occurs only in the on-state and off-state (not shown) branches of the IV curves where the current flows homogeneously. The normalized curves differ in the transition regions from filamentary state to on-state, in the upper hysteresis. The normalized IV curves for W = 30 um and 10 um, on the other hand, overlap since they do not exhibit filamentary behavior. Besides that, Figure 3.18 (b) presents the change in dI values (see Figure 3.6 (d)) with W in both experiments and width-extended device simulations.

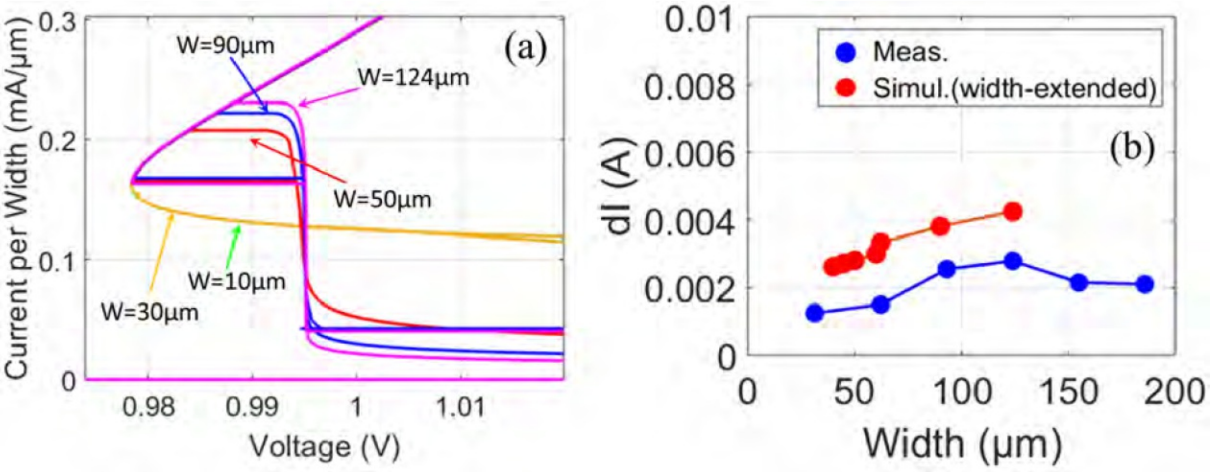

Figure 3.18: (a) Zoom of IV curves near U_{CO} for the width-extended device where the vertical scale is normalized by W. The normalized IV curves for W = 30 um and 10 um overlap since they do not exhibit filamentary behavior. (b) the change in dI values (see Figure 3.6 (d)) with W is given for both experiments and width-extended device simulations

3.5.2.2 Effect of edge termination

Figure 3.19 (a) and (b) compares the 3D IV curves of the width-extended and terminated structures for W = 124 µm. Although the trigger parameters (V_{TR} and I_{TR}) are nearly identical (see Figure 3.19 (a)), I_{HOLD} increases by 30% for the terminated device (see Figure 3.19 (a)). Furthermore, one can observe a transition from the on-state to filamentary IV curve at higher currents in the down-sweep than in the terminated device, as indicated by the thick arrow in Figure 3.19 (b). This is because the termination induces an inhomogeneity and so facilitates an earlier transition to the filamentary state. The small horizontal arrows, on the other hand, indicate the current sweeping direction. Figure 3.19 (c) and (d), on the other hand, presents the 3D-simulated IV curves for different widths in full and zoomed scales, respectively. In Figure 3.19 (d), the curves are subsequently horizontally fanned out with 10 mV distance between two curves for better visibility. Thus, U_{CO} does not change with device width W as in the width-extended devices. The voltage jumps in the upper hysteresis part of the simulation for W = 62.2 µm (see Figure

3.19 (d)) is also not well-visible due to scale of the figure. In addition to that, as in the width-extended devices, although I_{TR} values increase with the enhancing width values as shown in Figure 3.19 (c), V_{TR} stays the same.

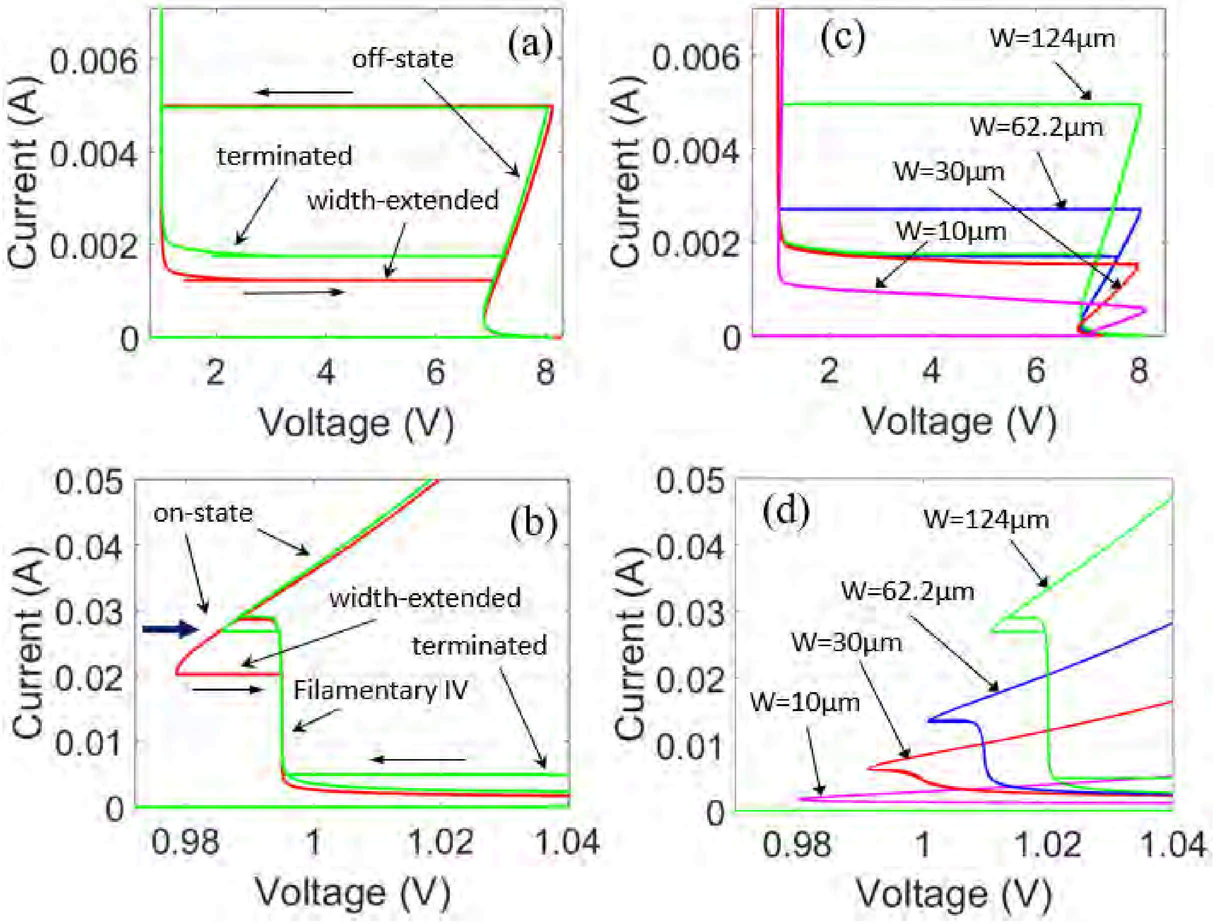

Figure 3.19: 3D TCAD simulated IV curve for the width-extended and terminated devices in the full (a) and zoomed (b) scale. W = 124 um. The thick arrow in (b) indicates the early transition from on-state to filamentary state in the terminated device. The small horizontal arrows indicate the current sweeping direction. the 3D-simulated IV curves for different widths in (c) full and (d) zoomed scales. For better visibility, the curves in (d) are fanned out with 10 mV distance between two curves. The value of U_{CO} does not depend on the device width W.

The simulated I_{HOLD} values of the terminated devices as a function of W are included in Figure 3.17 (f) (see the green squares). Similar to the case with the width-extended device, also for the terminated device, the critical device width for the CF creation of about 45 µm fulfils the $5xL_{CF}$ criterion. In the same figure, in addition, one can remark that I_{HOLD} in the terminated devices is higher than that in the width-extended structures and this difference is nearly width-independent for $W > 60$ µm. This can be attributed to an additional current flow around the edge. One can also notice in Figure 3.17 (f) that the I_{HOLD} values of the terminated devices match better to the experimental values. This increased accuracy, however, is accompanied with an increasing simulation time. In this respect, since I_{HOLD} for the width-extended device is lower than for the terminated device, one can state that even though the width-extended device simplifies the 3D TCAD IV analysis, it represents the worst-case scenario in I_{HOLD} estimation. This is true, however, for the computational time saving reasons, I_{HOLD} for other layout variations will be evaluated only for the width-extended device with W = 50 µm. The width has been chosen as 50 µm because for this width a CF is certain to be created.

3.5.2.3 Effect of active silicon layer thickness

Figure 3.20 (a), (b), (c) and (d) present the simulated current per width (J_{CO}), filamentary wall thickness (L_{CF}), I_{HOLD} and dI (see Figure 3.6 (d)) values for different active silicon layer thicknesses (see Figure 3.9 (c)) in an arbitrary unit, respectively. The width of the simulated structures, on the other hand, is W = 50 µm. With the increase of the thickness of the active silicon layer, the effective resistance of p-sub in the on-state (see Figure 3.6 (d)) that the flowing current faces decreases and so I_{CO} shifts to a higher current value (see Figure 3.6 (d)). Then, since $J_{CO} = I_{CO}/W$, J_{CO} increases. We observe this effect clearly until the active silicon layer thickness of 2 in Figure 3.20 (a). Most of the current flows within the active silicon layer thickness of 1 from the surface. The amount of current from surface into the deeper region of active silicon layer, in addition, decreases exponentially as shown in Figure 3.20 (e). That is why, the increase in J_{CO} is not linear but close to logarithmic. For thicknesses larger than 2, on the other hand, the effective value of resistance that current faces does not change so much. However, some of the free carriers still moves into deeper regions of the p-sub and do not contribute to the current. Hence, for the same voltage, we observe a smaller current in the on state of the IV curve. That means I_{CO} and so J_{CO} shifts to a lower value (see Figure 3.6 (d)). The fall in current per width (J_{CO}) values in Figure 3.20 (a) after the silicon layer thickness of 2 can be attributed to this reason.

The L_{CF} values, on the other hand, first increases with the enhancement of the thickness of the active silicon layer due to the reduction in the effective resistance of p-sub. This is because, due to the lower effective p-sub resistance, the filamentary wall elongates through the width. After some thickness value; however, since most of the current flows through the surface, the width of the CF do not change so much any more and so L_{CF} values stays nearly the same.

Since at the current value I_{HOLD}, the width of the filamentary wall is equal to L_{CF}, this gives us a relation that

$$I_{HOLD} \approx J_{CO} \cdot L_{CF} \tag{3.2}$$

In this respect, I_{HOLD} values follow a trend consistent with Equation 3.2 (see the blue curve in Figure 3.20 (c)). 2D TCAD simulations, on the other hand, overestimates I_{HOLD}. As for dI values, due to above mentioned process of J_{CO} values, they also show a trend

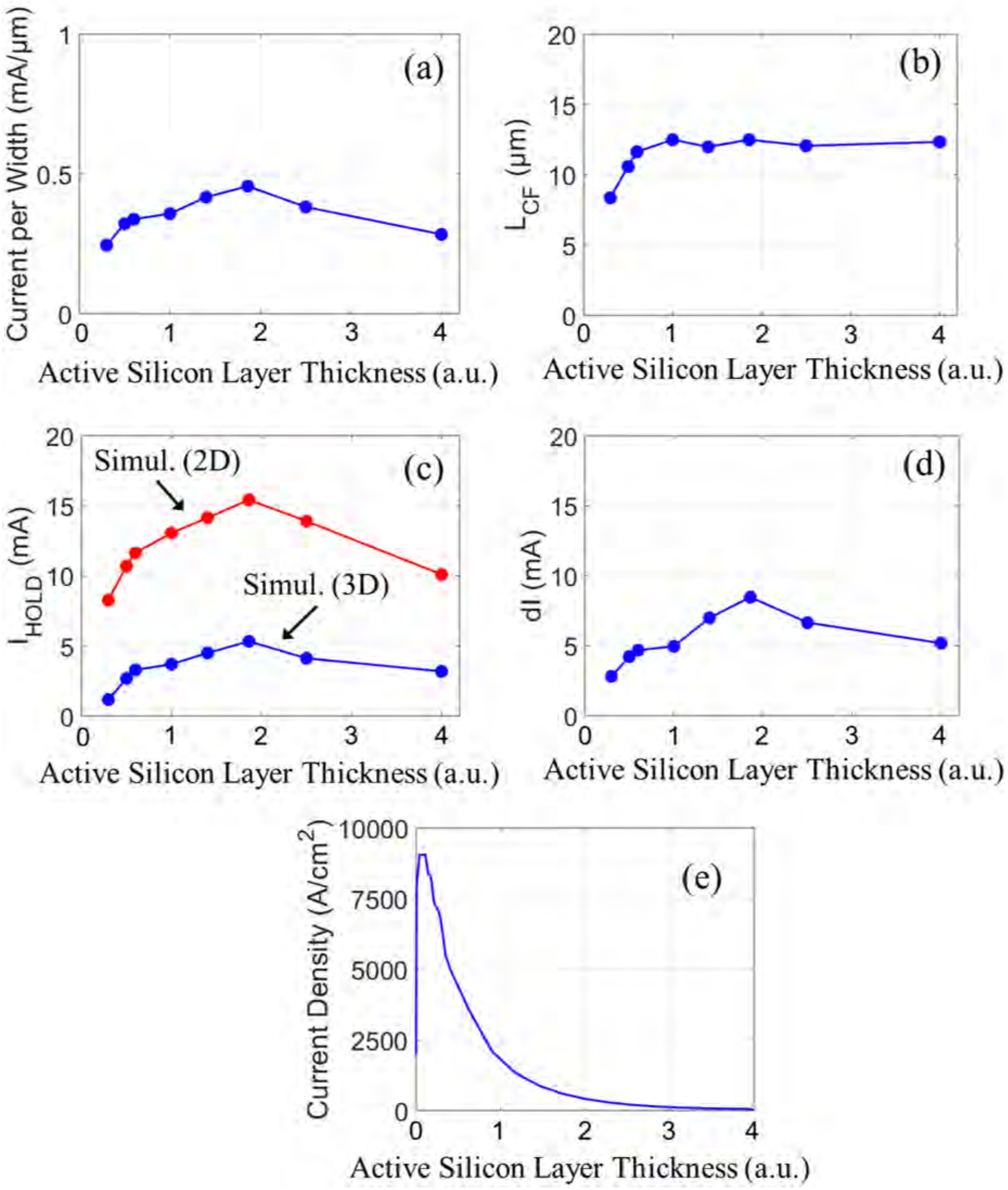

Figure 3.20: (a) Current per width (J_{CO}), (b) filamentary wall thickness (L_{CF}), (c) I_{HOLD} and (d) dI (see Figure 3.6 (d)) values for different active silicon layer thicknesses in an arbitrary unit. (e) The amount of current from surface into the deeper region of active silicon layer decreases exponentially.

similar to what is shown in Figure 3.20 (a).

3.5.2.4 Effect of silicon extension at the edge

In order to understand the effect of the simulation area on the IV behavior, we have added a 20 µm silicon at one of the edges (i.e. in the z-direction) of the width-extended simulation structure as shown in Figure 3.21 (a). The width of the width-extended device, on the other hand, is W = 50 µm. As it can be observed, although the V_{TR} stays the same, I_{TR} increases after the extension. This is because since the doping profiles and device parameters (see Figure 3.9 (c)) are same in both structures, p-emitter starts to inject once we reach V_{TR}. Due to flow of the current in the off-state also towards the extended silicon region; however, some portion of the current in the device with extra silicon extension cannot directly contribute to the triggering and so cause an increase in I_{TR}.

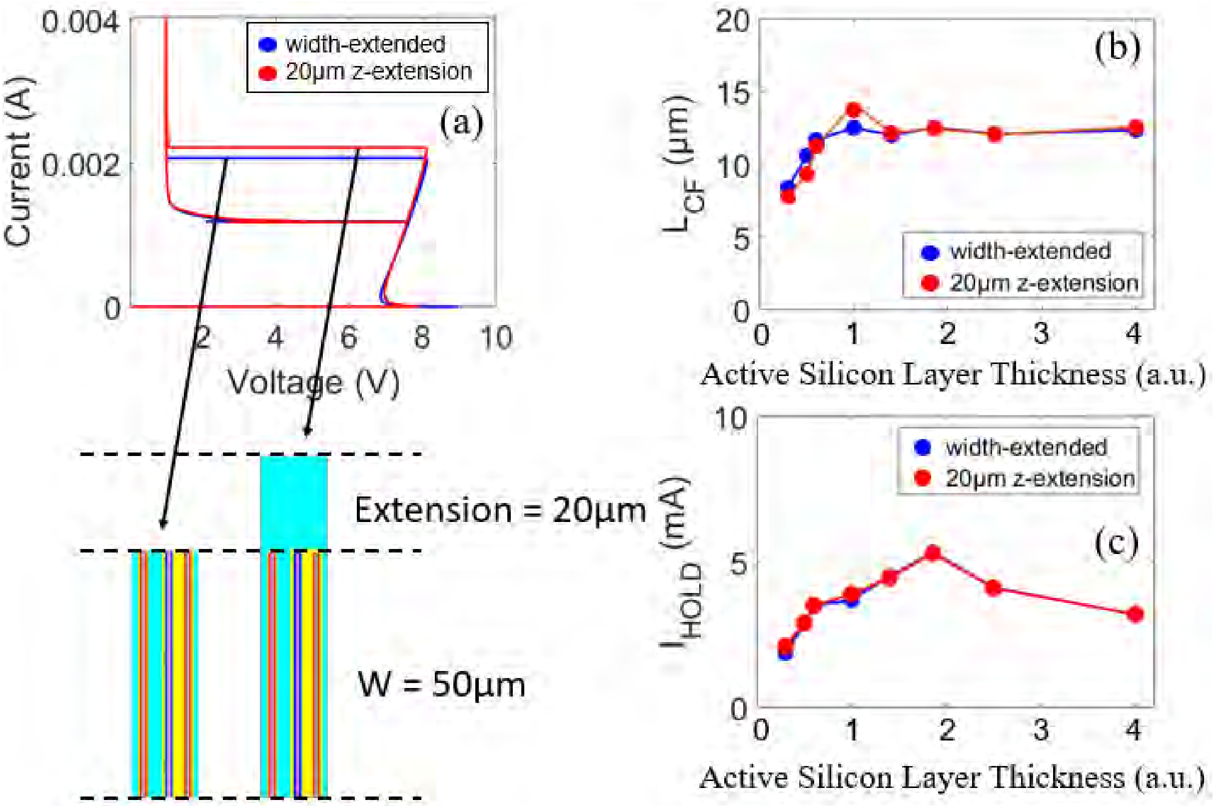

Figure 3.21: (a) Comparison of IV behavior between, the width-extended simulation device with W = 50 µm, and the simulation structure which has an extra 20 µm silicon region at one of the edges of the width-extended device. Comparison of (b) L_{CF} and (c) I_{HOLD} values.

When we compare the L_{CF} and I_{HOLD} values as shown in Figure 3.21 (b) and (c), on the other hand, we observe not so much difference. Both simulations show the same trend with nearly the same values. This result; therefore, simplifies the analysis and tell us that we do not need to add an extra silicon region at one of the edges when evaluating I_{HOLD}. A smaller simulation area also provides us a shorter simulation time.

3.5.2.5 Effect of lateral silicon extensions

Another method that we applied to investigate the effect of the simulation area on the IV behavior is extending the device in lateral dimensions as shown in Figure 3.22 (a). The width-extended device is laterally extended by 5 µm and 10 µm. Figure 3.22 (b), on the other hand, evaluates the effect of these extensions on I_{HOLD} values. As it can be seen, lateral extension has a weak influence on I_{HOLD}. It shows that the SCR action occurs in a certain limited volume and that it is not necessary to enlarge the simulation area beyond this volume. This result; hence, simplifies the analysis again and help us to conduct our simulations in shorter time by reducing the simulation area.

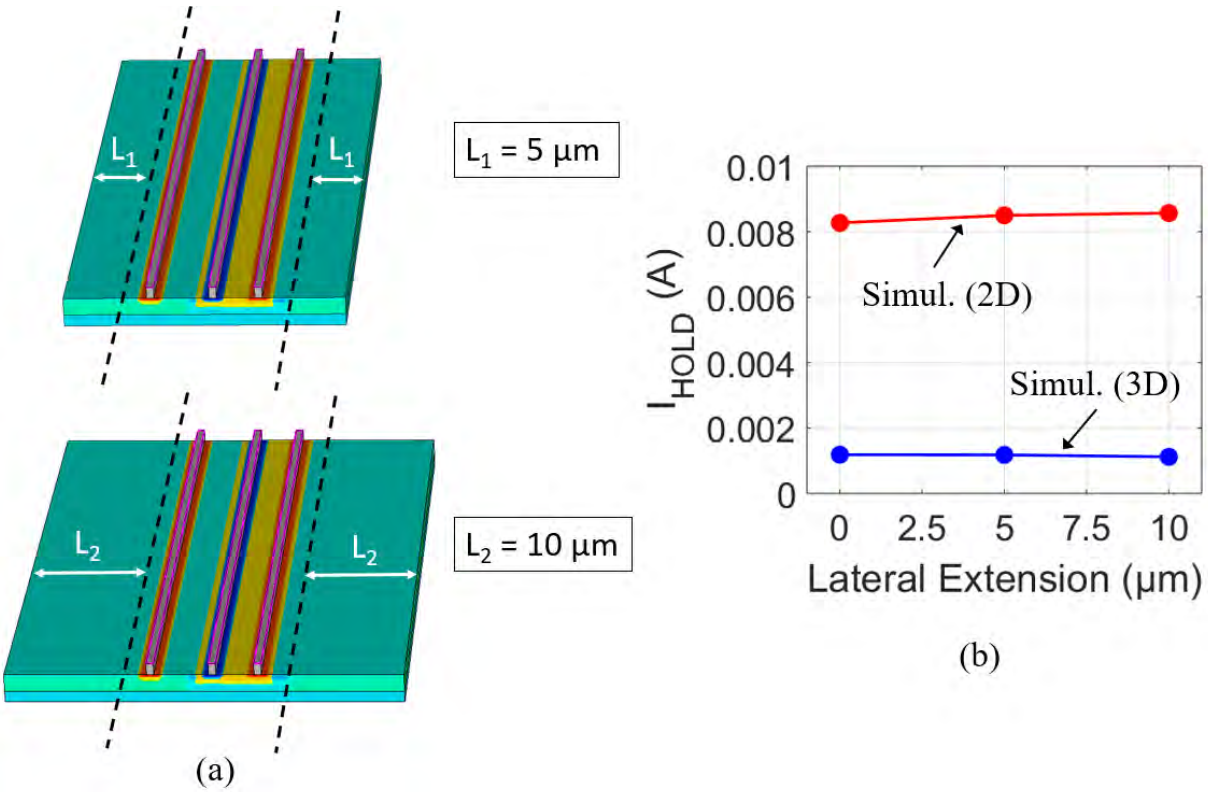

Figure 3.22: (a) The width-extended device is laterally extended by 5 µm and 10 µm. (b) Effect of lateral extension on I_{HOLD}.

3.5.2.6 Effect of the distance between n+-GND and deep p-well (L)

Figure 3.23 (a, b) and Figure 3.23 (c, d) show the experimental and simulated IV curves as a function of L which is the distance between n+-GND and deep p-well (see Figure 3.9(c)). Figure 3.2 (a) and (c) show the IV curve near the V_{TR} whereas Figure 3.23 (b) and (d) presents IV curve near U_{CO}. As it can be observed, in both experiment and simulation, open base breakdown voltage of the npn and V_{TR} shifts slightly to higher values with increasing L values. This is because with the increase of L, the base width of npn enhances and so its gain decreases. The extracted values of I_{HOLD} from 2D and 3D simulations are given in Figure 3.23 (e). While I_{HOLD} (2D) increases with L, I_{HOLD} (3D) is L-independent and much lower than I_{HOLD} (2D). That means 2D TCAD, in these simulations, provide unwanted over-estimation of I_{HOLD}.

3.5.2.7 Effect of the distance between n+-SIGNAL and Signal p+-SIGNAL (L_{pn})

Figure 3.24 (a) and (b) show the simulated IV curves with L_{pn} (see Figure 3.9 (c)) as a parameter near V_{TR} and near U_{CO}, respectively. As it can be observed, the value of I_{TR} for the studied layout range does not depend much on L_{pn} (see Figure 3.24 (a)). This can be explained as following: I_{TR} depends on the total n-well resistance over the length d_{sub} below p+ and in the region of length L_{pn} (see Figure 3.9 (c)). However, since through the length d_{sub} below p+ the net n-well doping is lower than that in the region of the length L_{pn}, n-well resistance part of length d_{sub} mainly determines the total n-well resistance and controls the forward biasing of the p+/n-well junction necessary for pnp triggering. Then, since d_{sub} is L_{pn}-independent, changing L_{pn} does not so much effect I_{TR} values. For the same reason, in addition, the differential resistance below I_{TR} also does not depend much on L_{pn}. The extracted values of I_{HOLD} from 2D and 3D simulations, on the other hand, are shown in Figure 3.24 (c). There, while I_{HOLD}(2D) decreases with L_{pn}, I_{HOLD} (3D) is lower and layout independent. 2D TCAD simulations; therefore, overestimates the I_{HOLD} values also for these simulations.

3.5.2.8 Effect of length of p+-SIGNAL (L_p)

Figure 3.25 (a) and (b) present the simulated 3D IV curves as a function of p+ length (L_p) (see Figure 3.9 (c)) around V_{TR} and near U_{CO}, respectively. As discussed previously, since the value of n-well resistance is mostly determined by the region below p+, the increase of L_p enhances the value of n-well resistance and thus this results in a decrease in I_{TR} (see Figure 3.25 (a)). In addition, one can notice in Figure 3.25 (b) that for higher values of L_p, the simulation structure does not show a double hysteresis behavior. The I_{HOLD} values from 2D and 3D TCAD simulations; therefore, coincides with each other at high L_p values as shown in Figure 3.25 (c). This is an important result because it shows us a condition that can directly affect the existence of the double hysteresis IV behaviour. This can be explained as following. With the increase of the n-well resistance, smaller currents on the n-well resistance become enough to trigger the pnp of the SCR. Thus, more device region along the device width starts to become active under the same applied current. The filamentary wall of CF; therefore, elongates through the device width. That is, L_{CF} increases with L_p. Figure 3.25 (d) shows the change in L_{CF} for $L_p = L_{p,0}$ and

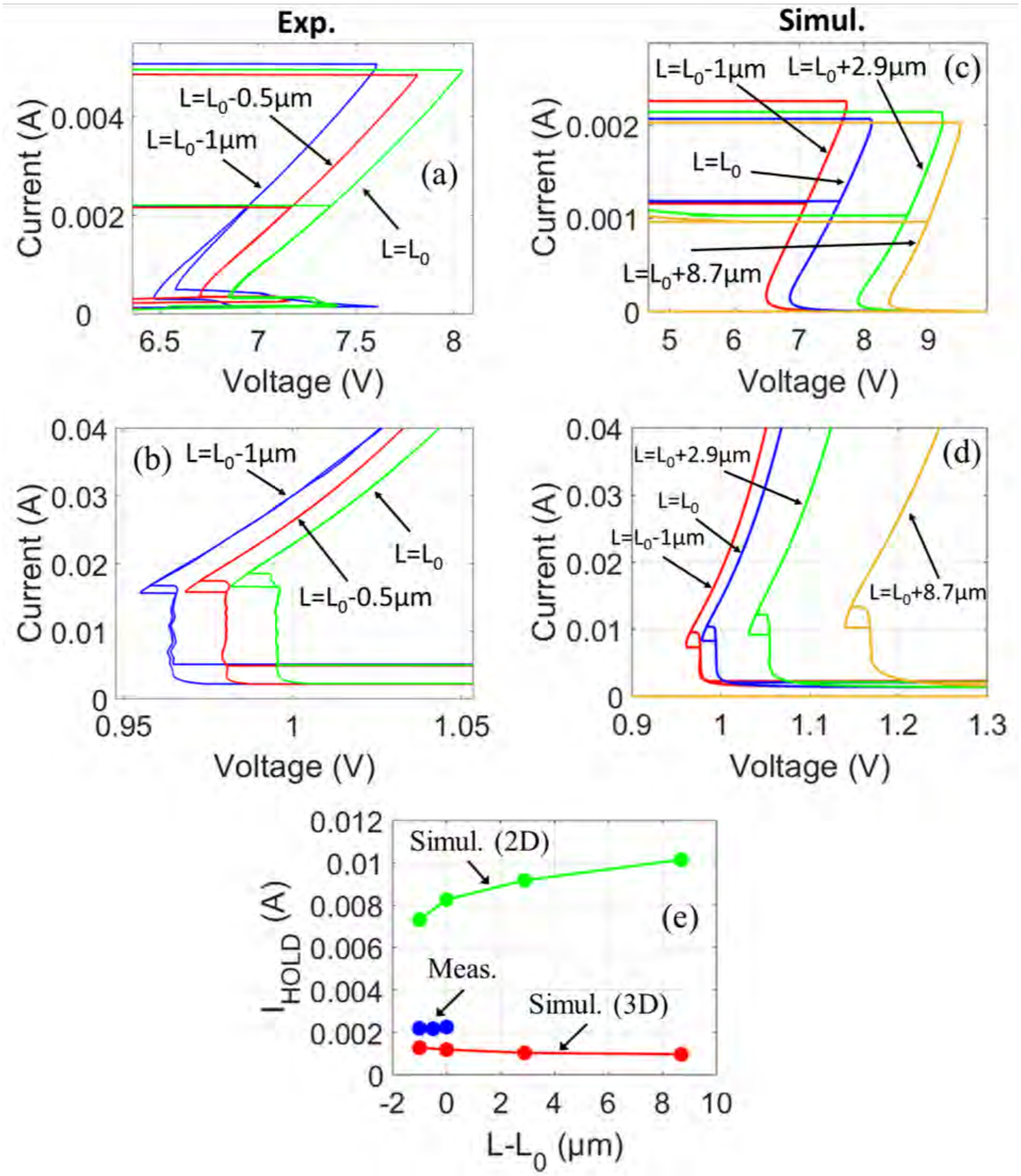

Figure 3.23: Experimental (a,b) and 3D TCAD simulated (c,d) IV curves for the width-extended device as a function of L near V_{TR} (a,c) and near U_{CO} (b,d) voltages. (e) Extracted measured I_{HOLD} and simulated values of I_{HOLD} (3D) and I_{HOLD} (2D) as a function of L.

$L_p = L_{p,0} + 1.2$ µm. Since for $L_p = L_{p,0} + 3.6$ µm and $L_p = L_{p,0} + 8.4$ µm there is no CF, L_{CF} data for them are not included. After a value between $L_p = L_{p,0} + 1.2$ µm and $L_p = L_{p,0} + 3.6$ µm, however, the filamentary instability is lost and we start to observe

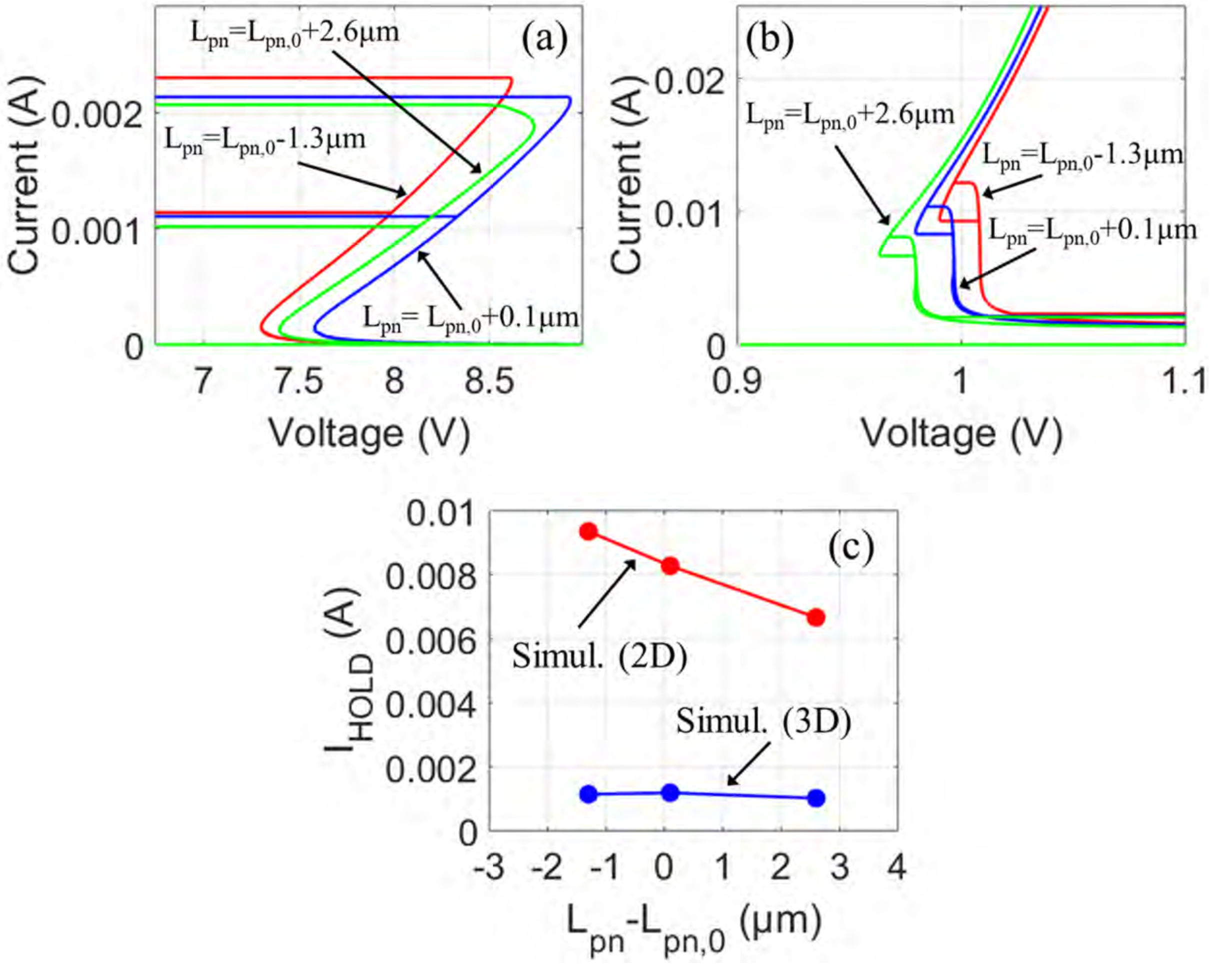

Figure 3.24: Simulated 3D IV curves for the width-extended device in full (a) and zoomed (b) scales with L_{pn} as a parameter. (c) Extracted simulated values of I_{HOLD} (3D) and I_{HOLD} (2D) as a function of L_{pn}.

a homogeneous current distribution through the device width. Due to this homogeneous current flow; therefore, IV curves become similar to that from 2D TCAD simulations.

To conclude, experiments with multi-finger devices showed us that I_{HOLD} is determined by the last active finger/segment in multi-finger devices, independent of the position of it. Thus, the behavior of I_{HOLD} was investigated by studying single finger devices.

We have seen that the way we measure had an influence on the IV curve. For example, although the IV curves obtained by HP 4155A Semiconductor Parameter Analyzer was exhibiting a double hysteresis IV behaviour for devices with W ≥ 62.2 μm, the IV curves from Keithley 2410 SMU was producing serious oscillations due to parasitic elements in the measurement chain. To deal with this issue, TDK ZCAT ferrite beads were used on the measurement cables and so oscillations were mostly damped.

A current filament (CF) and so a double hysteresis IV behaviour was observed only

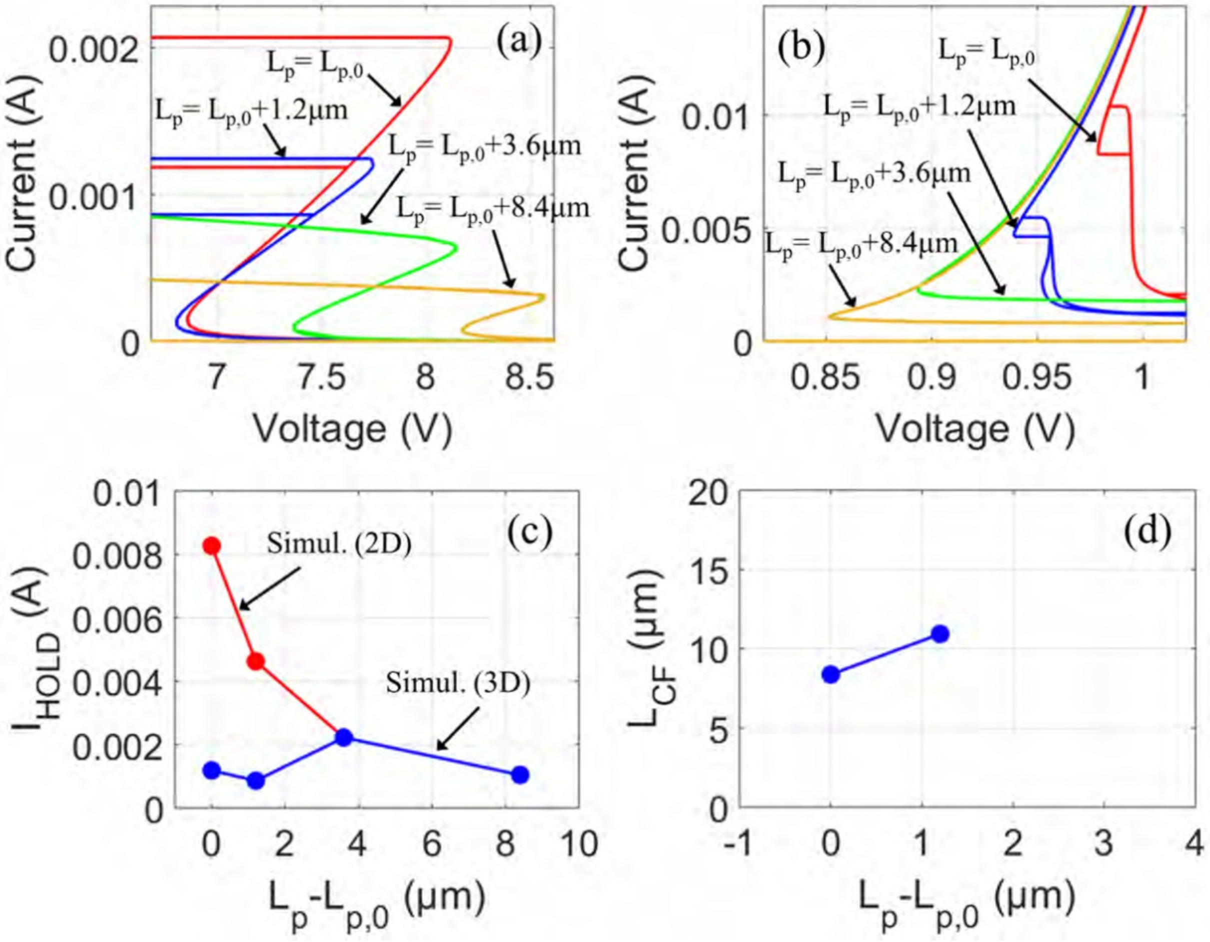

Figure 3.25: Simulated 3D IV curves for the width-extended device in full (a) and zoomed (b) scales with L_p as a parameter. (c) Extracted simulated values of I_{HOLD} (3D) and I_{HOLD} (2D) as a function of L_p. (d) Extracted simulated L_{CF} values for $L_p = L_{p,0}$ and $L_p = L_{p,0} + 1.2$ µm.

for devices with W ≥ 62.2 µm in experiments and W ≥ 45 µm in simulations. For devices with smaller width, a homogeneous current distribution was occurring through the device width while entering the NDR region. In this respect, I_{HOLD} in simulations was increasing with the device width for W < 45 µm since no current filaments were formed. For larger W, on the other hand, current filaments were forming and I_{HOLD} was becoming W-independent.

During simulations, since the natural mesh asymmetry created by the mesh generator was not always sufficient to induce a large enough inhomogeneity, which causes a filamentary state in a device with W ≥ 45 µm when entering the NDR region, a fine mesh region with width of 12.5 µm (wider than the filamentary wall thickness L_{CF}) was applied at one of the device edges and so an inhomogeneity in the current distribution along the device width was created. By doing like that it was ensured that a double hysteresis behaviour will always be obtained for all simulations with W ≥ 45 µm.

I_{HOLD} determined from 3D TCAD was almost layout independent. The value of I_{HOLD}

determined from 2D TCAD, on the other hand, was strongly depending on them and it was also typically several times higher. This has practical relevance for protection design because it told us to exclude 2D TCAD as a tool for latch-up safe ESD protection design of I_{HOLD}.

Chapter 4

Conclusion

In chapter 2.1, depending on the rise time (RT) of the pulse, the multi-finger devices exhibited different behaviors: simultaneous finger triggering for RT = 300 ps and sequential finger triggering (SFT) for RT = 10 ns. It was found that for RT = 300 ps, the fingers were triggering simultaneously due to the positive influence of a voltage overshoot related to delayed conductivity modulation in the p-sub. For RT = 10 ns, however, due to lateral carrier diffusion-limited processes and the coupling via substrate currents, fingers were triggering sequentially, which is accompanied by the voltage drops near the holding voltage. For RT = 10 ns, in addition, slow and fast triggering processes, with long (τ_{long} = 15-150 ns) and short (τ_{short} = 3-5 ns) trigger delay, respectively, have been found.

The triggering of each new finger pair was corresponding a drop in the voltage waveform. The more fingers were triggered, the longer τ_{long} was occurring due to lower one-dimensional current density, J, in the active fingers. TCAD simulations also confirmed that the average one-dimensional current density (J) is the main parameter controlling τ_{long}, where two slow diffusion-related processes limit subsequent trigger speed. Besides that, as soon as a minimum electron current density J, which is identical for all fingers, was established in the n-well of an individual finger, it was triggered. Analyses with different applied current, contact resistance, ambient temperature and active silicon layer thickness also showed that it was possible to influence trigger delay values in addition to RT. This study showed us that sequential finger triggering (SFT) is an important phenomenon because it helps SCR fingers to share the ESD current and so enhances the ESD robustness in case of pulses with long rise time.

In chapter 2.2, the multi-finger devices also exhibited SFT but with slightly different SFT mechanism. Although the position of the first triggered finger was changing from device to device, the finger triggering towards the left side was more preferable due to geometry of the device. Once a finger triggers, since the ground contact of the non-triggered neighbor finger on the left side is closer to the signal contact of the triggered finger, compared to that on the right side, it was taking less amount of time for holes from triggered finger to move and bias the non-triggered fingers on the left side. Thus, fingers were triggering towards the left side easier. In both triggering directions, the amount of current per triggered finger at the moment of the sequential triggering of the neighbor finger was decreasing with the increasing number of triggered fingers. This decrease, in addition, was showing a tendency to level off at high number of triggered fingers. The amount of required current for the triggering towards the right side; however, was still considerably higher than that for the triggering towards the left side.

Simulations with the structure without TT showed smaller current per triggered finger values compared to the devices which have TT at all fingers due to the attraction effect of TT on holes. Once we removed one of the fingers from the simulation structure to see the effect of a missing finger on the triggering behavior, on the other hand, the maximum device temperature reached to very high values due to self-heating effect, before the triggering of the finger which is next to the missing finger.

In chapter 3, the experiments with multi-finger SCRs showed us that the holding current, I_{HOLD}, is determined by the last active finger/segment, independent of the position of it. Therefore, by using DC and quasi-DC up and down current sweeps in EMMI and 3D TCAD, respectively, I_{HOLD} were investigated in single-finger ESD protection SCRs. During these investigation, it was found that the shape of the IV curve was related to spatial distribution of the current density in the width (W) direction. While in sufficiently long width devices (W is longer than five times the filamentary wall thickness (L_{CF})), a current filament (CF) was occurring and this was resulting in a double hysteresis IV behaviour, in devices with shorter widths, a homogeneous current distribution was happening and so a double hysteresis IV behaviour was not observed. For short width devices; thus, while I_{HOLD} was increasing with the device width, for longer W, I_{HOLD} was becoming W-independent. Besides that, the value of I_{HOLD} in width-extended devices was lower than that in the terminated devices. The simulation of width-extended devices; hence, was simplifying the 3D TCAD IV analysis and providing a safe margin for I_{HOLD} prediction.

The natural mesh asymmetry created by the mesh generator was not always sufficient to induce a large enough inhomogeneity in current distribution along the device width to cause a filamentary state in long width devices when entering the NDR region. Therefore, a fine mesh region (wider than L_{CF}) was introduced at one of the device edges and obtaining a double hysteresis IV behaviour in simulations of long width devices was ensured. The experiments also showed us that the way we measure had an influence on the IV curve. Parasitic elements in the measurement chain could result in serious oscillations. Importantly, while I_{HOLD} determined from 3D TCAD was typically independent of the layout parameters, the value of I_{HOLD} determined from 2D TCAD was strongly depending on them and also it was typically several times higher. 2D TCAD simulations were overestimating the I_{HOLD} values. This result; thus, showed us that 3D TCAD has to be used for the latch-up safe ESD protection design of I_{HOLD}.

References

[1] D Kahng and M. Atalla. "“Silicon-silicon dioxide field induced surface devices,” IRE-AIEEE Solid-State Device Research Conference, Carnegie Institute of Technology", (1960).

[2] G. E. Moore et al. *Cramming more components onto integrated circuits.* 1965.

[3] E. Amerasekera and F. N. Najm. *Failure mechanisms in semiconductor devices.* Wiley, 1997.

[4] J. Ebers. "Four-terminal pnpn transistors". *Proceedings of the IRE* **40** (1952) pp. 1361–1364.

[5] S. M. Sze. *Semiconductor devices: physics and technology.* John wiley & sons, 2008.

[6] G. Notermans, H.-M. Ritter, J. Utzig, S. Holland, Z. Pan, J. Schuett, J. Wynants, P. Huiskamp, W. Peters and B. Laue. "Design of an on-board ESD protection for USB3 applications". *IEEE Transactions on Device and Materials Reliability* **16** (2016) pp. 504–512.

[7] C. Fleury, G. Notermans, H.-M. Ritter and D. Pogany. "TIM, EMMI and 3D TCAD analysis of discrete-technology SCRs". *Microelectronics Reliability* **76** (2017) pp. 698–702.

[8] S. Holland, G. Notermans and H.-M. Ritter. "Modelling transient voltage overshoot of a forward biased pn-junction diode with intrinsic doped region". *2018 40th Electrical Overstress/Electrostatic Discharge Symposium (EOS/ESD).* IEEE. 2018 pp. 1–9.

[9] I. E. Commission et al. *IEC 61000-4-2, Electromagnetic compatibility (EMC)-Part 4-2: Testing and measurement techniques-Electrostatic discharge immunity test.* Tech. rep. IEC 61000-4-2, Dec, 2008.

[10] A. Level. "Electrostatic Discharge Sensitivity Testing– Human Metal Model (HMM)", (2009).

[11] J. Di Sarro, K. Chatty, R. Gauthier and E. Rosenbaum. "Study of design factors affecting turn-on time of silicon controlled rectifiers (SCRs) in 90 and 65nm bulk CMOS technologies". *2006 IEEE International Reliability Physics Symposium Proceedings.* IEEE. 2006 pp. 163–168.

[12] J Bourgeat, C. Entringer, P. Galy, M. Bafleur and D Marin-Cudraz. “Evaluation of the ESD performance of local protections based on SCR or bi-SCR with dynamic or static trigger circuit in 32 nm”. *Microelectronics Reliability* **50** (2010) pp. 1379–1382.

[13] G. Notermans, H.-M. Ritter, S. Holland and D. Pogany. “Modeling dynamic overshoot in ESD protections”. *2018 40th Electrical Overstress/Electrostatic Discharge Symposium (EOS/ESD)*. IEEE. 2018 pp. 1–9.

[14] H. Karaca, C. Fleury, S. Holland, H.-M. Ritter, G. Notermans and D. Pogany. “Mechanism of sequential finger triggering of multi-finger floating-base SCRs due to inherent substrate currents”. *2019 41st Annual EOS/ESD Symposium (EOS/ESD)*. IEEE. 2019 pp. 1–10.

[15] H. Karaca, C. Fleury, S. Holland, V. Kumar, H.-M. Ritter, G. Notermans and D. Pogany. “Simultaneous and sequential triggering in multi-finger floating-base SCRs depending on TLP pulse rise time”. *IEEE Transactions on Device and Materials Reliability*, (2020).

[16] W. Soldner, M. Streibl, U Hodel, M. Tiebout, H. Gossner, D. Schmitt-Landsiedel, J.-H. Chun, C. Ito and R. W. Dutton. “RF ESD protection strategies: Codesign vs. low-C protection”. *Microelectronics Reliability* **47** (2007) pp. 1008–1015.

[17] T Smedes and N Guitard. “Harmful voltage overshoots due to turn-on behaviour of ESD protections during fast transients”. *2007 29th Electrical Overstress/Electrostatic Discharge Symposium (EOS/ESD)*. IEEE. 2007 6A–4.

[18] K. Esmark, H. Gossner, S. Bychikhin, D. Pogany, C. Russ, G. Langguth and E. Gornik. “Transient behavior of SCRs during ESD pulses”. *2008 IEEE International Reliability Physics Symposium*. IEEE. 2008 pp. 247–253.

[19] C Musshoff, H Wolf, H Gieser, P Egger and X Guggenmos. “Risetime effects of HBM and square pulses on the failure thresholds of GGNMOS-transistors”. *Microelectronics Reliability* **36** (1996) pp. 1743–1746.

[20] K.-H. Oh, C. Duvvury, K. Banerjee and R. W. Dutton. “Analysis of nonuniform ESD current distribution in deep submicron NMOS transistors”. *IEEE Transactions on Electron Devices* **49** (2002) pp. 2171–2182.

[21] S Trinh, M Mergens, K Verhaege, C Russ, J. Armer, P. Jozwiak, B. Keppens, R. Mohn, G Taylor, F. De Ranter et al. “Multi-finger turn-on circuits and design techniques for enhanced ESD performance and width scaling”. *Microelectronics Reliability* **43** (2003) pp. 1537–1543.

[22] M.-D. Ker and J.-H. Chen. “Self-substrate-triggered technique to enhance turn-on uniformity of multi-finger ESD protection devices”. *IEEE journal of solid-state circuits* **41** (2006) pp. 2601–2609.

[23] C. Duvvury and C. Diaz. “Dynamic gate coupling of NMOS for efficient output ESD protection”. *Proc. IRPS.* Vol. 30. 1992 pp. 141–150.

[24] J. JEDEC. *ESDA Standard for Electrostatic Discharge Sensitivity Test Human Body Model (HBM) Component Level.* Tech. rep. ESDA ANSI/ESDA/JEDEC JS-001-2014, 2014.

[25] C. Fleury. “Behavior of silicon and gallium nitride devices under electrical overstress conditions”. PhD thesis. Wien, 2017.

[26] D Pogany, D Johnsson, S Bychikhin, K Esmark, P Rodin, M Stecher, E Gornik and H Gossner. “Measuring holding voltage related to homogeneous current flow in wide ESD protection structures using multilevel TLP”. *IEEE Transactions on Electron Devices* **58** (2010) pp. 411–418.

[27] E. A. Amerasekera and C. Duvvury. “ESD in silicon integrated circuits”, (2002).

[28] H. L. Grubin, V. V. Mitin, E. Schöll and M. P. Shaw. *The physics of instabilities in solid state electron devices.* Springer Science & Business Media, 2013.

[29] M Meixner, P Rodin, E Schöll and A Wacker. “Lateral current density fronts in globally coupled bistable semiconductors with S-or Z-shaped current voltage characteristics”. *The European Physical Journal B-Condensed Matter and Complex Systems* **13** (2000) pp. 157–168.

[30] E. Schöll and E. Scholl. *Nonlinear spatio-temporal dynamics and chaos in semiconductors.* 10. Cambridge University Press, 2001.

[31] A. Volkov and S. M. Kogan. “Physical phenomena in semiconductors with negative differential conductivity”. *Soviet Physics Uspekhi* **11** (1969) p. 881.

[32] V. L. Bonch-Bruevich, I. P. Zvyagin and A. G. Mironov. *Domain electrical instabilities in semiconductors.* Consultants Bureau, 1975.

[33] I. Varlamov, V. Osipov and E. Poltoratskii. “Current filamentation in a four-layer structure”. *Soviet Phys. Semiconductors* (1970) pp. 978–982.

[34] I. Varlamov and V. Osipov. “Current filamentation in pnpn-structures”. *Sov. Phys. Semicond.* **3** (1970) pp. 803–911.

[35] V. A. Vashchenko and V. F. Sinkevitch. *Physical limitations of semiconductor devices.* Springer, 2008.

[36] M. Dyakonov and M. Levinshtein. “Theory of propagation of the turned-on state in a thyristor”. *Sov Phys Semicond* **12** (1978) pp. 426–33.

[37] U. Glaser. “Complex ESD protection elements and issues in decananometre CMOS technologies”. PhD thesis. ETH Zurich, 2007.

[38] D Pogany, D Johnsson, S Bychikhin, K Esmark, P Rodin, E Gornik, M Stecher and H Gossner. “Nonlinear dynamics approach in modeling of the on-state-spreading-related voltage and current transients in 90nm CMOS silicon controlled rectifiers”. *2009 IEEE International Electron Devices Meeting (IEDM)*. IEEE. 2009 pp. 1–4.

[39] S. H. Voldman. *Latchup*. John Wiley & Sons, 2008.

[40] M.-D. Ker and S.-F. Hsu. *Transient-induced latchup in CMOS integrated circuits*. John Wiley & Sons, 2009.

[41] T Green and W. Denson. “A review of EOS/ESD field failures in military equipment”. *Proceedings of the 10th EOS/ESD Symposium*. Vol. 7. 1988.

[42] R. Merrill and E. Issaq. “ESD design methodology, 1993 EOS”. *Electrical Overstress/Electrostatic Discharge Symposium*. 1993 pp. 233–237.

[43] E. Association et al. *Standard for electrostatic discharge (esd) sensitivity testing: Human body model (hbm)-component level*. Tech. rep. Tech. Rep. ANSI/ESD STM5. 1, ESD Association, Rome, NY, USA, 2001.

[44] E. Discharge. *Sensitivity Testing: Human Body Model (HBM)—Component Level*. Tech. rep. document ANSI/ESDA/JEDEC JS-001-2017, 2017.

[45] E. Association et al. “ESD Association Standard Test Method for Electrostatic Discharge Sensitivity Testing: Charged Device Model-Component Level”. *ESD STM* **5**, 1 (1999).

[46] E. Association et al. “ESD STM5. 2-1999: Standard test method for electrostatic discharge sensitivity testing: machine model (MM)–Component level”. *ESD Association*, (1999).

[47] I. S.-I.-I. E. Commission et al. *Section of IEC 61000–4–5*. 2005.

[48] H. Michael. “Holographic Interferometric Investigation of Power Devices under ESD Stress”, (2005).

[49] M. Heer. “Semiconductor devices and integrated circuits under short electrical stress”. PhD thesis. 2012.

[50] M Scholz. “Closing the design gap between system-level and component-level electro static discharge (esd)”. *Ph. D. dissertation*, (2013).

[51] Y. Zhou, J.-J. Hajjar, A. W. Righter and K. P. Lisiak. “Modeling snapback of LVTSCR devices for ESD circuit simulation using advanced BJT and MOS models”. *2007 29th Electrical Overstress/Electrostatic Discharge Symposium (EOS/ESD)*. IEEE. 2007 3A–3.

[52] L. Buccolini and A. delle Marche. *Simple SPICE ESD Generator Circuit Based on IEC61000-4-2 Standard*. 2018.

[53] J. E. Barth, K. Verhaege, L. G. Henry and J. Richner. “TLP calibration, correlation, standards, and new techniques”. *IEEE Transactions on Electronics Packaging Manufacturing* **24** (2001) pp. 99–108.

[54] G. Notermans, S. Bychikhin, D. Pogany, D. Johnsson and D. Maksimovic. “HMM–TLP correlation for system-efficient ESD design”. *Microelectronics Reliability* **52** (2012) pp. 1012–1019.

[55] S. Agarwal. “What’s The Difference Between HBM, CDM, And MM Test”. *Electronic Design, March*, (2014).

[56] W. Mamanee. “Investigation of current filament behavior in smart power technology ESD protection devices subjected to long ESD-like pulses”. PhD thesis. 2012.

[57] C. Duvvury, R. Ashton, O. Semiconductor, A. Righter and A. Devices. “Discontinuing use of the machine model for device ESD qualification”. *Compliance Magazine* (2012) pp. 56–63.

[58] P. L. F. Penalver and E. da Silva Braga. “Simulation of Surge Protection for a Direct Current Circuit”. *International Journal of Electrical and Computer Engineering* **11** (2016) pp. 1–5.

[59] T. Maloney and N. Khurana. “Transmission line pulsing techniques for circuit modeling of ESD phenomena”. *Proc. EOS/ESD Symp., 1985*. 1985 pp. 49–54.

[60] W. Simbürger, D. Johnsson and M. Stecher. “High current TLP characterisation: An effective tool for the development of semiconductor devices and ESD protection solutions”. *ARMMS RF & microwave society* (2012) pp. 1–4.

[61] R. Soref and B. Bennett. “Electrooptical effects in silicon”. *IEEE journal of quantum electronics* **23** (1987) pp. 123–129.

[62] J. McCaulley, V. Donnelly, M Vernon and I Taha. “Temperature dependence of the near-infrared refractive index of silicon, gallium arsenide, and indium phosphide”. *Physical Review B* **49** (1994) p. 7408.

[63] D. Pogany, S. Bychikhin, M. Heer, W Mamanee and E. Gornik. “Application of transient interferometric mapping method for ESD and latch-up analysis”. *Microelectronics Reliability* **51** (2011) pp. 1592–1596.

[64] C. Fürböck, K Esmark, M. Litzenberger, D. Pogány, G Groos, R Zelsacher, M Stecher and E. Gornik. “Thermal and free carrier concentration mapping during ESD event in smart power ESD protection devices using an improved laser interferometric technique”. *Microelectronics Reliability* **40** (2000) pp. 1365–1370.

[65] D. Pogany, S. Bychikhin, C Furbock, M. Litzenberger, E. Gornik, G. Groos, K. Esmark and M. Stecher. “Quantitative internal thermal energy mapping of semiconductor devices under short current stress using backside laser interferometry”. *IEEE Transactions on Electron Devices* **49** (2002) pp. 2070–2079.

[66] D. Pogány, S. Bychikhin, M. Litzenberger, E. Gornik, G Groos and M Stecher. “Extraction of spatio-temporal distribution of power dissipation in semiconductor devices using nanosecond interferometric mapping technique”. *Applied physics letters* **81** (2002) pp. 2881–2883.

[67] D. Pogány, V. Dubec, S. Bychikhin, C Furbock, A Litzenberger, G Groos, M Stecher and E Gornik. “Single-shot thermal energy mapping of semiconductor devices with the nanosecond resolution using holographic interferometry”. *IEEE Electron device letters* **23** (2002) pp. 606–608.

[68] M. Litzenberger, C Furbock, S. Bychikhin, D. Pogany and E. Gornik. “Scanning heterodyne interferometer setup for the time-resolved thermal and free-carrier mapping in semiconductor devices”. *IEEE transactions on instrumentation and measurement* **54** (2005) pp. 2438–2445.

[69] J van Zwol, W Kemper and P Bruin. “Transmission line pulsed photo emission microscopy as an ESD troubleshooting method”. *2003 Electrical Overstress/Electrostatic Discharge Symposium*. IEEE. 2003 pp. 1–8.

[70] C. Russ, K. Bock, M. Rasras, I. De Wolf, G. Groeseneken and H. E. Maes. “Non-uniform triggering of gg-nMOSt investigated by combined emission microscopy and transmission line pulsing”. *Electrical Overstress/Electrostatic Discharge Symposium Proceedings. 1998 (Cat. No. 98TH8347)*. IEEE. 1998 pp. 177–186.

[71] F. E. Gentry. *Semiconductor controlled rectifiers: principles and applications of pnpn devices*. Prentice-Hall, 1964.

[72] Z. Qi, M. Qiao, Y. He and B. Zhang. “High holding voltage SCR for robust electrostatic discharge protection”. *Chinese Physics B* **26** (2017) p. 077304.

[73] P. Hongwei, L. Siyang and S. Weifeng. “A novel latch-up free SCR-LDMOS with high holding voltage for a power-rail ESD clamp”. *Journal of Semiconductors* **34** (2013) p. 014007.

[74] Y.-C. Huang and M.-D. Ker. “A latchup-immune and robust SCR device for ESD protection in 0.25-μm 5-V CMOS process”. *IEEE Electron Device Letters* **34** (2013) pp. 674–676.

[75] Z. Liu, J. He, J. J. Liou, J. Liu, M. Miao and S. Dong. “Segmented SCR for high voltage ESD protection”. *2012 IEEE 11th International Conference on Solid-State and Integrated Circuit Technology*. IEEE. 2012 pp. 1–4.

[76] C.-T. Dai and M.-D. Ker. “Comparison between high-holding-voltage SCR and stacked low-voltage devices for ESD protection in high-voltage applications”. *IEEE Transactions on Electron Devices* **65** (2018) pp. 798–802.

[77] B.-B. Song, K.-I. Do and Y.-S. Koo. “SCR-based ESD protection using a penta-well for 5 V applications”. *IEEE Journal of the Electron Devices Society* **6** (2018) pp. 691–695.

[78] M. P. Mergens, C. C. Russ, K. G. Verhaege, J. Armer, P. C. Jozwiak, R. P. Mohn, B. Keppens and C. S. Trinh. “Speed optimized diode-triggered SCR (DTSCR) for RF ESD protection of ultra-sensitive IC nodes in advanced technologies”. *IEEE Transactions on Device and Materials Reliability* **5** (2005) pp. 532–542.

[79] M. P. Mergens, C. C. Russ, K. G. Verhaege, J. Armer, P. C. Jozwiak and R. Mohn. “High holding current SCRs (HHI-SCR) for ESD protection and latch-up immune IC operation”. *Microelectronics Reliability* **43** (2003) pp. 993–1000.

[80] M. P. Mergens, O. Marichal, S. Thijs, B. Van Camp and C. C. Russ. “Advanced SCR ESD protection circuits for CMOS/SOI nanotechnologies”. *Proceedings of the IEEE 2005 Custom Integrated Circuits Conference, 2005.* IEEE. 2005 pp. 481–488.

[81] J. Li, J. Di Sarro and R. Gauthier. “Design and optimization of SCR devices for on-chip ESD protection in advanced SOI CMOS technologies”. *Electrical Overstress/Electrostatic Discharge Symposium Proceedings 2012.* IEEE. 2012 pp. 1–7.

[82] J. Li, S. Mitra, H. Li, M. J. Abou-Khalil, K. Chatty and R. Gauthier. “Capacitance investigation of diode and GGNMOS for ESD protection of high frequency circuits in 45nm SOI CMOS technologies”. *EOS/ESD 2008-2008 30th Electrical Overstress/Electrostatic Discharge Symposium.* IEEE. 2008 pp. 228–234.

[83] I Jyothi, V Janardhanam, H. Hong and C.-J. Choi. “Current–voltage and capacitance–voltage characteristics of Al Schottky contacts to strained Si-on-insulator in the wide temperature range”. *Materials Science in Semiconductor Processing* **39** (2015) pp. 390–399.

[84] B Afzal, A Zahabi, A Amirabadi, Y Koolivand, A Afzali-Kusha and M El Nokali. “Analytical model for C–V characteristic of fully depleted SOI–MOS capacitors”. *Solid-state electronics* **49** (2005) pp. 1262–1273.

[85] G. Krieger. “Thermal response of integrated circuit input devices to an electrostatic energy pulse”. *IEEE transactions on electron devices* **34** (1987) pp. 877–882.

[86] B. El-Kareh and R. J. Bombard. *Introduction to VLSI silicon devices: physics, technology and characterization.* Vol. 10. Springer Science & Business Media, 2012.

[87] N. Jensen, G. Groos, M. Denison, J. Kuzmik, D. Pogany, E. Gornik and M. Stecher. “Coupled bipolar transistors as very robust ESD protection devices for automotive applications”. *2003 Electrical Overstress/Electrostatic Discharge Symposium*. IEEE. 2003 pp. 1–6.

[88] J.-R. Manouvrier, P. Fonteneau, C.-A. Legrand, H. Beckrich-Ros, C. Richier, P. Nouet and F. Azais. “A physics-based compact model for ESD protection diodes under very fast transients”. *EOS/ESD 2008-2008 30th Electrical Overstress/Electrostatic Discharge Symposium*. IEEE. 2008 pp. 67–75.

[89] Z. Pan, D. Schroeder, S. Holland and W. H. Krautschneider. “Understanding and modeling of diode voltage overshoots during fast transient ESD events”. *IEEE transactions on Electron Devices* **61** (2014) pp. 2682–2689.

[90] R. L. Davies and J. Petruzella. “Pnpn charge dynamics”. *Proceedings of the IEEE* **55** (1967) pp. 1318–1330.

[91] J. Moll, M Tanenbaum, J. Goldey and N Holonyak. “PNPN transistor switches”. *Proceedings of the IRE* **44** (1956) pp. 1174–1182.

[92] H. Liang, X. Bi, X. Gu, H. Cao and Y. Zhang. “Investigation on LDMOS-SCR with high holding current for high voltage ESD protection”. *Microelectronics Reliability* **61** (2016) pp. 120–124.

[93] S. Bart, B. Ilse, M. Olivier and K. Bart. “On-chip ESD protection with improved high holding current SCR (HHISCR) achieving IEC 8kV contact system level”. *Electrical Overstress/Electrostatic Discharge Symposium Proceedings 2010*. IEEE. 2010 pp. 1–10.

[94] M Litzenberger, C Furbock, D. Pogany, E. Gornik, K Esmark and H Gossner. “Investigation of 3D phenomena in the triggering of gg-nMOS electrostatic discharge protection devices”. *30th European Solid-State Device Research Conference*. IEEE. 2000 pp. 520–523.

[95] H. Gossner, K. Esmark and W. Stadler. *Simulation methods for ESD protection development*. Elsevier, 2003.

[96] B. Ridley. “Specific Negative Resistance in Solids”. *Proceedings of the Physical Society* **82** (1963) pp. 954–966.

[97] A. Blicher. *Thyristor physics*. Vol. 12. Springer Science & Business Media, 2013.

[98] A. Stricker, D. Gloor and W. Fichtner. “Layout optimization of an ESD-protection n-MOSFET by simulation and measurement”. *Electrical Overstress/Electrostatic Discharge Symposium Proceedings*. IEEE. 1995 pp. 205–211.

[99] M. Heer, S. Bychikhin, W. Mamanee, D. Pogany, A Heid, P Grombach, M Klaussner, W. Soppa and B Ramler. “Experimental and numerical analysis of current flow homogeneity in low voltage SOI multi-finger gg-NMOS and NPN ESD protection devices”. *Microelectronics Reliability* **47** (2007) pp. 1450–1455.

[100] M. Heer, S. Bychikhin, V. Dubec, D. Pogány, E. Gornik, M Dissegna, L Cerati, L Zullino, A Andreini, A Tazzoli et al. “Analysis of the triggering behavior of low voltage BCD single and multi-finger gc-NMOS ESD protection devices”. *2006 Electrical Overstress/Electrostatic Discharge Symposium.* IEEE. 2006 pp. 275–284.

[101] N. Seliger, P. Habaš and E. Gornik. “A study of backside laser-probe signals in MOSFETs”. *Microelectronic engineering* **31** (1996) pp. 87–94.

[102] S. Kasapi, C.-C. Tsao, K. Wilsher, W. Lo and S. Somani. “Laser beam backside probing of CMOS integrated circuits”. *Microelectronics Reliability* **39** (1999) pp. 957–961.

[103] K. Esmark. “Device simulation of ESD protection elements”. PhD thesis. ETH Zurich, 2001.

[104] M Denison, M Blaho, P Rodin, V Dubec, D Pogany, D Silber, E Gornik and M Stecher. “Moving current filaments in integrated DMOS transistors under short-duration current stress”. *IEEE Transactions on Electron Devices* **51** (2004) pp. 1695–1703.

[105] T. Sentaurus. “Industry-Standard Process and Device Simulators, Synopsys”. *Inc., May*, (2012).

[106] P. Salome, C Leroux, J. Chante, P Crevel and G Reimbold. “Study of a 3D phenomenon during ESD stresses in deep submicron CMOS technologies using photon emission tool”. *1997 IEEE International Reliability Physics Symposium Proceedings. 35th Annual.* IEEE. 1997 pp. 325–332.

[107] M Gartner, D Vietzke, D Reznik, M Stoisiek, K.-G. Oppermann and W Gerlach. “Bistability and hysteresis in the characteristics of segmented-anode lateral IGBTs”. *IEEE Transactions on Electron Devices* **45** (1998) pp. 1575–1579.

[108] H. Karaca, C. Fleury, S. Holland, H.-M. Ritter, R. Krainer, V. Kumar, G. Notermans and D. Pogany. “Triggering of multi-finger and multi-segment SCRs near the holding voltage studied by emission microscopy under DC conditions”. *ESDA/IEW.* IEEE. 2021 to be published.

[109] A Alekseev, S Bose, P Rodin and E Schöll. “Stability of current filaments in a bistable semiconductor system with global coupling”. *Physical Review E* **57** (1998) p. 2640.

Curriculum Vitae

Personal information

E-mail hasan.karaca@tuwien.ac.at
Nationality Turkey
Birth 16.04.1991 in Silifke, Mersin, Turkey

Professional experience

11.2017–07.2021 **Project assistant**, *TU Wien*, Vienna, Austria.
Institute of Solid State Electronics, Vienna, Austria

Electro-optical characterization and TCAD simulations of Silicon Controlled Rectifiers as external ESD protection under EOS/ESD events.

Partners Nexperia Hamburg

09.2015–02.2016 **R&D Engineer**, *Bilkent University Nanotechnology Research Center (NANOTAM)*, Ankara, Turkey.

Modeling and simulation of GaN HEMT transistor by using IC-CAP to be used in ADS. Modeling and simulation of GaN HEMT transistor by using Synopsys Sentaurus TCAD

02.2014–05.2014 **Part-Time Engineer**, *ASELSAN INC.*, Ankara, Turkey.

Vhdl coding with Xilinx Zinq

07.2013–08.2013 **Internship**, *ASELSAN INC.*, Ankara, Turkey.

Estimating the thickness of the ionosphere by using Matlab codes. It was necessary to find the place of a target by using radio frequencies reflecting from ionosphere

06.2012–07.2012 **Internship**, *Basari Technology*, Ankara, Turkey.

Design and production of a switch mode power supply (smps) used in electric meters

Education

2018–Present	**Ph.D. in Electrical Engineering**, *TU Wien*, Vienna, Austria. Institute of Solid State Electronics, Vienna, Austria
thesis	Experimental and TCAD Analysis of Behaviour of Multifinger Devices with Substrate Coupling and of Filamentary States in SCRs for ESD Protection
supervisor	Ao.Univ.Prof. Dipl.-Ing. Dr. Dionyz Pogany
GPA	3.46/4
2014–2017	**M.Sc. in Electrical and Electronics Engineering**, *Bilkent University*, Ankara, Turkey. Department of Electrical and Electronics Engineering, Bilkent University, Ankara, Turkey
thesis	A micromachined pressure sensor
supervisor	Prof. Abdullah Atalar
GPA	3.73/4
2014–2017	**B.Sc. in Electrical and Electronics Engineering**, *Bilkent University*, Ankara, Turkey. Department of Electrical and Electronics Engineering, Bilkent University, Ankara, Turkey
GPA	3.72/4

Awards

2020	Best Student Paper Award, 41st Annual EOS/ESD Symposium (Riverside, CA, USA)
2014	Bilkent University Graduate Scholarship
2009	Bilkent University Merit Scholarship

Projects

- Development and investigation of sequential finger triggering and filamentary states in Silicon Controlled Rectifiers (SCRs)
- CMUT (Capacitive Micromachined Ultrasonic Transducer) and Oscillator based Pressure Sensor Design with Cadence
- Modeling and simulation of GaN HEMT transistor by using IC-CAP to be used in ADS
- Modeling and simulation of GaN HEMT transistor by using Synopsys Sentaurus TCAD

- Developing Ge and ZnS based CO/CO2 sensor by using Lumerical FDTD.
- Developing thin film transistor by using COMSOL.
- Voice over Laser Transmission System which transmits the speech by using laser light and PLL.
- Developing Speech Recognition System with two people by using MATLAB and FPGA. It can recognize the numbers from zero to nine and show it on the seven segment display.
- Measuring the temperature by using LM335 temperature sensor and 8051 microprocessor. Also showing the temperature on an LCD screen.
- Measuring the temperature by using LM335 temperature sensor and Basys 2 FPGA Board. Also by using VHDL codes, showing the temperature on the computer screen.
- Developing software called "Math Tool" with three people by using Java. It can make scientific calculations, plot graphs, convert units to each other and calculate interest.

Technical skills and competences

Programming Languages	Java, VHDL, Intel 8051 Assembly Language
Packaged Software	Synopsys Sentaurus TCAD, MATLAB, COMSOL, Lumerical, 5Spice and LTSpice Analysis, OrCAD, Proteus, IC-CAP, Cadence, Tanner L-Edit, and Office programs
Characterization	Transmission Line Pulser, Transient Interferometric Mapping, Emission Microscopy

Certificates and Documents

2015	Synopsys Sentaurus TCAD course certificate by Microelectronics Support Centre, Oxford, UK
2011-2014	Bilkent University High Honor Student, Turkey
2008	OYAK National Math Olympics, first place as a team, Bolu, Turkey
2008	OYAK National Math Olympics, attending Turkey Championship, Istanbul, Turkey

List of publications

Journal papers

H. Karaca, C. Fleury, S. Holland, V. Kumar, H.-M. Ritter, G. Notermans and D. Pogany. "Simultaneous and sequential triggering in multi-finger floating-base SCRs depending on TLP pulse rise time". *IEEE Transactions on Device and Materials Reliability*, (2020)

N Lambert, A Taylor, P Hubík, J Bulíř, J More-Chevalier, H Karaca, C Fleury, J Voves, Z Šobáň, D Pogany et al. "Modeling current transport in boron-doped diamond at high electric fields including self-heating effect". *Diamond and Related Materials* **109** (2020) p. 108003

H. Karaca, S. Holland, H.-M. Ritter, V. Kumar, G. Notermans and D. Pogany. "3D TCAD Methodology for Simulating Double-hysteresis filamentary IV Behavior and Holding Current in ESD Protection SCRs". *IEEE Transactions on Electron Devices* (2021) in reviewing process, submitted revised version

Conference presentations

H. Karaca, C. Fleury, S. Holland, H.-M. Ritter, G. Notermans and D. Pogany. "Mechanism of sequential finger triggering of multi-finger floating-base SCRs due to inherent substrate currents". *2019 41st Annual EOS/ESD Symposium (EOS/ESD)*. IEEE. 2019 pp. 1–10

H. Karaca, C. Fleury, S. Holland, H.-M. Ritter, R. Krainer, V. Kumar, G. Notermans and D. Pogany. "Triggering of multi-finger and multi-segment SCRs near the holding voltage studied by emission microscopy under DC conditions". *International ESD Workshop (ESDA/IEW)*. IEEE. 2021, to be published.

V. Kumar, H. Karaca, S. Holland, H.-M. Ritter and D. Pogany. "Influencing SCR Holding Current by Segmentation Topology". *International ESD Workshop (ESDA/IEW)*.

IEEE. 2021, to be published.